國 立 交 通 大 學

土 木 工 程 學 系
博 士 論 文

利用多衛星測高資料改善全球重力異常模型以及淺海區重力異常

Improved Determinations of Global Gravity Anomaly Model and Shallow-Water Gravity Anomalies from Multi-Satellite Altimetry

研究生：徐欣瑩

指導教授：黃金維

中華民國九十六年六月

利用多衛星測高資料改善全球海洋重力異常模型以及淺海區重力異常

研究生：徐欣瑩　　　　　　　　　　　　指導教授：黃金維

國立交通大學土木工程研究所

摘要

　　本論文的內容主要是致力於改善全球海洋重力異常模型以及淺海區重力異常。本研究結合 Seasat, Geosat/GM, Geosat/ERM, ERS-1/35day, ERS-1/GM, ERS-2, 以及 T/P 等七種衛星測高任務資料來推求全球海洋重力異常模型以及全球平均海水面模型，以 2' X 2' 的解析度涵蓋全球南緯 80 度到北緯 80 度的區域範圍。全球平均海水面模型透過與 T/P 以及 ERS-1 的平均海水面模型進行比較，可分別得出 5.0 公分以及 3.1 公分的均方根值。在全球選擇出十二個區域，進行船測重力異常與全球重力異常模型之比較，得出其差值之均方根值最大為 13.4mgals，最小為 3.0mgals。

　　為改善衛星測高的資料品質，本研究從資料偵錯以及資料型態兩方面著手，採用一種非線性的濾波函數對沿軌跡的測高資料進行粗差偵測，以及採用海水面高度值一次差作為資料型態，研究成果顯示可以得出較佳的重力異常。本研究選擇東海海域以及台灣海峽作為改善淺海區重力異常的研究區域，在此兩區域比較兩個不同的全球海洋測高重力異常模型，將兩模型的差異值進行分析討論，可以得出重力異常的差異與海潮模式的選擇、海水面高度值的中誤差以及海深有其相關性。

　　為改善淺海區重力異常，本研究採用不同的資料型態搭配計算方法產生三種推求重力異常的方法進行測試：第一種方法是採用最小二乘預估法，資料型態採用海水面高度值一次差以及海水面高度值的梯度值；第二種方法是採用沿軌跡的垂線偏差值作為資料型態以最小二乘預估進行計算重力異常；第三種方法是採用

最小二乘預估將沿軌跡垂線偏差組成網格，再以 inverse Vening Meinesz 公式進行計算。以上三種方法在台灣海峽進行淺海區重力異常計算，並與船測重力進行比較，分別得出其差值的均方根為 9.06,10.26,10.44 以及 10.73 mgals;在東海區域分別得到的結果是 9.59,9.77,13.10,11.86 mgals。由此可知採用海水面高度值一次差以及海水面高梯度值作為測高資料型態可以得出較佳的重力異常成果。對於陸地沿岸的淺海區重力異常推求，若加入沿岸陸地重力資料，可以明顯改善淺海區的重力異常，本研究在台灣海峽沿岸進行測試，得出差值的均方根為 8.22mgals。

Improved Determinations of Global Gravity Anomaly Model and Shallow-Water Gravity Anomalies from Multi-Satellite Altimetry

Phd Student: Hsin-Ying Hsu　　　　　**Advisor: Cheinway Hwang**

Department of Civil Engineering

National Chiao Tung University

ABSTRACT

This dissertation is aimed at improved determination of global and shallow water gravity anomalies. Global mean sea surface heights (SSHs) and gravity anomalies on a 2´×2´ grid were determined from Seasat, Geosat (ERM and GM), ERS-1 (1.5-year mean of 35-day, and GM), TOPEX/POSEIDON (T/P) (5.6-year mean) and ERS-2 (2-year mean) altimeter data over the region 0°-360° longitude and –80°-80° latitude. The comparison of the global mean sea surface height (MSSH) with the T/P and the ERS-1 MSSH result in overall RMS differences of 5.0 and 3.1 cm in SSH, respectively, and 7.1 and 3.2 µrad in SSH gradient, respectively. The RMS differences between the predicted and shipborne gravity anomalies range from 3.0 to 13.4 mgals in 12 areas of the world oceans.

To improve the altimeter data quality, a nonlinear filter with outlier rejection is applied to along-track data, and differenced height is found to be most sensitive to this method. The differences of two global satellite altimeter-derived gravity anomaly grids over the East China Sea (ECS) and the Taiwan Strait (TS) are investigated and

the causes of the differences are discussed. Difference of gravity anomaly is correlated with tide model error, standard deviation of sea surface heights (SSHs) and ocean depth.

To improve the shallow water gravity anomalies, three methods of gravity anomaly derivation from altimetry were compared near Taiwan and East China Sea: (1) compute gravity anomalies by LSC using along-track, differenced geoidal heights and height slopes, (2) compute gravity anomalies by least-squares collocation (LSC) using altimeter-derived along-track deflections of vertical (DOV), and (3) grid along-track deflections of vertical by LSC and then compute gravity anomalies by the inverse Vening Meinesz formula. For the three methods, the RMS differences between altimetry-derived gravity anomalies and shipborne gravity anomalies are 9.06 (differenced height) and 9.59, 10.26 (height slope) and 9.77, 10.44 and 13.10, 10.73 and 11.86 mgals, in Taiwan Strait and East China Sea respectively. Two new SSH-derived observations of altimetry (differenced height and height slope) were presented for gravity derivation and use of differenced heights in LSC produces the best result. Use of land gravity data in the vicinity of coasts was implemented near Taiwan and this enhances the accuracy of altimeter-derived gravity anomalies at a RMS difference of 8.22 mgals.

CONTENTS

CHAPTER 3 GLOBAL MODELS OF MEAN SEA SURFACE AND GRAVITY ANOMALY 41

CHAPTER 4 DATA PROCESSING AND METHODS OF GRAVITY DERIVATION OVER SHALLOW-WATERS 58

CHAPTER 5 GRAVITY ANOMALY OVER EAST CHINA SEA AND TAIWAN STRAIT: CASE STUDY AND ANALYSIS 74

LIST OF FIGURES

LIST OF TABLES

CHAPTER 1

INTRODUCTION

1.1 Development of Satellite Altimetry

1.1.1 Past Satellite Altimetry Missions

From 1980s, with the advanced development of computer science and space technology, the study of the earth science itself has changed as we better understand everything from the macroscopic aspect to microcosmic dimension. Over the past few decades satellite altimetry has developed into a new way to study the earth. The basic concept is very simple. The satellite is used as a moving platform, with a sensor to receive the return signals after reflection at the earth's surface. Through data processing and analysis, we can study the problems of geodesy, geophysics and oceanography.

Satellite altimetry has only been around for 30 years, but even though it is still a very young science, the results of its research explain geoid and gravity anomaly better than ever before. Its history demonstrates huge potential in improving the study of the global gravity field, and studying the oceans currents and surface. Satellite altimetry shows the structure of the bottom of the ocean from a viewpoint that has never before been possible. Because of its characteristics: worldwide range, high accuracy, rapid and periodic, satellite altimetry can help us explore all kinds of phenomena in earth sciences. Therefore we can take the study of the earth to another level providing extensive information about the earth.

The first satellite launched exclusively for altimeter research was called Skylab (Seeber, 1993). Skylab was launched on 9, April 1975, and was the first satellite of its kind specifically designed to research the physical attributes of the ocean by satellite. The experiment didn't yield many results but was a good foundation for future missions such as Geos-3 through the National Aeronautics Space Administration (NASA).

Skylab weighed 345.9kg, orbit altitude is 840km, with an incline angle is 115°. Its lifespan was 3.5 years, repeating its orbital cycle every 23 days with an altimeter accuracy of about 25~50cm. The satellite was designed to provide useful parameters of oceanography and geodynamics for over 3 years enhancing our capability to earth gravity field, the shape and the size of geoid, deep ocean tide, ocean current structure, the crust structure and rigid geodynamics etc. Geos-3 was successfully launched into regular orbit, which is a model mission for future satellites to be launched.

On June28, 1978, Seasat (Sea Satellite) altimeter was launched with a new remote sensing technique. This new method of researching ocean science began a new era of ocean exploration. The satellite has an altitude of 800km, at an incline angle of 108°. This satellite is expected to function for 106 days, the first repeat cycle is 3 days, and the post repeat cycle is 17 days, with an accuracy of about 20~30cm. Seasat was launched to provide a remote sensing technique that could measure the whole earth very precisely while measuring the temperature, current and tides of the ocean simultaneously. In spite of the fact that Seasat worked perfectly in orbit for almost 3 months, the electronics of altimeter malfunctioned and it stopped working, but it still provided a lot of statistics about the ocean even after it malfunction. Through satellite altimetry we have advanced so much in our knowledge of ocean geoid, sea surface terrain, marine gravity, the seafloor, geodynamics and oceanography that there is no way to overlook its value.

In order to efficiently develop accurate measurements, correctly measure earths gravity field, understand the shape of the geoid, and make up for the weakness of Seasat for its short life span that limits the amount of time to collect information, the American Navy launched the Geosat (Geodetic Satellite) satellite altimeter on March 12, 1985. Its primary mission was to precisely measure all gravity fields throughout the entire world. Geosat's average orbit altitude is 800km, with an inclination angle of 108 degrees. Geosat will repeat its cycle every 17 days throughout its functional lifespan of more than 4 years. Geosat is accurate within about 10~ 20cm. It took 18 months from its launch date in March 1985, through 30 Sept 1896 for the Geosat satellite to complete its mission of tracking the entire earth in 4km intervals. The tracks that were flown while measuring the worlds great oceans combined would measure 200 million km, and the project collected 270 million measurements.

Geosat orbit repeats every 17 days in precisely the frozen orbit, this is called an Exact Repeat Mission (ERM). Statistics from the Geosat, satellite altimeter data are used to gather information about earth gravity field, sea mountain, oceanic trench, ocean floor over a very wide area. This project was a huge accomplishment and the first of its kind. The information gathered in satellite altimetry has been tested and has proved to be very accurate in measuring the global geoid, gravity anomaly, gravity disturbance, establish a higher degree gravity model, seafloor, geological structure, solid geophysics, oceanography, ocean tide, and ocean current. There are many possibilities for the uses of satellite altimetry in the future.

The European Space Agency (ESA) after ten years of preparation launched the first European Remote-Sensing Satellite (ERS-1) on July 17, 1991, ERS-1's average altitude is 785km, the incline angle is 98.5°, and orbits the earth every 100 minutes throughout its 3 year life. Its main mission is to study the Earth's atmosphere and its

ocean. During its first 3 months in orbit ERS-1 will cover the whole earth every three days. ERS-1 has the ability to adjust its orbital altitude and cycle. After the first three months the satellite switched to normal orbital cycles every 35 days. At the end of its mission the satellite repeated every 168 days.

ERS-1 measures ocean waves, wind field and its change, ocean circulations, global sea level change, and provides satellite images of both land and ocean, sea surface topography, sea surface temperature, and sea surface vapor and may other things. ERS-2, the follow-on of ERS-1, was used together with it from April 1995 to June 1996, their identical orbits (35 days) have a one-day shift.

In order to be more accurate in measuring the surface of the ocean, and in researching ocean circulation and ocean tide, NASA and CNES jointly launch Topex/Poseidon (T/P) on Aug 10, 1992, a satellite mission with the objective of "observing and understanding the ocean circulation". Its altitude in orbit is about 1336 km, with an inclination angle of 66°. Topex/Poseidon is capable of covering 90% of both the earth and ocean, it has a repeat cycle of 10 days and collects statistics on the whole earth 35 times each year.

The main purpose of the Topex/Poseidon mission is monitoring global sea surface height, determining the ocean currents and measuring the effect of these currents on the surrounding areas. This information provide statistics about the parameter of the ocean for the whole world. So far T/P has the best performance on the accuracy of precision orbit determination in all altimetry mission.

Because of the significant meaning of altimeter data in geodesy, oceanography and geophysics, the ERS-1-follow-on, ERS-2 were launched in April 1994. Geosat came before GEOSAT Follow-On (GFO) which was launched Feb 1998. T/P came

before Jason-1, which was launched on December 7, 1992. Lots of advancement have been made in altimeter technology that have advanced all areas of researching the ocean. The satellites have collected enormous amounts of data that still need to be researched.

1.1.2   Current and Future Satellite Altimetry Missions

(1) GEOSAT Follow-On 1 (GFO-1)

The GEOSAT Follow-On 1 (GFO-1) program is the U.S. Navy's plan to develop an workable series of radar altimeter satellites to continuously monitor the ocean observations from the GEOSAT Exact Repeat Mission (ERM) orbit (800 km altitude, 108° inclination, 0.001 eccentricity, and, 100 min period). GFO-1 is the follow-on to the highly successful GEOSAT and was launched in February 1998. On 29 November 2000, the U.S. Navy declared the satellite as operational.

The first 17-day Cycle after the U.S. Navy began using it is numbered 000 and is used as a reference for the succeeding cycles.   After the reference cycle, the first 17-day cycle which started on December 16, 2000 (Julian day 352) is the beginning of the first evaluation cycle, Cycle 001, which ended on 2 January 2001 (Julian day 2001 002).   Each following 17 day cycle is consecutively numbered. This 17-day Exact Repeat Orbit (ERO) retraces the same ERM ground track to +/-1 km. As with the original GEOSAT ERM, the data will be available for ocean science through NOAA/NOS and NOAA/NESDIS.

The 5-year GEOSAT mission with its extensive data validation program confirmed the ability of the radar altimeter to measure the dynamic topography of the western boundary currents such as the Gulf Stream, as well as their associated rings

and eddies, to provide sea surface height data for assimilation into numerical models, and to map the progression of El Nino in the equatorial Pacific. Figure 1.1 is the ground tracks of Geosat/ERM (the same as GFO-1) around Taiwan.
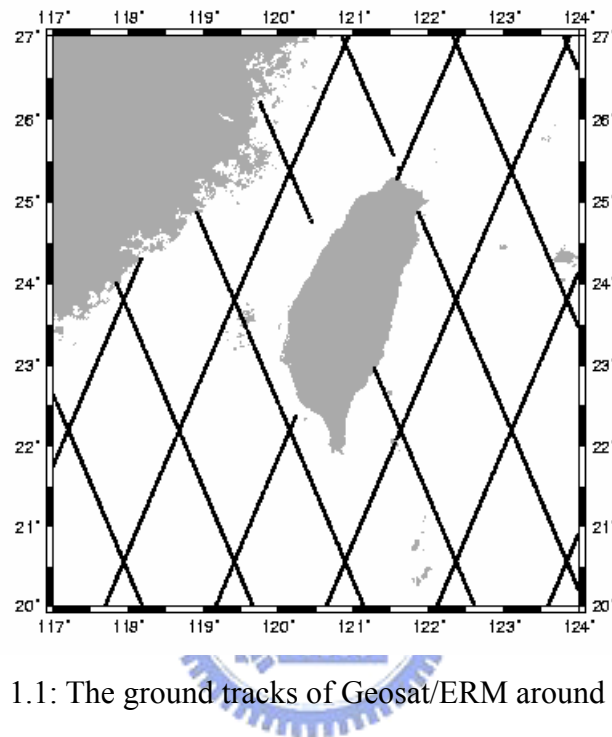
Figure 1.1: The ground tracks of Geosat/ERM around Taiwan.

(2) Environmental Satellite (EnviSat)

The main objective of the Envisat program is to provide Europe with an improved capability for the remote sensing observation of Earth from space. The goal is to increase the capacity of participating states to become involved in the studying and monitoring of the Earth and its environment.

Its main goals are: to provide for continuity and stability of the observations started with the ERS satellites, including those obtained from radar-based observations; to enhance the ERS mission, specifically the ocean and ice mission; to increase the observed geographical area to help to better understand the parameters

that effect the environment; to make a significant contribution to environmental studies, notably in atmospheric chemistry and ocean studies (including marine biology).

These are together with two secondary objectives: to allow more effective monitoring and management of the Earth's resources; to better understand the processes of solid Earth.

The mission intends to continue and improve the measurements began by ERS-1 and ERS-2, it will take into account the requirements related to the global study and monitoring of the environment. The mission is an essential part in providing long-term continuous data sets that are crucial for addressing environmental and climatological issues. It will at the same time push for a gradual change in the use of remote sensing data from experimental to operational exploitation.

Envisat, as an undertaking of ESA member states plus Canada, constitutes a major contribution to the international effort of space agencies worldwide to provide the data and information required to further the understanding, modeling, and prediction of environmental and climatic changes. Figure 1.2 shows the ground tracks of ERS-2 (EnviSat) around Taiwan.
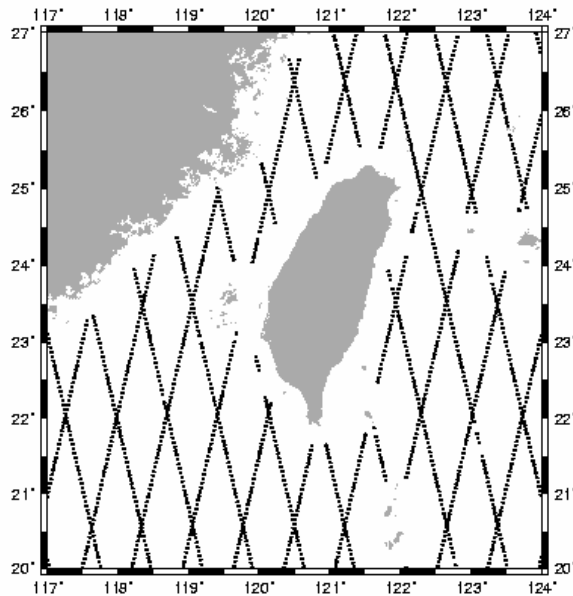
Figure 1.2: The ground tracks of EnviSat around Taiwan.

(3) Jason-1

JASON-1 is a follow-on mission to the highly successful TOPEX/POSEIDON (T/P) mission. It was developed by the French Space Agency, the Centre National d'Etudes Spatiales (CNES) and the United States National Aeronautics and Space Administration (NASA), for the study of global circulation from space. The mission uses the technique of satellite altimetry to make precise and accurate observations of sea level for several years. Jason-1 continues Topex/Poseidon's observations of ocean surface topography to monitor world ocean circulation. It studies interactions of the oceans and atmosphere, improves climate predictions and observes events like El Nino.

The main goal of this mission is to measure the sea surface topography with the same quality as T/P. The mission will provide a large continuous time series of highly-accurate measurements of the ocean topography from which scientists can determine the general circulation of the ocean, and understand its role in the Earth's

climate. In addition to the primary JASON-1 IGDR and GDR data products provided with a 5 and 30 day latency, respectively, JASON-1 also supports the preparation of operational ocean services by providing a non-validated near-real-time (3 hour latency) JASON-1 data product, the Operational Sensor Data Record (OSDR). JASON-1 is the first in a twenty-year series of satellites to take over from T/P, marking the start of operational satellite altimetry.

The global oceans are Earth's main storehouse of solar energy. Jason-1's measurements of sea-surface height reveal where this heat is stored, how it moves around Earth by ocean currents, and how these movements affect the weather and climate. Jason-1 is designed to directly measure climate change through very precise millimeter-per-year measurements of global sea-level changes.

Weighing 500 kilograms (about 1,100 pounds), Jason-1 is one-fifth the size of Topex/Poseidon. Jason-1 flew together with Topex/Poseidon until Topex/Posiedon stopped working, this doubled the scientific data measured. Figure 1.3 shows the ground tracks of Jason-1 around Taiwan.
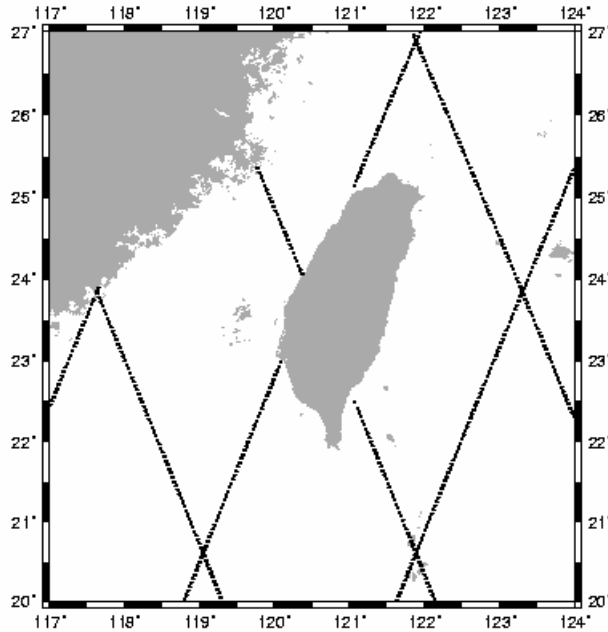
Figure 1.3: The ground tracks of Jason-1 around Taiwan.

(4) Jason-2: WSOA (Wide-Swath Ocean Altimeter)

A pulse-limited radar altimeter such as T/P provides profiles of sea-surface height along the satellite's ground tracks with a spatial resolution of 6-7 km. Such profiles may be used to obtain information about ocean surface currents and the marine gravity field. However, this measurement is basically one-dimensional and does not provide a complete picture of the vector field of ocean currents and gravity anomalies. In order to map the sea-surface height in two dimensions with comparable resolutions, this new type of radar instrument, WSOA, has been developed at JPL using the principle of radar interferometry (Fu, 2003).

WSOA is based on a technique that combines altimeter and interferometer measurements. Below is a summary cited from Fu and Rodriguez (2004). WSOA is a wide-field radar altimeter able to measure sea-surface height across a swath centered on the satellite ground track. The WSOA is designed to be flown with a Jason-1–class,

conventional dual-frequency altimeter system, including a multifrequency radiometer for the correction of the effects of water vapor in the troposphere. By flying with a Jason-1–class altimeter, the WSOA will be able to measure the ocean surface topography over a swath that is 200 km wide, with rms accuracy ranging from 4.2 cm (inner swath) to 5.3 cm (outer swath) at a spatial resolution of 15 km. Shown in Figure 1.4 is the configuration of WSOA as part of a Jason-class altimeter mission (Fu and Rodriguez, 2004). Within its 10-day orbit-repeat period (the same as for TOPEX/POSEIDON and Jason-1), the WSOA will make at least two measurements at a given resolution cell at most mid, and high-latitude locations. One can make use of these multiple observations to either enhance the temporal resolution or reduce the measurement errors by averaging the observations. The capability of the WSOA is equivalent to that of the formation flight of more than five nadir-looking conventional altimeters. Figure 1.5 shows the coverage of WSOA in the Jason 10-day repeat orbit. Note that a substantial portion of the ocean surface is covered more than once.

The most important application of the WSOA is to provide the first synoptic maps of the global oceanic eddy field. The strong currents and water property anomalies (in temperature, salinity, oxygen, etc.) associated with ocean eddies are a major factor affecting the general circulation of oceanic and maritime operations such as offshore oil drilling, ship routing, fisheries, and distribution of marine debris. The WSOA is expected to be an essential part of the future ocean-observing system for addressing these applications. The WSOA will also provide measurements for monitoring and studying coastal currents and tides.
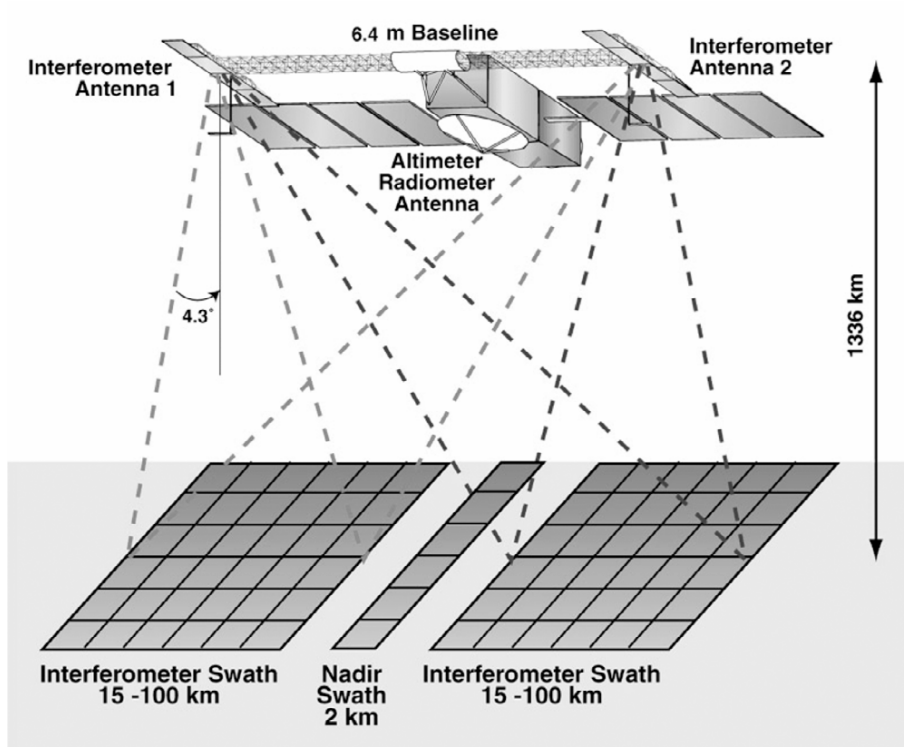
Figure 1.4: Conceptual operation of the WSOA instrument to measure a 200-km swath. (Fu and Rodriguez, 2004)
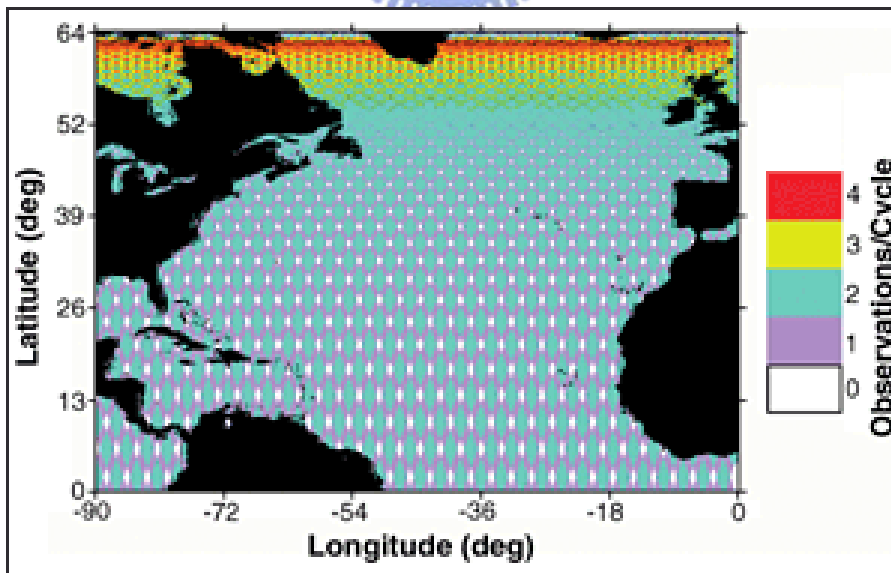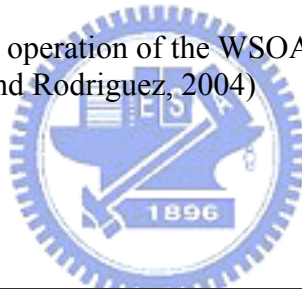
Figure 1.5: Coverage map for WSOA showing the number of observations per 10-day cycle for a 200-km swath. (Fu and Rodriguez, 2004)

1.2 Objectives and Outline

The main objective of this dissertation is the improvement of global and local marine gravity anomaly derivations from multi-satellite altimeter data. Early such works, can be found in Hwang and Parsons (1995), Andersen et al. (1996), Sandwell and Smith (1997), Hwang et al. (1998). Based on this objective, there are several main issues to be studied in this dissertation:

Chapter 1 introduces the background, development and the latest missions of Satellite Altimetry. The objectives and thesis outline are also given in Chapter 1.

In Chapter 2, an overview about marine gravity field from satellite altimetry is described. Four existing computation methods developed with different altimeter data types to compute gravity anomaly are reviewed and the basic concept of altimeter data and observations are introduced, in preparation for demonstrating the database of multi-satellite altimeter used in this study. Multi-satellite altimeter data processing such as the choice of model and the geophysical corrections are also discussed in Chapter 2.

Global model of mean sea surface height (MSSH) and gravity anomaly on a 2 minute by 2 minute grid will be determined in Chapter 3. Comparisons of the global MSSH model with the T/P and the ERS-1 MSSH are carried out and discussed. The RMS differences between the predicted and shipborne gravity anomalies are computed in 12 areas of the world's oceans.

In Chapter 4, issues concerning gravity anomaly recovery over shallow waters are investigated and tests are carried out . A method will be introduced that uses to detect outliers in altimeter data and to filter the non-repeated mission data. Several

examples from repeated and non-repeated mission data will be tested. Two methods with three kinds of data types of gravity anomaly computations were introduced and compared in the East China Sea (ECS) and the Taiwan Strait (TS) in order to find the best parameters and method with a new data type -differenced height.

Chapter 5 compares global gravity anomaly models and tide models to analyze the errors in altimeter-gravity conversion over shallow waters. Case studies and analysis will be performed over the ECS and the TS. The best method given in section 4.3 will demonstrate the case of using land data in enhancing the accuracy of altimeter-derived gravity anomalies.

In Chapter 6, conclusions and recommendations are given.

CHAPTER 2

MARINE GRAVITY ANOMALIES RECOVERY BY SATELLITE ALTIMETER DATA

2.1 Introduction

With the advent of satellite altimetry, the applications of satellite altimeter data have been extensively investigated. One of the major applications is to recover gravity information from satellite altimetry data. Several methods for gravity derivation from altimetry exist, e.g., least-squares collocation (LSC), inverse Vening Meinesz Formula, FFT with Deflection of Vertical (DOV), the inverse Stokes integral. This chapter will discuss these methods.
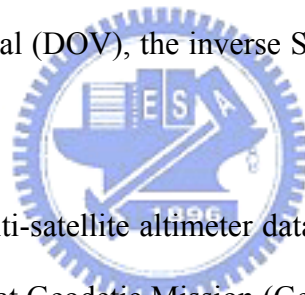
In this study, we use multi-satellite altimeter data – Seasat, Geosat Exact Repeat Mission (Geosat/ERM), Geosat Geodetic Mission (Geosat/GM), ERS-1 35-day repeat mission (ERS-1/35-daay), ERS-1/GM and TOPEX/POSEIDON (T/P)- in the gravity and mean sea surface height derivation. With altimeter data from such a variety of satellite missions, a good data management system and data processing is important and will be discussed in this chapter.

2.2 Marine Gravity Field from Altimetry

2.2.1 Overview

A review of altimeter contribution to gravity field modeling is given below. Satellite altimetry will keep its role in gravity even if there are improvements through

the gravity satellite missions. Altimetry is able to map the mean sea surface and gravity anomaly with a spatial resolution of 2'x2' or higher (Hwang et al., 2002). A 2'x2'-resolution corresponds to a harmonic degree beyond 2000. The gravity field models of GOCE will not go beyond degree 300. Thus the high frequency information of the marine gravity filed will be mainly based on satellite altimetry. However, due to the low density of shipboard and seafloor gravity measurements, satellite altimetry provides the most valuable data sets for the recovery of the marine gravity field.

Since the advent of satellite altimetry, investigators created numerous local and global marine gravity field models using a variety of successful techniques. According to Fu and Cazenave (2001), the first regional (Haxby et al., 1983), and global (Haxby, 1987) color portrayals, created from the 1978 Seasat data, demonstrated the promising potential of satellite altimetry for the global recovery of the marine gravity field. The results Haxby are based on the planar spectral method of using two-dimensional fast Fourier transform (FFT) to convert the altimeter-derived sea-surface slopes to gravity anomalies on flat-earth domains. In an alternate study, a global simultaneous recovery of the sea-surface height and the marine gravity anomaly field was developed from the Seasat data (Rapp, 1983) using the least-squares collocation technique.

The planar spectral method and the least-squares collocation are the most widely used tools in the short-wavelength marine gravity recovery. The major advantage of the least-squares collocation is that randomly spaced heterogeneous data can be combined and gravity anomalies can be derived in grid or discrete. Besides, this method has the capability to give accuracy estimates for the computed gravity anomalies. As such, the accuracy of the result depends on the accuracy of the statistical information used. However, the LSC is numerically cumbersome and needs more computer time, so the FFT is another commonly used method. On the other

16

hand, the spectral method has great simplicity and computational efficiency when compared with any least-squares techniques.

Up to 2007, all marine areas within the area 82°S to 82°N and 0°to360°E longitude have been covered with sufficient altimetric observations to derive the global marine gravity field on a 2 minute by 2 minute resolution, corresponding to 3.6 by 3.6 km at the Equator. Numerous local and global marine gravity anomalies have been created using a variety of successful techniques (e.g., Haxby (1987), Sandwell (1992), Tscherning et al. (1993), Hwang et al. (1998)). Numerous comparisons between marine observations and altimetry-derived gravity anomalies have been presented, e.g., Hwang and Parsons (1995), Sandwell and Smith (1997), Andersen and Knudsen (1998), Hwang et al. (1998). Using the high-density data collected from multi-satellite missions, the precision of the derived global gravity fields is reported to range from 3 to 14 mgal (Hwang et al., 2003) based on the comparisons between shipborne and altimeter-derived results.

Detailed knowledge of the gravity anomalies are used for a variety of purposes, such as the guidance of aircrafts, and spacecrafts over geophysical exploration purposes, over bathymetry, and understanding of the tectonics, territorial claims.

2.2.2 Remove-restore Technique

The gravity derivations in this work are all based on the remove-restore procedure. In this procedure, a reference gravity field is needed. The choice of reference field has been somewhat arbitrary in the literature, eg., Sandwell and Smith (1997), Hwang (1989) and Rapp and Basic (1992) chose to use degree 70, 180 and 360 fields, respectively (note that the gravity models are also different). Wang's (1993)

theory suggests the use of a reference field of the highest degree, provided that the geopotential coefficients are properly scaled by the factor S_n given by

$$S_n = \frac{C_n}{C_n + \varepsilon_n} \tag{2.1}$$

where C_n and ε_n are the degree variance and the error degree variance of the chosen reference field. Wang's theory was tested by Hwang & Parsons (1996) and, in the case of OSU91A (Rapp, Wang and Pavlis, 1991), the scaling factors improve slightly the accuracy of the computed gravity anomalies. In Hwang et al. (1998), EGM96 model was used to see whether the scaling factor S_n is necessary. The results show that the use of S_n does not increase the accuracy of the computed gravity anomalies in the two test areas, the Reykjanes Ridge and the South China Sea. This is due to the fact that EGM96's high-degree coefficients are substantially improved compared to OSU91A, since S_n has a larger effect on the high-degree coefficients than on the low-degree ones.

2.2.3 Altimeter Data Types

It has been shown by, e.g., Hwang and Parsons (1995), Sandwell and Smith (1997), that use of geoid gradients for derivation of gravity anomaly from altimetry is more stable than doing so using geoidal heights and can reduce the effect of long wavelength errors in altimeter data. A typical long wavelength error is orbit error. Another advantage of using geoid gradients is that we do not need to adjust the sea-surface height as in Knudsen (1987). In the following three kinds of altimeter data types are introduced and will be used for predicting gravity anomaly.

Taking the first horizontal derivatives of the altimeter-sensed sea surface heights along-track yields the negative deflections of the vertical at the geoid. Along-track DOV is defined as

$$\varepsilon = -\frac{\partial h}{\partial s} \qquad (2.2)$$

where h is geoidal height obtained from subtracting dynamic ocean topography from sea surface height (SSH), and s is the along-track distance. In using DOV satisfactory result can be obtained without crossover adjustment of SSH, and this is especially advantageous in the case of using multi-satellite altimeter data. The problem with Equation (2.2) is that DOV can only be approximately determined because along-track geoidal heights are given on discrete points.

A data type similar to along-track DOV is differenced height defined as

$$d_i = h_{i+1} - h_i \qquad (2.3)$$

where i is index. Using differenced height has the same advantage as using along-track DOV in terms of mitigating long wavelength errors in altimeter data. We go one step forwards by using "height slope" defined as

$$\chi_i = \frac{h_{i+1} - h_i}{s_i} \qquad (2.4)$$

where s_i is the distance between points associated with h_i and h_{i+1}. The advantage of using height slope is similar to that of using DOV and differenced height in terms of

error reduction.

2.3 Methods of Marine Gravity Anomalies From Altimetry

Seasat, Geosat, ERS-1/ERS-2 and TOPEX/POSEIDON satellite altimetry missions have collected a vast amount of data over ocean areas. These data enable us to determine the marine gravity field with unprecedented resolution and accuracy. Practical computations of marine gravity anomalies and geoid heights from satellite altimetry data have been carried out for more than two decades; e.g., see Koch (1970), Balmino et al. (1987), Basic and Rapp (1992), Hwang (1989), Rapp (1985), Zhang and Blais (1993) and Zhang and Sideris (1995). Here we introduce four methods of gravity anomalies from satellite altimetry. The overview below only provides a brief outline and the reader is referred to the cited literature for the exact details of the theories and computational procedures.

2.3.1 Method 1: Least Squares Collocation

The application of conventional (space domain) LSC in physical geodesy has been discussed in detail by Moritz (1980). Its practical applications in gravity field modeling can be found in, e.g., Tscherning (1974), Rapp (1985) and Basic and Rapp (1992). A fast frequency domain LSC method was studied by Eren (1980). Examples of the use of LSC to calculate gravity anomalies are the works by Rapp (1979,1985), Hwang (1989), and Rapp & Basic (1992), who all used altimeter data alone. The LSC method needs more computer time but has the capability to combine heterogeneous data and to give accuracy estimates for the computed gravity anomalies. The conventional LSC method and derived formulae by using of different altimeter data types will be introduced in this section

Using geoidal heights as observations, the prediction of gravity anomalies evaluated by the LSC method can be expressed as:

$$\Delta g = C_{\Delta gh}(C + D)^{-1}h \qquad (2.5)$$

where $C_{\Delta gh}$ is the covariance matrix between gravity anomalies Δg and h, C and D are the observations and error covariance matrices which are geoidal heights observed by altimetry.

If geoid heights $h^{'}$ and shipborne gravity anomalies Δg' are used simultaneously, the LSC formula reads

$$\left\{ \begin{matrix} h \\ \Delta g \end{matrix} \right\} = \begin{bmatrix} C_{hh'} & C_{h\Delta g'} \\ C_{\Delta gh'} & C_{\Delta g\Delta g'} \end{bmatrix}$$

$$\left\{ \begin{bmatrix} C_{hh} & C_{h\Delta g} \\ C_{\Delta gh} & C_{\Delta g\Delta g} \end{bmatrix} + \begin{bmatrix} D_{hh} & 0 \\ 0 & D_{\Delta g\Delta g} \end{bmatrix} \right\}^{-1} \left\{ \begin{matrix} h' \\ \Delta g' \end{matrix} \right\} \qquad (2.6)$$

$$C_{ee}(\Delta g) = C_{\Delta g\Delta g} - \begin{bmatrix} C_{\Delta gh'} & C_{\Delta g\Delta g'} \end{bmatrix}$$

$$\left(\begin{bmatrix} C_{hh} & C_{h\Delta g} \\ C_{\Delta gh} & C_{\Delta g\Delta g} \end{bmatrix} + \begin{bmatrix} D_{hh} & 0 \\ 0 & D_{\Delta g\Delta g} \end{bmatrix} \right)^{-1} \begin{bmatrix} C_{h'\Delta g} \\ C_{\Delta_g'\Delta g} \end{bmatrix} \qquad (2.7)$$

where $C_{ee}(\Delta g)$ is the error covariance matrix of Δg.

To use differenced height for gravity estimation, again one may employ LSC.

First, the covariance function between two differenced heights is

$$\text{cov}(d_i, d_j) = \text{cov}(h_{i+1} - h_i, h_{j+1} - h_j)$$

$$= \text{cov}(h_{i+1}, h_{j+1}) - \text{cov}(h_{i+1}, h_j) - \text{cov}(h_i, h_{j+1}) + \text{cov}(h_i, h_j) \qquad (2.8)$$

The covariance function between gravity anomaly and differenced height is

$$\text{cov}(\Delta g, d_i) = \text{cov}(\Delta g, h_{i+1} - h_i)$$

$$= \text{cov}(\Delta g, h_{i+1}) - \text{cov}(\Delta g, h_i) \qquad (2.9)$$

The needed covariance functions of using height slope are then

$$\text{cov}(\chi_i, \chi_j) = \frac{1}{s_i s_j} \text{cov}(d_i, d_j) \qquad (2.10)$$

$$\text{cov}(\Delta g, \chi_i) = \frac{1}{s_i} \text{cov}(\Delta g, d_i) \qquad (2.11)$$

The spectral characteristics of height slope are the same as DOV and gravity anomaly as they are all the first spatial derivatives of earth's disturbing potential.

With differenced height or height slope, gravity anomaly can be computed using the standard LSC formula

$$\Delta g = C_{sl}(C_l + C_n)^{-1} l \qquad (2.12)$$

where vector *l* contains differenced heights or height slopes, C_l and C_n are the signal and noise parts of the covariance matrices of *l*, and C_{sl} is the covariance matrix of gravity anomaly and differenced height or height slope. Differenced height or height slope can also be used for computing geoidal undulation: one simply replaces C_{sl} by the covariance matrix of geoid and differenced height or height slope in Equation (2.12). Furthermore, for two consecutive differenced heights along the same satellite pass, a correlation of -0.5 exits and must be taken into account the C_n matrix in Equation (2.12).

Next formula uses along-track DOV defined in (2.2.3) and the LSC method for gravity anomaly derivation (Hwang and Parsons, 1995). For this method, the covariance function between two along-track DOV is needed and is computed by

$$C_{\varepsilon\varepsilon} = C_{ll}\cos(\alpha_{\varepsilon_p} - \alpha_{pq})\cos(\alpha_{\varepsilon_q} - \alpha_{pq}) + C_{mm}\sin(\alpha_{\varepsilon_p} - \alpha_{pq})\sin(\alpha_{\varepsilon_q} - \alpha_{pq}) \qquad (2.13)$$

where α_{ε_p} and α_{ε_q} are the azimuths of DOV at point *p* and *q*. respectively, and C_{ll} and C_{mm} are the covariance functions of longitudinal and transverse DOV components, respectively and α_{pq} is the azimuth from *p* to *q*. The covariance function between gravity anomaly and along-track DOV is computed by

$$C_{\Delta g\varepsilon} = \cos(\alpha_{\varepsilon_Q} - \alpha_{QP})C_{l\Delta g} \qquad (2.14)$$

where $C_{l\Delta g}$ is the covariance function between longitudinal component of DOV and gravity anomaly. C_{ll}, C_{mm} and $C_{l\Delta g}$ are isotropic functions depending on spherical

distance only. With these covariance functions, gravity anomaly can be computed

by LSC as in Equation (2.12) using along-track DOV for l and covariance matrices

computed with $C_{\varepsilon\varepsilon}$ and $C_{\Delta g\varepsilon}$ for C_l and C_{sl}. For the detail of this method, see

Hwang and Parsons (1995).

2.3.2 Method 2: Inverse Vening Meinesz Formula

This method employs the inverse Vening Meinesz formula (Hwang, 1998) to

compute gravity anomaly. The inverse Vening Meinesz formula reads:

$$\Delta g_p = \frac{\gamma}{4\pi}\iint_\sigma H'\left(\xi_q \cos\alpha_{qp} + \eta_q \sin\alpha_{qp}\right)d\sigma_q$$

$$= \frac{\gamma}{4\pi}\iint_\sigma H'\varepsilon_{qp}d\sigma_q \tag{2.15}$$

where p is the point of computation, γ is the normal gravity, ξ_q and η_q are the north

and east components of DOV, α_{qp} is the azimuth from point q to point p, and H' is

the kernel function defined by

$$H' = -\frac{\cos\dfrac{\psi_{pq}}{2}}{2\sin\dfrac{\psi_{pq}}{2}} + \frac{\cos\dfrac{\psi_{pq}}{2}\left(3 + 2\sin\dfrac{\psi_{pq}}{2}\right)}{2\sin\dfrac{\psi_{pq}}{2}\left(1 + \sin\dfrac{\psi_{pq}}{2}\right)} \tag{2.16}$$

where ψ_{pq} is the spherical distance between the computation point p and the moving

point q of the integration, see also Figure 2.1. In the practical computation, the 1D

FFT method is used to implement the spherical integral in Equation (2.15). For the 1D FFT computation, the two DOV components ξ_q and η_q are prepared on two regular grids. We use LSC to obtain ξ_q and η_q on the grids along-track DOV by LSC, see also Hwang (1998).
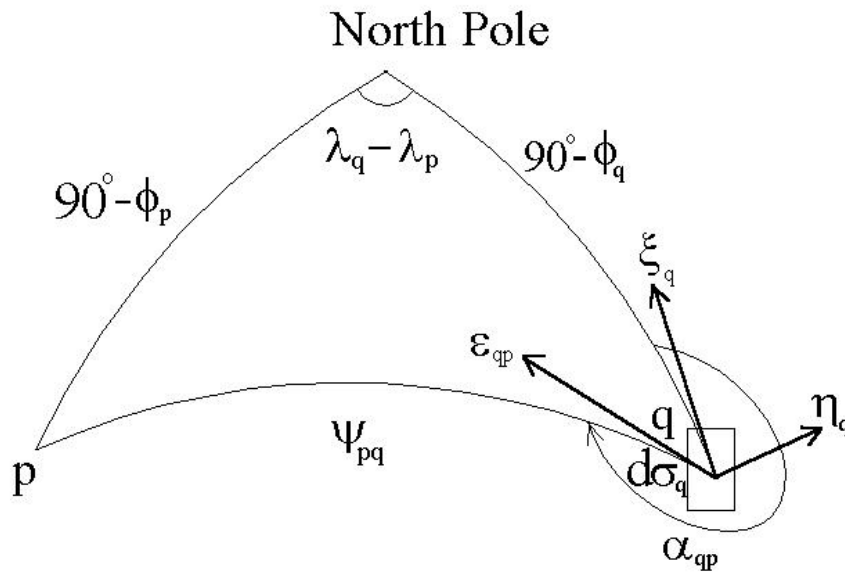
Figure 2.1: Geometry for the inverse Vening-Meinesz formula

2.3.3 Method 3: Fourier Transform with Deflection of Vertical

In this approach, complete grids of east and north deflections of vertical are computed and the conversion is achieved using the relationship between gravity anomalies and deflections of vertical formulated via Laplace's equation (e.g. Haxby et al., 1983; Sandwell, 1992; Sandwell and Smith, 1997).

The geoid height h and gravity anomaly $\triangle g$ cane derived from the disturbing potential T by simple operations.. To a first approximation, the geoid height is related

to the disturbing potential by Bruns' formula,

$$h \cong \frac{1}{\gamma} T \qquad (2.17)$$

where γ is the normal gravity of the earth. The gravity anomaly is the vertical derivative of the potential,

$$\Delta g = -\frac{\partial T}{\partial z} \qquad (2.18)$$

the east component of deflection of vertical is the slope of the geoidal height in the x-direction,

$$\eta = -\frac{\partial h}{\partial x} \cong \frac{-1}{\gamma} \frac{\partial T}{\partial x}, \qquad (2.19)$$

and the north component of deflection of vertical is the slope of the geoidal height in the y-direction,

$$\xi \equiv -\frac{\partial h}{\partial y} \cong \frac{-1}{\gamma} \frac{\partial T}{\partial y} \qquad (2.20)$$

These quantities are related to Laplace's equation in rectangular coordinates:

$$\frac{\partial^2 T}{\partial x^2} + \frac{\partial^2 T}{\partial y^2} + \frac{\partial^2 T}{\partial z^2} = 0 \qquad (2.21)$$

According to Sandwell and Smith (1997), the relationship between the vertical gravity

gradient and the sum of x and y derivatives of the east and north deflection of vertical

is:

$$\frac{\partial \Delta g}{\partial z} = -\gamma \left[\frac{\partial \eta}{\partial x} + \frac{\partial \xi}{\partial y} \right] \qquad (2.22)$$

In the frequency domain, Equation (2..2) becomes

$$F\{\Delta g\} = \frac{j\gamma}{\sqrt{u^2 + v^2}} \left(uF\{\eta\} + vF\{\xi\} \right) \qquad (2.23)$$

where $j = \sqrt{-1}$. Thus, by inverse FT we have

$$\Delta g = \gamma F^{-1} \left\{ j \frac{1}{\sqrt{u^2 + v^2}} \left(uF\{\eta\} + vF\{\xi\} \right) \right\} \qquad (2.24)$$

where u and v are spatial frequencies corresponding to x and y.
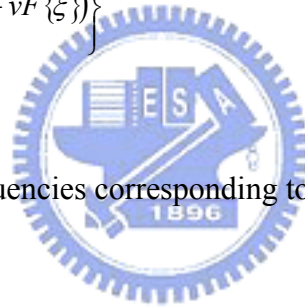
2.3.4 Method 4: Inverse Stokes Integral

In this case marine geoid heights from altimetry are converted to gravity anomalies using the inverse of Stokes integral formulas. According to Heiskanen and Moritz (1967), the Stokes' integral equation can be expressed as:

$$h = \frac{R}{4\pi\gamma} \iint_\sigma \Delta g S(\psi) d\sigma \qquad (2.25)$$

where σ is the unit sphere; R is the mean radius of the Earth; Δg is the free air

27

gravity anomaly on a surface of the sphere of radius R; S(ψ) is the Stokes kernel function, given by

$$S(\psi) = \frac{1}{\sin(\psi/2)} - 6\sin\frac{\psi}{2} + 1 - 5\cos\psi - 3\cos\psi \ln[\sin\frac{\psi}{2} + \sin^2(\frac{\psi}{2})] \qquad (2.26)$$

when ψ is small, S(ψ) can be written as:

$$S(\psi) \approx \frac{1}{\sin(\psi/2)} \approx \frac{1}{\psi/2} = \frac{2}{\psi} \qquad (2.27)$$

By the planar approximation, Equation (2.25) can be expressed as the convolution between gravity anomaly and Stokes function in Equation (2.28). That is (Wang, 1999):

$$h(x,y) = \frac{1}{2\pi\gamma}\Delta g * l_h(x,y) \qquad (2.28)$$

where " * " is the convolution operator, and $l_h(x,y) = (x^2 + y^2)^{-1/2}$,

The corresponding frequency-domain version of Equation (2.28) is

$$\tilde{h}(u,v) = \frac{1}{\gamma}\Delta\tilde{g}(u,v)L_h(u,v) \qquad (2.29)$$

where $\Delta\tilde{g}(u,v)$ is the Fourier transform of gravity anomaly, $L_h(u,v) = (u^2 + v^2)^{-1/2}$,

The above equation can be used to recover gravity anomaly from geoidal heights. That is,

$$\Delta g = \gamma F^{-1}\left(\omega \widetilde{N}(u,v)\right) \tag{2.30}$$

where $\omega = \sqrt{u^2 + v^2}$, such a transformation from geoidal heights into free-air gravity anomalies uses a differentiation operator, which enhances the high frequencies and it is sensitive to noise (Andersen and Knudsen, 1998).

2.4 Radar Altimeter Data

2.4.1 Altimetry Data and Observations

During the last two decades altimetry has been available from the following satellites listed in Table2.1. Altimetry increased vastly in accuracy from meters to centimeters (Wunch and Zlotniki, 1984, Fu and Cazenave, 2001), and has opened for a whole new suite of scientific problems that can now be addressed using altimetry. One of these is the ability to perform a high-resolution mapping of the Earth's marine gravity field. Table 2.1 shows the specifications for selected satellite missions.

Table 2.1: Specifications for satellite missions.

Satellite	Mission Duration	Orbit Inclination (degrees)	Repeat Period (days)	Noise (m)
Seasat	1978	108	-	0.20
Geosat	1984-1988	108	~3, 17	0.08
ERS-1	1991-1996	98	3, 35, 168	0.04
ERS-2	1995-2005	98	35	0.03
T/P	1992-2006	66	~10	0.01
Jason-1	2001-2005	66	~10	0.01
EnviSat	2002->now	98	35	0.02

After the altimetric range observations have been corrected for orbital, range and geophysical corrections (Fu and Cazenave, 2001), they provide mean sea surface height for gravity derivation. The surface height can be described according to the following expression in its most simple form:

$$h = N + \xi + e \tag{2.31}$$

where

N is the geoid height above the reference ellipsoid,

ξ is the sea surface topography

e is the error (treated below).

In geodesy the geoid N or the geoid slope is the important signal. In oceanography the sea surface topography ξ is of prime interest.

The geoid N can be described in terms of a long wavelength geoid N_{REF}, geoid contributions from nearby terrain N_{DTM} and residuals ΔN to this. Similarly, the sea surface topography can be described in terms of a mean dynamic topography (ξ_{MDT}) and a time varying or dynamic sea surface topography ($\xi(t)$). Some minor contributions h_s to sea level is also seen from aliased barotropic motion and atmospheric pressure loading. Therefore, sea surface height can then be written as (ref. Figure 2.1):

$$h = N_{REF} + N_{DTM} + \Delta N + \xi_{MDT} + \xi(t) + h_s \tag{2.32}$$

The magnitudes of these contributions are :

The geoid N_{REF} +/- 100 meters

Terrain effect N_{DTM} +/- 30 centimeters

Residual geoid ΔN +/- 2 meters

Mean dynamic topography ξ_{MDT} +/- 1.5 meter

Dynamic topography $\xi(t)$ +/- 1 meters.

Aliased barotropic motion and

atmospheric pressure loading h_s +/- 10 centimeters

In order to enhance the signal to noise of the residual geoid height ΔN used for geoid and gravity field modeling in this study, as many contributors to sea level variation as possible should be modeled and removed.
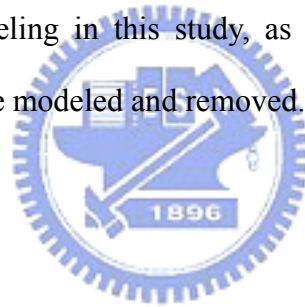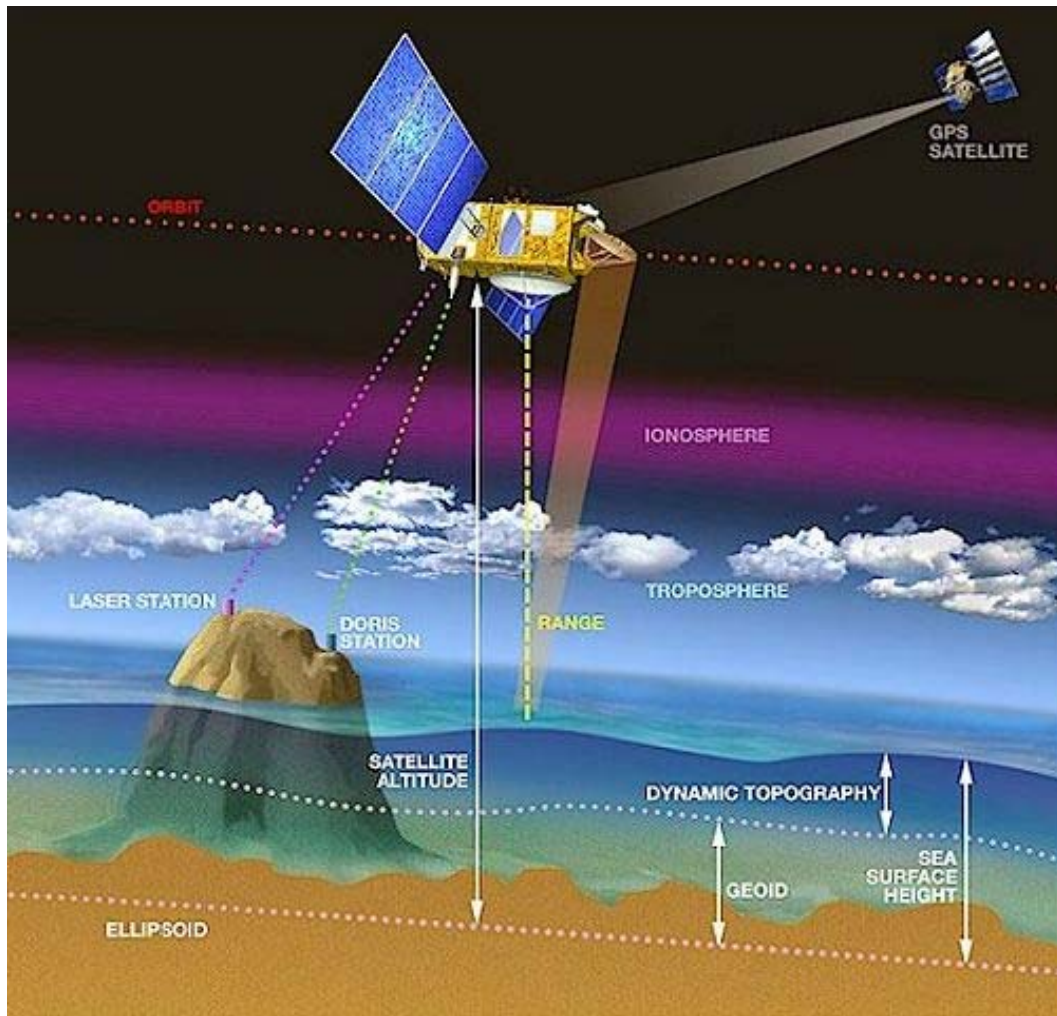
Figure 2.2: Schematic illustration of the measurement principle (from http://www.aviso.oceanobs.com/html/alti/principe_uk.html).

2.4.2 Time-averaging of SSH

The repeated ground tracks of altimetric satellites do not exactly coincide with each other, and the separations of them is about 1 or 2 km. In order to reduce the anomalous temporal changes of SSH caused by some significant oceanographic phenomena, such as EL Nino or La Nina occurred during particular seasons or years, the altimetric SSH data from repeat missions is time-averaged for all available cycles and the mean tracks are obtained.

Mean track is derived from a selected reference tracks and the related collinear tracks. After the reference tracks are determined, the SSH at each point of the collinear tracks corresponding to the point of the reference track can be computed. Altimeter data from repeated missions used in this study are also processed to get the mean sea surface, more details can be found in Hsu (1997).

2.5 Multi-Satellite Altimeter Data Processing

2.5.1   Multi-Satellite Altimetry Data Base

The satellite altimeter data used in this study were from the National Chiao Tung University (NCTU) altimeter data base. Table 2.2 lists the altimeter data used in computing the global MSSH and gravity anomaly grids. The data are from five satellite missions and span more than 20 years. The Seasat data are from the Ohio State University and are edited by Liang (1983), who also have crossover adjusted the Seasat orbits. The Geosat data are from National Oceanic and Atmospheric Administration and contain the latest JGM3 orbits and geophysical correction models (NOAA, 1997). In the Geosat/GM JGM3 GDRs, the wet and dry troposphere corrections are based on the models of National Centers for Environmental Prediction (NCEP)/National Center for Atmospheric Research (NCAR) (Kalnay et al., 1996）and NASA Water Vapor Project (NVAP) (Randel et al., 1996), and the ionosphere correction is adopted from the IRI95 model (Bilitza, 1997). The sea state bias, which introduces an error to the measured range, is also recomputed and is more accurate than the previous version of GDRs. The ERS-1 and ERS-2 data are from Centre ERS d'Archivage et de Traitement (CERSAT)/France and their orbits have been adjusted to

the T/P orbits by Le Traon and Ogor (1998). Finally, the T/P data are provided by Archiving, Validation, and Interpretation of Satellite Oceanographic Data (AVISO) (1996) and should have the best point data quality among all altimeter data, due to the low altimeter noise and the state-of-the-art orbit and geophysical correction models.

The Geosat/GM and ERM GDRs from NOAA contain both raw measurements at 10 samples per second (10 Hz) and the one-second averaged SSH. To increase spatial resolution, we re-processed the raw data to obtain SSHs at 2 samples per second. When re-sampling, the 10-Hz SSHs were first approximated by a second-degree polynomial and the desired 2 per second (2 Hz) SSHs were then computed from the solve-for polynomial coefficients. Pope's (1976) tau-test procedure was used to screen any erroneous raw data. Among these data sets, Geosat/GM and ERS-1/GM have very high 2-D spatial density and will contribute most to the high-frequency parts of MSSH and gravity fields. In one test over the SCS we used separately the new JGM3 and the old T2 versions of Geosat/GM altimeter data to predict gravity anomalies and it was found the root mean square (RMS) differences between the predicted and shipborne gravity anomalies are 10.65 and 9.77 mgals, respectively. Thus the JGM3 version indeed outperforms the T2 version.

Table 2.2: Satellite altimeter missions and data used for the global computation

Mission	Repeat period (day)	Data duration	Orbit height (km)	Inclination angle (°)	mean track separation at the equator (km)
Seasat	no	78/8-78/11	780	108	165
Geosat/GM	no	85/03-86/09	788	108	4
Geosat/ERM	17	86/11-90/01	788	108	165
ERS1-/35d	35	92/04-93/12 95/03-96/06	781	98.5	80
ERS-1/GM	no	94/04-95/03	781	98.5	8
ERS-2/35d	35	95/04-98/10	785	98.5	80
T/P	10	92/12-00/06	1336	66	280

2.5.2 Averaging SSH to Reduce Variability and Noise

The altimeter data from the repeat missions (Geosat/ERM, ERS-1/35d, ERS-2/35d and T/P) were averaged to reduce time variability and data noise. When averaging, Pope's (1976) tau-test procedure was also employed to eliminate erroneous observations. But it turns out that the Geosat observed SSHs behave erratically (for example, large jump of SSHs in along-track observations) and Pope's method failed to detect outlier SSHs in several occasions. Thus for Geosat/ERM a modified averaging/outlier rejection procedure was used. In this new procedure, at any locations SSHs from repeat cycles were first sorted to find the median value. Then, the difference between individual SSHs and the median were computed. Any SSH with difference larger than 0.45 m is flagged as an outlier and removed. (0.45 is based on three times point standard deviation of Geosat/ERM, see below). The desired MSSH is finally computed from the cleaned SSH by simple averaging. Table 2.3 lists the statistics associated with the averaged and non-averaged SSHs. For the repeat missions in Table 2.3, we computed the point standard deviation (SD) of SSH as

$$\sigma_h(i,j) = \sqrt{\frac{\sum_{k=1}^{n}(h(i,j,k) - \bar{h}(i,j))^2}{n-1}} \tag{2.33}$$

where $h(i,j)$ is the observed SSH at point i along pass j, $\bar{h}(i,j)$ is the averaged SSH and n is the number of points. According to the statistical theory, the SD of averaged height $\bar{h}(i,j)$ is

$$\sigma_{\bar{h}}(i, j) = \frac{\sigma_h(i, j)}{\sqrt{n}} \tag{2.34}$$

Thus the accuracy increases with number of repeat cycles. A point SD can be expressed as

$$\sigma_h = \sqrt{\sigma_i^2 + \sigma_o^2 + \sigma_g^2 + \sigma_s^2} \tag{2.35}$$

where

σ_i : instrument error (random part + time-dependent part)

σ_o : orbit error (random part + non-geographical correlated error)

σ_g : errors in geophysical correction models (random + systematic errors)

σ_s : sea surface variability (excluding tidal variation)
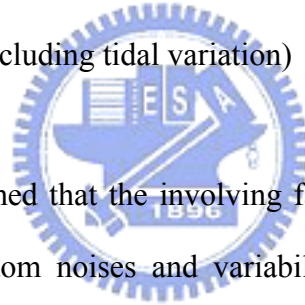
In Equation (2.35) it is assumed that the involving factors are uncorrelated. Thus, a point SD contains both random noises and variabilities arising from a variety of sources. Figure 2.3 shows the point SDs derived by averaging Geosat/ERM, ERS-1/35d and T/P. (ERS-2/35d SD is close to ERS-1/35d SD, so it is not shown here). Clearly the SDs from the three repeat missions have the same patterns of distribution. Over oceanic areas of high variability such as the Kuroshio Extension, the Gulf Stream, the Brazil Current, the Agulhas Current and the Antarctic Circumpolar Currents, sea surface variability contributes most to SD. SD is also relatively high in the tropic and the western Pacific areas, where mesoscale eddies are very active. Clearly, the pattern of sea surface variability is very stable over the past two decades, as the Geosat/ERM-derived SDs in the 1980s and the ERS-1 and T/P–derived SDs in the 1990s show very consistent signature. In the polar regions (above ±67º), SD will be less reliable because of ice contamination and sparse data

samples. Over shallow waters, tide model error becomes dominant in SD and is particularly pronounced in the continental shelves of the western Pacific, the northern Europe and the eastern Australia. In the immediate vicinity of coasts, the interference of altimeter waveforms by landmass further increases SD. Over the deep, quiet oceans, SD is in general very small and here along-track MSSH will be best determined. Note that in Table 2.3 the SD of Geosat/GM is simply the SD of the 2-Hz SSHs as derived from the fitting of the 10-Hz SSHs, so it does not represent the noise level of 2-Hz SSHs.

Table 2.3: Statistics of SSHs from seven satellite altimeter missions

Mission	No. of repeat cycles	No. of passes	No. of points	No. points in deep ocean[a]	Averaged std dev. of SSH[b] (m)
Seasat	no	3314	1269169	6419	—
Geosat/GM	no	15708	25530238	151044	0.141
Geosat/ERM	68	488	1991672	4798	0.026
ERS1-/35d	26	1002	1677190	4805	0.023
ERS-1/GM	no	9532	14702377	44928	—
ERS-2/35d	37	1002	1141786	4815	0.022
T/P	239	254	553525	1387	0.009

[a]Over the area 25º S to 15º S and 235º E -245º E where there is no land
[b]The SD of Geosat/GM is the SD of 2-Hz SSHs from fitting the 10-Hz SSHs

2.5.3 Choice of ocean tide model

Ocean tide creates a deviation of the instantaneous sea surface from the mean sea surface. There are now more than 10 global ocean tide models (Shum et al., 1997) available for correcting tidal effect in altimetry. Table 2.4, partly from Matsumoto et al. (2000), shows the RMS collinear differences of T/P and the errors in along-track DOV using NAO99b (Matsumoto et al., 2000), CSR4.0 (Eanes, 1999) and GOT99.2b

37
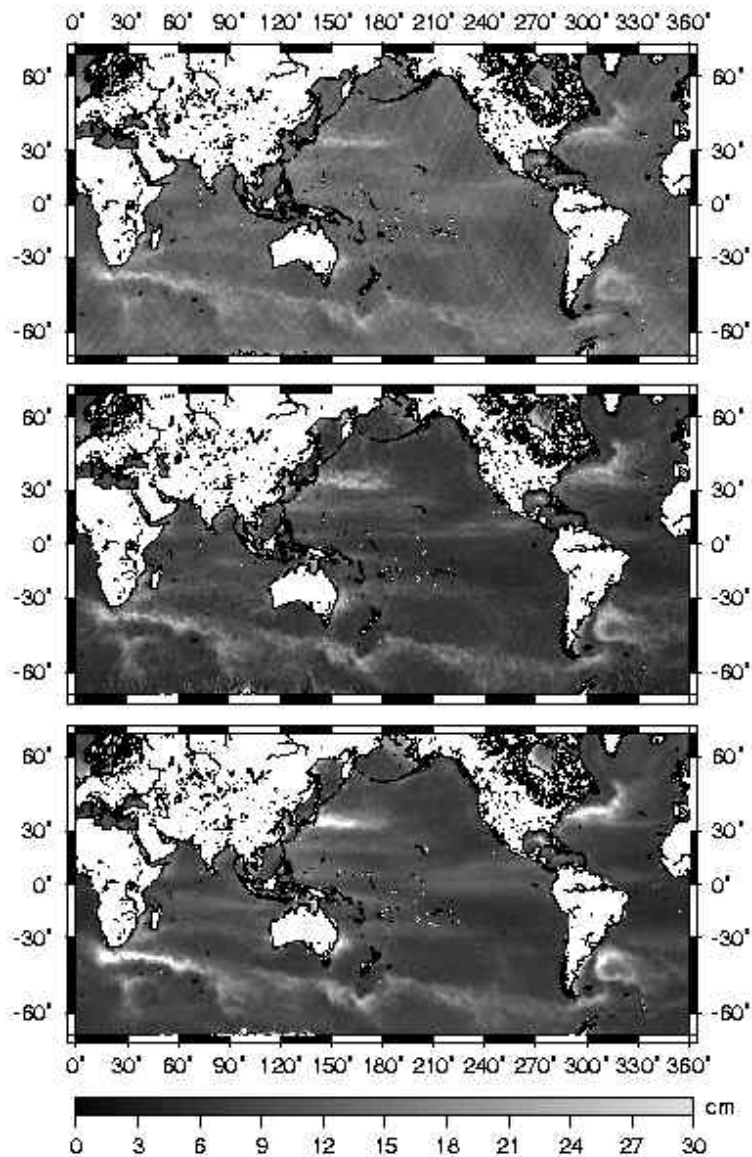
Figure 2.3: Estimated standard deviations of point SSH of Geosat/ERM (top), ERS-1 (center) and TOPEX/POSEIDON (bottom)

(Matsumoto et al., 2001) tide models. Both NAO99b and GOT99.2b are based on hydrodynamic solutions and a further enhancement by assimilating T/P altimetry data into the solutions. The CSR tide models (3.0 and 4.0 versions) use the orthotide approach to model the residual tides of some preliminary hydrodynamic oceans tide

models using T/P altimeter data. From Table 2.4, it seems that NAO99b is the best

model among the three. Using T/P SSHs, Chen (2001) found that the NAO99b tide

model yields the smallest RMS crossover differences of SSH compared to the CSR4.0

and GOT99.2b tide models. Over shallow waters, all the collinear differences exceed

10 cm, which translate to a 48-µrad (10^{-6} radian) error in DOV of Geosat/GM. Even in

the deep oceans, the collinear difference-implied DOV errors are still very large.

Using available resources here, we conducted a test over the SCS to compare the

accuracies of predicted gravity anomalies using the CSR3.0, CSR4.0 and GOT99.2b

tide models. As shown in Table 2.5, the NAO99b tide model produces the best

accuracy in gravity anomaly. However, as seen in Table 2.5, the differences in

accuracy are very close. This should be partly due to the fact that DOV is insensitive

to long wavelength tide model error. For Geosat/ERM, ERS-1/35d, ERS-2/35d and

T/P, the use of CSR3.0, CRS4.0 and NAO99b will probably not make too much

difference because of the reduction of tide model error by averaging data from repeat

cycles.

Table 2.4: RMS collinear differences (in cm) of T/P (Matsumoto et al. 2000) and corresponding error (in µrad) in along-track DOV of Geosat/GM using different tide models

Tide model	$0 < H^a < 0.2$		$0.2 < H < 1$		$1 < H$	
	Difference	Error	Difference	Error	Difference	Error
NAO99b	11.20	45	6.98	28	8.56	35
CSR4.0	15.77	64	7.37	30	8.55	35
GOT99.2b	13.99	57	7.37	30	8.65	35

[a]H: ocean depth in km

Table 2.5: RMS differences (in mgals) between shipborne and altimeter-derived gravity anomalies with different tide models

Tide model	ERS-1/GM	Geosat/GM (JGM3)
NAO99b	11.90	9.77
CSR3.0	11.93	Not available
CSR4.0	Not available	9.78

CHAPTER 3

GLOBAL MODELS OF MEAN SEA SURFACE AND GRAVITY ANOMALY

3.1 Introduction

Satellite altimetry has begun a new era in earth sciences research. Mean sea surface height (MSSH) and marine gravity anomaly are the most two important products of satellite altimetry for geodetic and geophysical applications. MSSH is useful in numerous applications such as global tide modeling, sea level change study, reduction of altimeter observations to reference tracks, and bathymetry prediction. Applications of marine gravity have been illustrated in, e.g., Sandwell and Smith (1997). Ignoring the sea surface topography (SST), marine gravity anomaly is basically equivalent to MSSH, and the two have a simple, linear relationship in the spectral domain. Current global MSSH models have been largely constructed by direct gridding of altimeter observed sea surface heights (SSHs), e.g., the MSSH models of Kort-og Matrikelstyrelsen (KMS) (Andersen and Knudsen, 1998), National Aeronautics and Space Administration (NASA)/Goddard Space Flight Center (GSFC) (Wang, 2000) and Collecte Localisation Satellites (CLS) (Hernandez and Schaeffer, 2000). A somewhat unconventional approach was employed by Yi (1995), who used a combined SSH and geoid gradient from multi-satellite missions to construct the OSU95 MSSH model, see also Rapp and Yi (1997). When using the direct gridding method, SSHs must be carefully crossover adjusted to remove inconsistency of SSHs at crossover points. Insufficient or improper crossover points

will easily lead to artifacts in the resulting field such as track pattern and extremely large signature.　With MSSH computed, marine gravity anomaly can be obtained by a simple conversion in the spectral domain, see, e.g., Schwarz et al. (1990) for a complete derivation of the spectral conversion between MSSH and gravity anomaly (assuming that SST is removed).

As discussed in (2.2.3), using deflections of the vertical (DOV) as the data type is one of the choices in gravity anomaly recovery from satellite altimetry data. The major argument of using DOV is that DOV is less contaminated by long wavelength errors than SSH, and using DOV requires no crossover adjustment; see, e.g., Sandwell and Smith (1997), Hwang et al. (1998), and Andersen and Knudsen (1998). With DOV from altimetry, it is possible to compute MSSH using the deflection-geoid formula derived by Hwang (1998).　Taking the advantage of DOV, in this chapter we will compute simultaneously a global MSSH grid and a global gravity anomaly grid by the deflection-geoid and the inverse Vening Meinesz formulae from multi-satellite altimetry data. In parallel to this study is the latest models of ocean tide and other geophysical corrections.

3.2 Forming north and east components of DOV

3.2.1 Computing along-track DOV

The methods for computing MSSH and gravity anomaly in this paper will use DOV as the data type. By definition, an along-track DOV is the geoid gradient with an opposite sign:

$$g = -\frac{\partial N}{\partial s} \qquad (3.1)$$

where N is the geoid, which is a surface function, and s is the along-track distance. By this definition one would need to first construct a surface of the geoid and then perform directional derivative along s to get DOV. Following this concept, we first fit a cubic spline (De Boor, 1978) to the along-track geoidal heights from altimetry. Then the along-track derivative is obtained by differentiating the spline. The actual numerical computations were done by the International Mathematical and Statistical Library (IMSL) routines. It turns that such a procedure results in very noisy DOV, which should be due to the interpolation error in fitting the spline. The interpolation error is particularly large when point intervals along a track segment are not uniform. Although this approach seems rigorous, it did not produce good results. A better result is obtained by simply approximating DOV by the slope of two successive geoidal heights:

$$g \doteq -\frac{(N_2 - N_1)}{d} \qquad (3.2)$$

where d is the point spacing. The geographic location of g is the mean location of the two geoidal heights. The estimated standard deviation of g is simply

$$\sigma_g = \frac{\sqrt{\sigma_1^2 + \sigma_2^2}}{d} \qquad (3.3)$$

where σ_1 and σ_2 are the standard deviations of N_1 and N_2, respectively. In order to obtain geoidal height from SSH, both the time-dependent and quasi-time independent

SST values should be removed. In this paper, the time-dependent SST is reduced by filtering, and for the quasi time-independent SST we adopt the model of Levitus et al. (1997), which is available at NOAA's Ocean Climate Laboratory (see http://www.nodc.noaa.gov/OC5/dyn.html). The Levitus SST values from NOAA are given as monthly averages on a 1º×1º grid for 12 months. We averaged the monthly values to get the needed quasi time-independent SST. Figure 3.1 shows the averaged Levitus SST, which looks very similar to the 1982 version of Levitus SST (cf: Hwang, 1997, Fig. 3). The divided difference method (Gerald and Wheatley, 1994) is then used to interpolate the needed SST value from this SST grid at any altimeter data point.
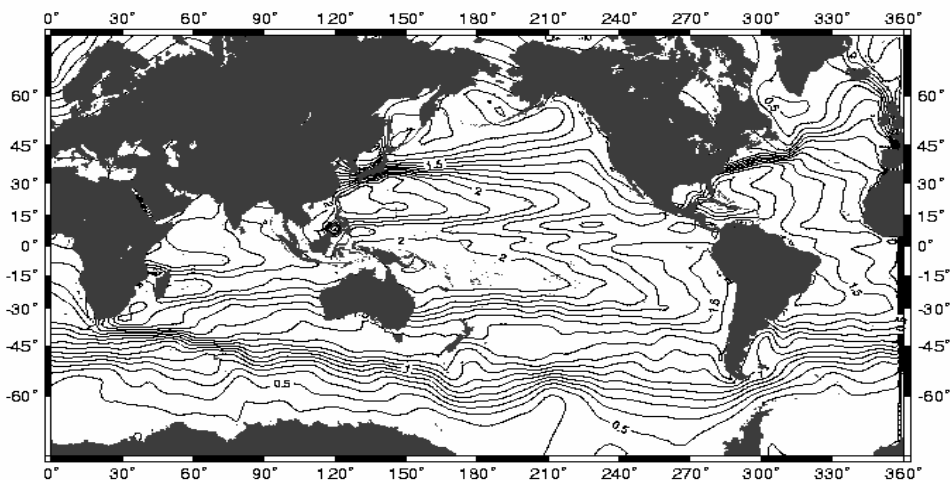
Figure 3.1: Quasi time-independent sea surface topography from Levitus et al. (1997), contour interval is 10 cm.

3.2.2 Removing Outliers and Gridding DOV

Because of the use of 1D FFT algorithm in the computations of MSSH and gravity anomaly (see below), the north and east components of DOV need to be formed on regular grids with constant intervals in latitude and longitude. Before

forming the regular grids, erroneous along-track DOV must be removed. Again we adopt Pope's tau-test method to remove possible outliers. Within a $4' \times 4'$ cell, any along-track DOV, ε_i, can form an observation equation as (cf: Heiskanen and Moritz, 1985, p. 187)

$$\varepsilon_i + v_i = \xi \cos\alpha_i + \eta \sin\alpha_i, \ i = 1, \ldots, n \tag{3.4}$$

where v_i is the residual, α_i is the azimuth of ε_i and n is the number of points, ξ and η are the north and east components. After least-squares estimating ξ and η, all residuals in the $4' \times 4'$ cell can be determined using Equation (3.4). A DOV is flagged as an outlier and is removed if its residual satisfies the condition:

$$\frac{|v_i|}{\sigma_{v_i}} > \tau_c(m) \tag{3.5}$$

where σ_{v_i} is the estimated standard deviation of v_i and $\tau_c(m)$ is the critical tau-value at degree of freedom of m; see Koch (1987, p.336) and Pope (1976) for the methods of computing σ_{v_i} and $\tau_c(m)$. Table 3.1 shows the ratios between removed and raw DOV in 12 selected areas. The removed DOV are largely from the non-repeat missions. In general, the removal ratios are relatively high in shallow waters and in higher latitudes, e.g., Ross Sea, and low in the open ocean, e.g., the Reykjanes Ridge and the East Pacific Rise. One problem with the above procedure of outlier removal is that, in areas with sparse data such as coastal regions and polar regions, there are not enough data points to produce large degree of freedom to make the result of the tau-test reliable, leading to undetected/improperly detected outliers.

After removing outliers the north and east components are then computed on a regular grid by the method of LSC (Moritz, 1980):

$$\mathbf{s} = \begin{pmatrix} \xi \\ \eta \end{pmatrix} = \mathbf{C_{sl}}(\mathbf{C_{ll}} + \mathbf{C_n})^{-1}\mathbf{l} \qquad\qquad (3.6)$$

Table 3.1: Test areas and ratios of removed outliers

Area	Geographic boundaries (latitude, longitude)	Total no. of. points	Deleted no. of points	Ratio of outliers
(1) Alaska Abyssal	$44° - 61°$, $99° - 221°$	696082	27224	3.9%
(2) East Pacific Rise	$-26° - -9°$, $229° - 251°$	809120	27474	3.4%
(3) Caribbean Sea	$9° - 31°$, $269° - 291°$	609605	29404	4.8%
(4) Reykjanes Ridge	$49° - 66°$, $319° - 341°$	800624	29949	3.7%
(5) Sierra Leone Basin	$-11° - 11°$, $339° - 361°$	855408	28254	3.3%
(6) Mediterranean Sea	$29° - 46°$, $0° - 31°$	202545	17506	8.6%
(7) Carlsberg Ridge	$-1° - 21°$, $49° - 71°$	564600	25819	4.5%
(8) Kerguelen Plateau	$-66° - 44°$, $59° - 81°$	611084	41032	6.7%
(9) South China Sea	$4° - 26°$, $104° - 126°$	495338	27478	5.5%
(10) Mariana Trench	$4° - 26°$, $139° - 161°$	1001211	33606	3.3%
(11) Fiji Plateau	$-31° - 9°$, $159° - 181°$	982678	33875	3.4%
(12) Ross Sea	$-71° - -59°$, $199° - 181°$	458505	38042	8.2%

where vector **l** contains along-tack DOV, vector **s** contains north (ξ) and east (η)components, $\mathbf{C_{sl}}$, $\mathbf{C_{ll}}$ and $\mathbf{C_n}$ are the covariance matrices for **s** and **l**, **l** and **l**, and the noise of **l**, respectively. In Equation (3.6), $\mathbf{C_n}$ is a diagonal matrix that in theory contains the variances of along-track DOV. When a reference gravity model is used, the error of the gravity model must be taken into account in constructing the covariance functions, see Hwang and Parsons (1995) and Hwang et al. (1998) for the methods of constructing the covariance functions when gridding DOV by LSC.

3.3 Conversions from DOV to MSSH and gravity anomaly

We use the deflection-geoid and inverse Vening Meinesz formulae as the basic tool for computing MSSH and gravity anomaly. The deflection-geoid formula transforms DOV into geoidal height, which then yields MSSH by adding the quasi time-independent SST. Detailed derivations of these two formulae are given in Hwang (1998). These two formulae read

$$\begin{Bmatrix} N_p \\ \Delta g_p \end{Bmatrix} = \frac{1}{4\pi} \begin{Bmatrix} R \\ \gamma \end{Bmatrix} \iint_\sigma (\xi_q \cos\alpha_{qp} + \eta_q \sin\alpha_{qp}) \begin{Bmatrix} C' \\ H' \end{Bmatrix} d\sigma_q \qquad (3.7)$$

where

N_p : geoidal height at p (free index)

Δg_p : gravity anomaly at p

R: mean earth radius, 6371000 m is used

γ : normal gravity, based on GRS80 (Torge, 1989)

C' and H' : Kernel functions

ξ_q, η_q : north and east components of DOV at q (dummy index)

α_{qp} : azimuth from q to p

σ : unit sphere

$d\sigma_q$: surface element = $\cos\phi_q d\phi_q d\lambda$ and ϕ_q, λ_q are latitude and longitude

The kernel functions C' and H' are functions of spherical distance only and are defined in Hwang (1998). The 1D FFT algorithm is used to rigorously implement

Equation (3.7). In the case of using a 360-degree reference field (see below), an optimal effective radius of integration in Equation (3.7) is about 110 km (about 1° at the equator). In the 1D FFT algorithm, all geoidal heights or gravity anomalies at a fixed latitude (or parallel) are computed simultaneously (Hwang, 1998), and this is why the 1D FFT algorithm is faster than the strait sum algorithm.

Because of the singularity of the kernel function C' and H' at zero spherical distance, the inner most zone effects on geoidal height and gravity anomaly must be taken into account and are computed by

$$\begin{Bmatrix} N_i \\ \Delta g_i \end{Bmatrix} = \frac{1}{4}(\xi_y + \eta_x)\begin{Bmatrix} s_0^2 \\ 2s_0\gamma \end{Bmatrix} \tag{3.8}$$

where $\xi_y = \partial\xi/\partial y, \eta_x = \partial\eta/\partial x$ (x is positive to the east and y is positive to the north), s_0 is the size of innermost zone, which can be estimated from the grid intervals as

$$s_0 = \sqrt{\frac{\Delta x \Delta y}{\pi}} \tag{3.9}$$

Formulae such as those in Equation (3.9) are based on spherical approximation. Errors arising from spherical approximation are investigated in detail by Moritz (1980). When using the remove-restore procedure, error in using spherical approximations should be very small compared to data noises. Consider the formula of error-free LSC in the case of using ellipsoidal correction (Moritz, 1980, p. 328)

$$\mathbf{s} = \mathbf{C_{sl}}\mathbf{C_{ll}^{-1}}(\mathbf{l} - e^2\mathbf{l^1}) + e^2\mathbf{s^1} \tag{3.10}$$

where $\mathbf{s}$, $\mathbf{l}$, $\mathbf{C_{sl}}$ and $\mathbf{C_{ll}^{-1}}$ are defined in Equation (3.6) and e^2 is the squared eccentricity of a reference ellipsoid, which is about 0.006694 for the GRS80 ellipsoid. The procedure in Equation (3.10) is first to remove the ellipsoidal effect of the data, $e^2\mathbf{l^1}$, perform LSC computation and finally add back the ellipsoidal effect of the signal $e^2\mathbf{s^1}$. In the case of using remove-restore procedure where a reference field is removed from the data and the residual signal is to be recovered, both $\mathbf{l^1}$ and $\mathbf{s^1}$ will be very small compared to their full signals (see Moritz (1980), p. 327, where the low degree part will vanish due to the use of a reference field). For example, if the largest element (DOV) in $\mathbf{l^1}$ is 100 µrad, then the largest element in $e^2\mathbf{l^1}$ will be 0.66 µrad. This value is far smaller than the noise of DOV from the multi-satellite altimetry. Furthermore, if the largest element in $\mathbf{s^1}$ is 100 mgal, then the largest ellipsoidal effect on gravity anomaly is 0.66 mgal, which is much smaller than the error of the recovered gravity anomaly. Of course, whether the reference field used in the remove-restore procedure will introduce additional error is another issue.
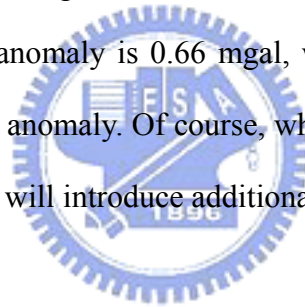
3.4 Computation and Analysis of Global MSS Model

After the tests performed in the previous sections and the selection of a set of optimal parameters, MSSH and gravity anomalies on a 2′×2′ grid were computed over the area: 80ºS-80ºN and 0º-360ºE. The computations were divided into 36 areas, each covering a 40º×40º area. A batch job was created for each of the 36 areas and this batch job creates maps of altimeter data distribution, predicted MSSH and gravity anomaly, and many statistics for detailed examinations. The final global MSSH and gravity anomaly grids are the combination of the results from the 36 areas. Figure 3.2 shows the flowchart of computation in a 40º×40º area. The most time-consuming part

in the procedure is the gridding of DOV. Only few minutes of CPU time is needed for the 1D FFT computation of geoid or gravity anomaly in a 40º×40º area on a Pentium III 600 machine. This computational procedure uses the EGM96 gravity model (Lemoine et al., 1998) to harmonic degree 360 as the reference field. In summary, reference DOV implied by EGM96 were removed from the raw DOV to yield residual DOV, which were used to compute residual geoidal heights and gravity anomalies using Equation (3.7). The final geoidal heights and gravity anomalies are obtained by adding back the EGM96-implied values.

As seen in Figure 3.2, the procedure for obtaining the global MSSH grid is more involved than that for the gravity anomaly grid. A preliminary MSSH grid was first obtained by adding the 1994 Levitus SST to the geoid grid. Because of the use of DOV as data type, it is possible that the long wavelength part of MSSH is lost in using the deflection-geoid formula. To mitigate such a loss, we first computed the differences between the along-track T/P, ERS-1 MSSH and the preliminary MSSH. Each difference is associated with a weight, which is the inverse of noise variance. Then smoothing and de-aliasing of the differences were made by computed the weighted median values within 15′×15′ cells. The weighted median values were then interpolated on a 15′×15′ grid using the minimum curvature method (Smith and Wessel, 1990). The final MSSH grid is obtained by summing the difference grid (which is now re-sampled into a 2′×2′ grid) and the preliminary grid. The resulting grids are now designated as the NCTU01 MSSH grid and the NCTU01 gravity grid.

Because of the final adjustment using T/P MSSH, The SSH from the global MSSH grid is the height above a geocentric ellipsoid with a semi-major axis= 6378136.3 m, and flattening=1/298.257222101. The geodetic coordinates of both global grids are geodetic latitudes and longitudes defined by the T/P coordinate frame.

In addition, the normal gravity for the global gravity anomaly grid is GRS80 because we have removed the zonal spherical harmonic coefficients C_{20}, C_{40}, C_{60} and C_{80} of the GRS80 reference ellipsoid (cf: Torge, 1989) when computing the reference gravity anomalies from EGM96

A standard method for evaluating a MSSH grid is to compare modeled MSSH and MSSH-derived gradients with averaged SSH and gradients from repeat missions. The first comparison is for the MSSH values from our model and from repeat missions. Table 3.2 shows the result of the comparison of MSSH values using the averaged along-track SSH from T/P and ERS-1. Also included in Table 3.2 are the comparisons for NASA/GSFC model (Wang, 2000) and the CLS model (Hernandez and Schaeffer, 2000). Compared to the NASA /GSFC and CLS models, the NCTU01 model agrees best with the T/P and the ERS-1 MSSH. The GSFC MSSH is slightly worse than the NCTU01 MSSH. On the continental shelves (depths below 200 m), all MSSH models contain large errors, which in the case of CLS has exceeded 20 cm. Even in the median depths, the accuracy of MSSH is not very promising and is generally worse than 10 cm. All MSSH models have the best accuracy of few cm in the deep oceans. The differences in the case of ERS-1 are smaller than in the case of T/P. This is to be explained by the fact that ERS-1 has a higher data density than T/P, so the former will dominate the resulting MSSH model. As such, the MSSH model will have a better match with the ERS-1 SSH than T/P SSH.   Furthermore, Figure 3.3 shows the differences between the NCTU01 and T/P MSSH. Again the differences in Figure 3.3 are large over shallow waters and small in the deep oceans. It is noted that the pattern of differences is very similar to the pattern of ocean variability in Figure 2.3.
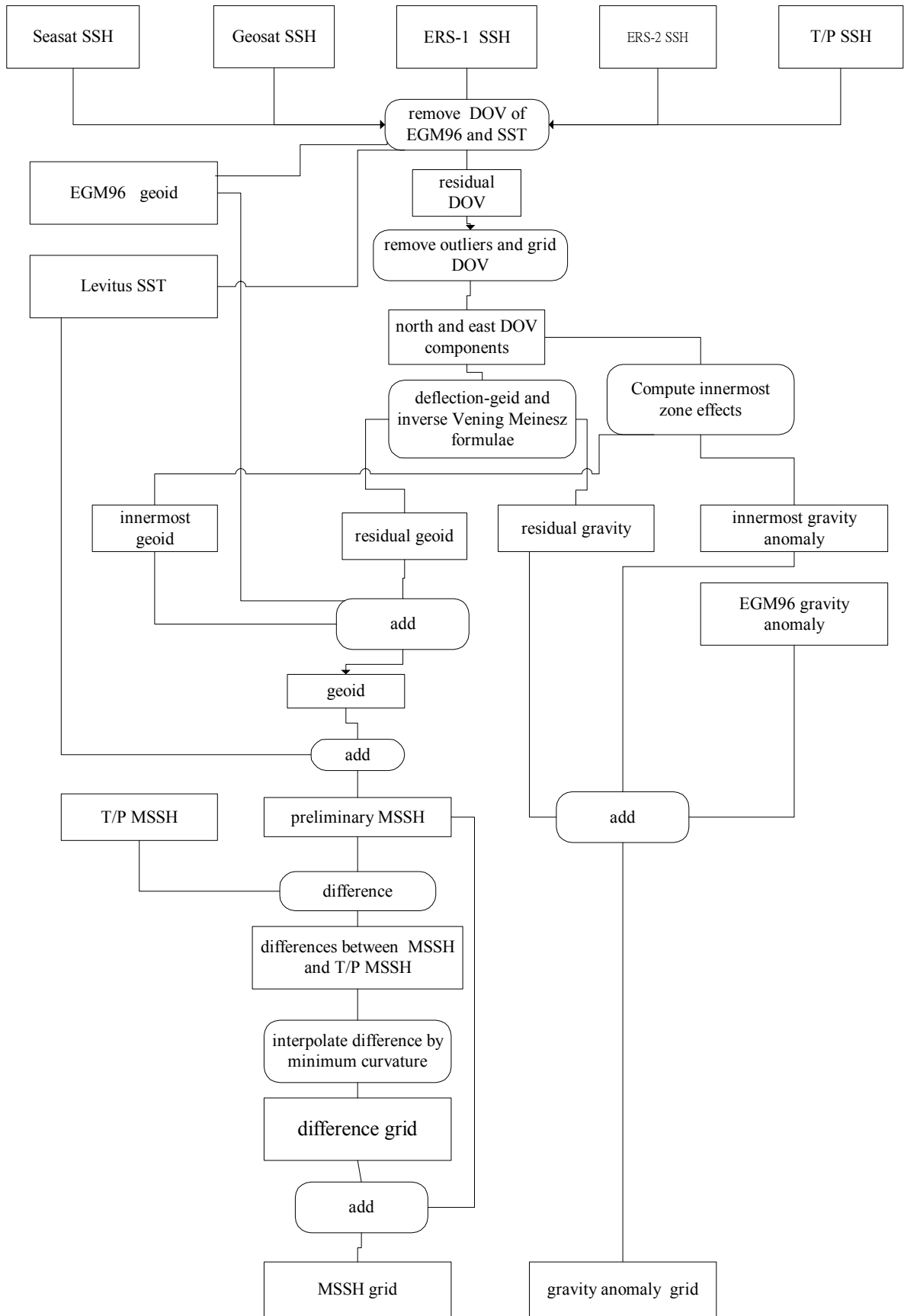
Figure 3.2: Flowchart for computing global MSSH and gravity anomaly grids

This shows that the MSSH is less reliably determined in areas of high ocean variability than in other areas. Such a result agrees with the expected outcome of least-squares collocation (see Equation (3.6)): data with larger noises (variability) yield less reliable results.

Table 3.2: RMS differences (in cm) between global sea surface models and T/P and ERS-1 MSSH

	T/P				ERS-1			
	0-0.2[a]	0.2-1	1-10	0-10	0-0.2	0.2-1	1-10	0-10
NCTU01	16.5	10.6	1.9	5.0	6.8	4.2	2.7	3.1
CLS	24.7	26.1	3.9	9.0	12.2	8.8	4.7	5.4
GSFC00	19.4	13.5	2.0	6.0	10.7	7.6	3.6	4.3
No. points	34824	23015	485762	543601	63828	48296	1517901	1630025

[a] Depths from 0 to 0.2 km

Figure 3.3: Difference between NCTU01 and T/P mean sea surface heights

Table 3.3 shows the RMS differences in gradients between the NCTU01, GSFC and CLS modeled gradients and the averaged along-track gradients from T/P and ERS-1 missions. The NCTU01 and GSFC models have almost the same level of accuracy, while the CLS model has a slightly poorer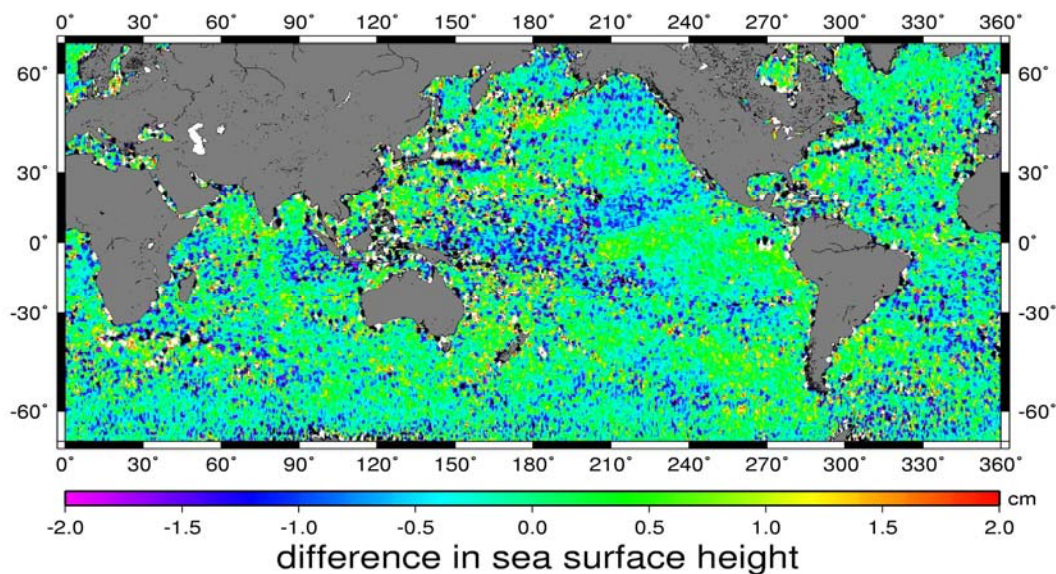 accuracy than the two. For all models the distribution of error is the same as that of MSSH error, namely, bad accuracy over shallow waters and good accuracy in the deep oceans. Again, for the reason of data dominance, the error in the ERS-1 case is smaller than the error in the T/P case. In the T/P case the RMS difference of 7-9 μrad has far exceeded than the standard deviation of T/P gradient, which is 1.9 μrad based on Equation (3.3) (with an averaged point spacing of 6.6 km, see Table 2.2). On the other hand, in the ERS-1 case the RMS difference of 3.2 μrad agrees well with the expected standard deviation of 4.7μrad of ERS-1 gradient.

Table 3.3: RMS differences in along-track sea surface height gradients (in μrad) derived from global sea surface models and from T/P and ERS-1 MSSH

	T/P				ERS-1			
	0-0.2[a]	0.2-1	1-10	0-10	0-0.2	0.2-1	1-10	0-10
NCTU01	23.3	16.7	2.4	7.1	7.1	5.0	2.8	3.2
CLS	26.4	19.9	2.9	9.0	8.7	5.3	2.8	3.3
GSFC00	22.9	16.9	2.3	7.0	7.3	4.3	2.8	3.2
No. points	33687	22814	485561	542062	61374	47071	1510808	1619253

[a] Depths from 0 to 0.2 km

3.5 Computation and Analysis of Global Gravity Anomaly Model

To evaluate the accuracy of the NCTU01 gravity grid, we made comparison between the predicted and shipborne gravity anomalies in 12 areas in the world oceans (see Table 3.1 for the boundaries). These shipborne gravity data are from the National Geophysical Data Center. The corresponding ship tracks are shown in Figure 3.4. The 12 areas are so selected that deep and shallow waters, and low and high latitudes are covered in the comparison. The comparing procedure and the adjustment of shipborne gravity data were detailed in Hwang et al. (1998). Briefly, long wavelength biases in the shipborne gravity anomalies were first adjusted using altimetry-derived gravity anomalies. A pointwise comparison was then made for the adjusted shipborne gravity anomalies. Table 3.4 shows the result of the comparison. In Table 3.4, the gravity grid from Hwang et al. (1998) is also compared. It has been shown that the gravity grid of Hwang et al. (1998) has a better accuracy than that of Sandwell and Smith's (1997). As shown in Table 3.4, the accuracy of the current gravity grid has indeed improved over the gravity grid of Hwang et al. (1998). The improvement is most dramatic in the deep oceans such as the East Pacific Rise. In the Caribbean Sea, the improvement is also significant. Other areas with significant improvements are the Ross Sea and Kerguelen Plateau, which are situated in the Antarctica. In general, large difference between predicted and shipborne gravity anomalies may be due to either or both of the following reasons: (1) bad altimeter data quality, including data scarcity, and (2) large gravity signatures, for example, in areas with trenches and seamounts. The largest difference in the Fiji Plateau and then the Mediterranean Sea should be attributed to the first reason. Due to possibly bad

tide correction and contamination of altimeter waveforms by land mass and reefs, the predicted gravity anomalies in the Fiji Plateau are not expected to be in good quality. A recent detailed analysis of errors in altimeter-derived gravity anomalies is given by Trimmer et al. (2001). To have a dramatic improvement of gravity accuracy in such an area, a better tide model and improved determination of SSH by retracking altimeter waveforms will be needed. Improved SSHs by wave retracking have been reported in, e.g., Anzenhofer and Shum (2001), Deng et al. (2001), and Fairhead and Green (2001).
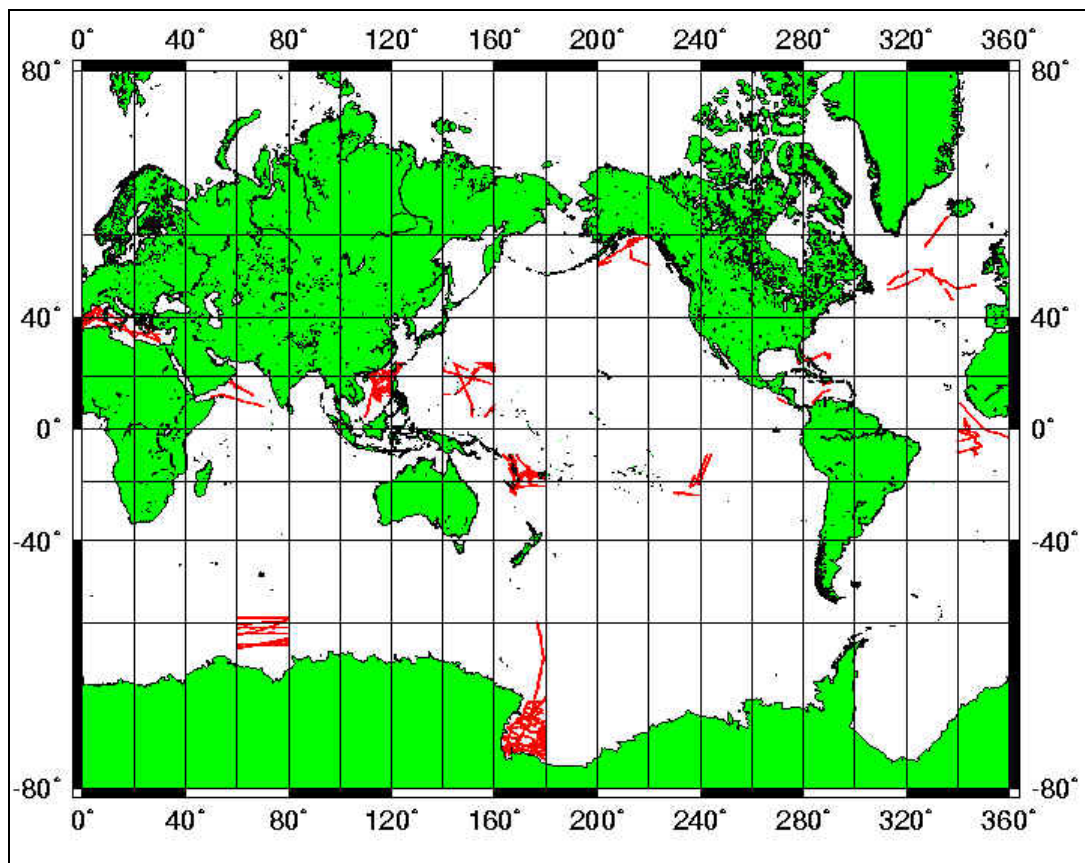

Figure 3.4: Distributions of shipborne gravity anomalies in the 12 areas where the NCTU01 gravity anomaly grid is evaluated.

Table 3.4: RMS differences (in mgal) between predicted and shipborne gravity anomalies in 12 areas

Comparison area	This work	Hwang et al. (1998)	Improvement
(1) Alaska Abyssal	4.887	5.168	0.281
(2) East Pacific Rise	3.057	6.786	3.729
(3) Caribbean Sea	9.840	11.399	1.559
(4) Reykjanes Ridge	5.122	5.202	0.080
(5) Sierra Leone Basin	3.678	3.688	0.010
(6) Mediterranean Sea	13.026	13.480	0.454
(7) Carlsberg Ridge	7.347	7.397	0.023
(8) Kerguelen Plateau	6.017	6.931	0.914
(9) South China Sea	8.004	8.229	0.225
(10) Mariana Trench	11.561	11.814	0.253
(11) Fiji Plateau	13.365	14.148	0.783
(12) Ross Sea	7.634	8.477	0.843
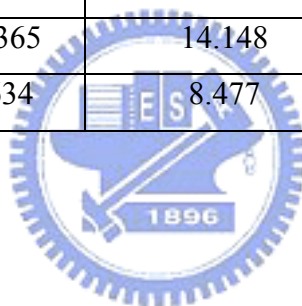
CHAPTER 4

SHALLOW-WATER ALTIMETRY GRAVITY RECOVERY: DATA PROCESSING AND COMPARISON OF METHODS

4.1   Introduction

Satellite altimetry can be useful in coastal area, such as coastal geoid modeling and offshore geophysical explorations, see, e.g., Hwang (1997), Andersen and Knudsen (2000). Recent global altimeter-derived gravity anomaly grids by, e.g., Sandwell and Smith (1997), Andersen et al. (2001), and Hwang et al. (2002), confirm that the accuracies of estimated gravity anomalies range from 3 to 14 mgals, depending on gravity roughness, data quality and areas of comparison. These papers made their comparisons with shipborne gravity anomalies mostly in the open oceans. Research has shown that over shallow waters, altimeter data are prone to measurement errors and errors in geophysical corrections. For example, Deng et al. (2002) shows that within about 10 km to the coastlines, altimeter waveforms are not what the onboard tracker has expected and use of ocean mode product altimetry leads to error in range measurement. The footprint of a radiometer is also large enough to make the water vapor contents measurement near shores highly inaccurate, yielding bad wet tropospheric corrections. Large tide model errors and large wave heights, among others, add to the problem of poor quality in altimeter data over shallow waters. Worst still, there is no data on land for near-shore gravity computation and this poses a theoretical problem in transformation of functionals of the earth's gravity field

(for example, transforming gravity anomaly to geoid requires global integration). Thus, gravity anomaly prediction over shallow waters has been a challenging task, due mainly to problems with both data and theory. In view of these problems, this chapter compares two methods of gravity computation from altimetry discussed in (2.3.1) and (2.3.2), and a method of removing outliers in altimeter data based on a nonlinear filter is also discussed. The test area is over shallow waters in Taiwan Strait and East China sea. Figure 4.1 shows the bathymetry based on the ETOPO5 depth grid. The water west of Taiwan is a part of the east Asia continental shelf with depths less than 200 meters, while the waters east of Taiwan is deep due to the subducting Philippine Sea Plate.

4.2   Data Processing：Outlier Detection and Filtering

Outliers which are anomalous measurements in data will create a damaging result. There are methods abundant in literature for removing outliers in one-dimensional time series, see, e.g., Kaiser (1999), Gomez et al. (1999) and Pearson (2002). In this chapter we use an iterative method to remove outliers in along-track altimeter data. Consider the measured height or the differenced height as a time series with along-track distance as the independent variable. First, a filtered time series is obtained by convolving the original time series with the Gaussian function

$$f(x) = e^{-\frac{x^2}{\sigma^2}} \tag{4.1}$$

where σ is the 1/6 of the given window size of convolution. The definition of Gaussian function is the same as that used in GMT (Wessel and Smith, 1995). For all data points the differences between the raw and filtered values are computed, and the
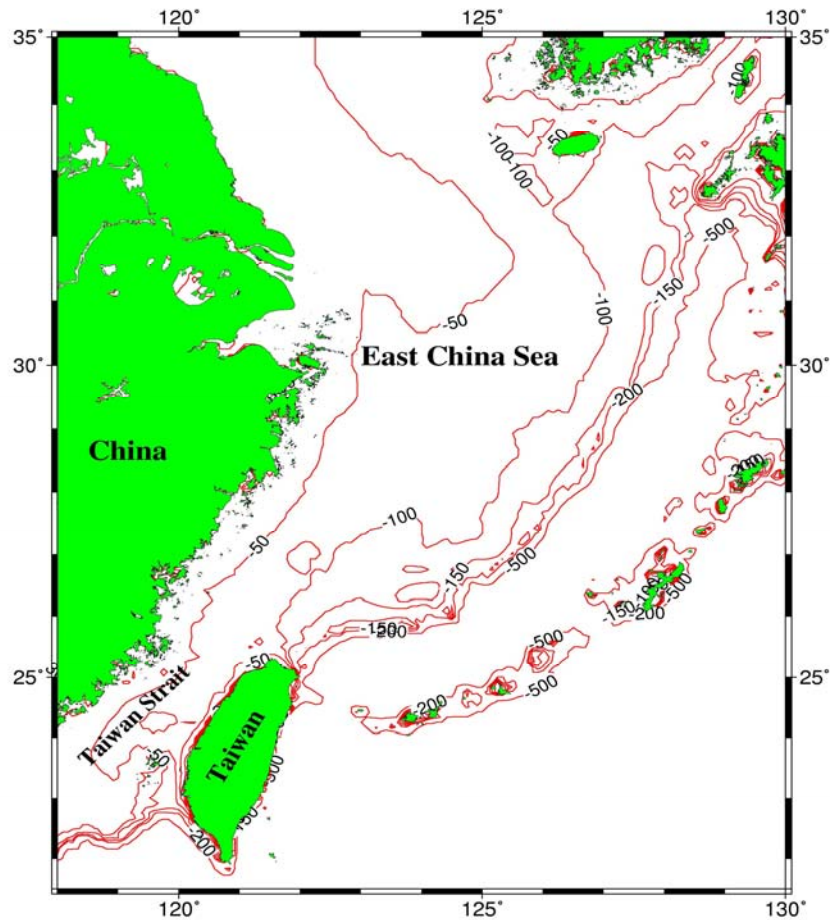
Figure 4.1: Contours of slected depths around Taiwan, unit is meter

standard deviation of the differences is found. The largest difference that also exceeds

three times of the standard deviation is considered an outlier and the corresponding

data value is removed from the time series. The cleaned time series is filtered again

and the new differences are examined against the new standard deviation to remove a

possible outlier. This process stops when no outlier is found.

We choose pass d64 of Geosat/ERM, which travels across Taiwan, to be used for

the test of outliers detection. Figure 4.2 shows the ground track of pass d64 and

Figure 4.3 shows the result of outlier removing. In Figure 4.3, we clearly see that

erroneous differenced heights are successfully removed (discrete points) after outlier

detection with a 28-km window. For the non-repeat satellite mission such as Seasat,

ERS-1/gm and Geosat/gm, we do outlier detection as well as filtering for the differenced heights with a 14-km wavelength in order to reduce the data noise. There is no need of filtering for the differenced heights from the repeat missions because their data noises will be reduced due to time averaging. As an example, we choose pass a27 of Geosat/GM for testing outlier removal and filtering. Figure 4.4 shows the ground pass a27 and Figure 4.5 shows the result. Again, our algorithm removes outliers and filter the data successfully.

Furthermore, Figure 4.6 and 4.7 show the result of outlier detection along Tracks d0222 and a3083 of Geosat/GM. Both tracks pass through Peng-Hu Island in the Taiwan Strait, where most of the outliers occur and the differenced heights contain large variation. These examples from the Geosat altimeter show that differenced height is very sensitive to sudden change of height, and is particularly useful for outlier detection in the above iterative method.

We also tested this outlier detection method using altimeter data from the repeat and non-repeat missions in the East China Sea area. The altimeter data type used is also differenced height. It turns out outliers in differenced heights are very sensitive to this method, especially when along-track SSHs experience an abrupt change. A spike of SSH will translate into two large height differences. As an example, Figure 4.9 shows the result of outlier detection along two tracks of Geosat/ERM. In this case, the outliers are removed using a 28-km window size to generate the filtered time series. Another test was carried out using data from a non-repeat mission--Geosat/GM. Figure 4.11 shows the result of the test along two tracks of Geosat/GM. In this case, we used an 18-km window size. According to our experiments, different window sizes

for outlier detection should be used for altimeter data from different missions. Based on numerous tests, in this chapter we adopt 28 km as the optimal window sizes for the repeat missions, and 18km and 14km for non-repeat missions, respectively, over the ECS and the TS.
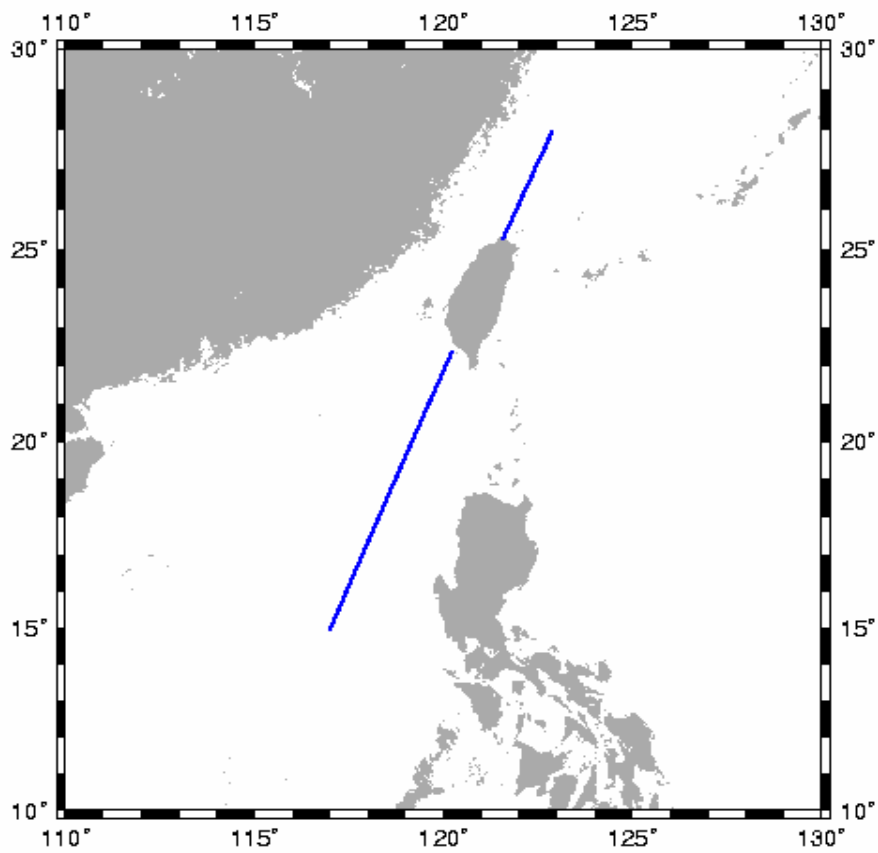

Figure 4.2: The ground track of pass d64 of Geosat/ERM
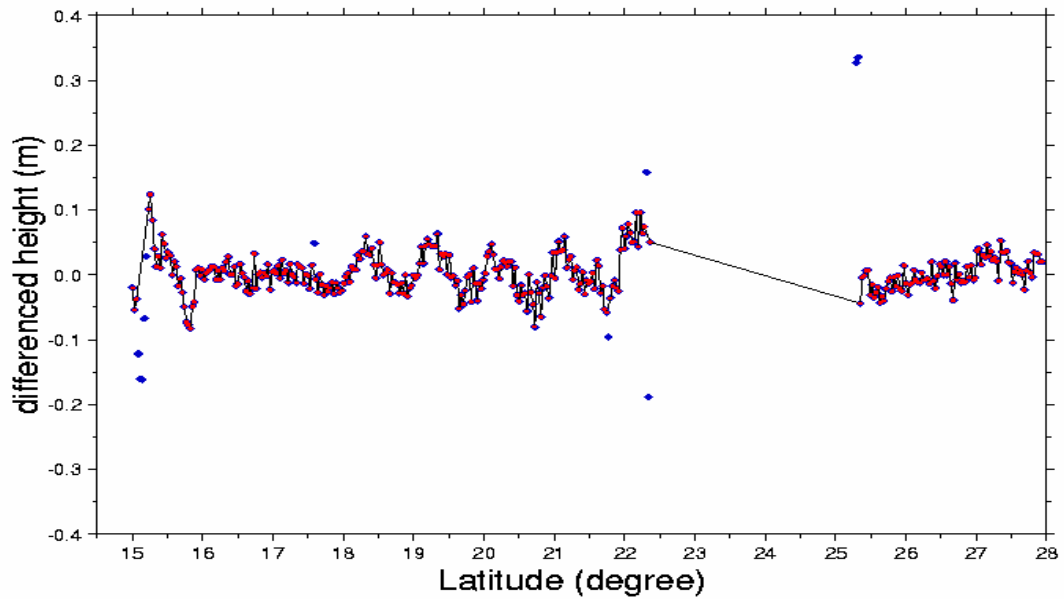
Figure 4.3: Raw data points (red) and outliers (blue) detected with a 28-km window for pass d64 of Geosat/ERM.
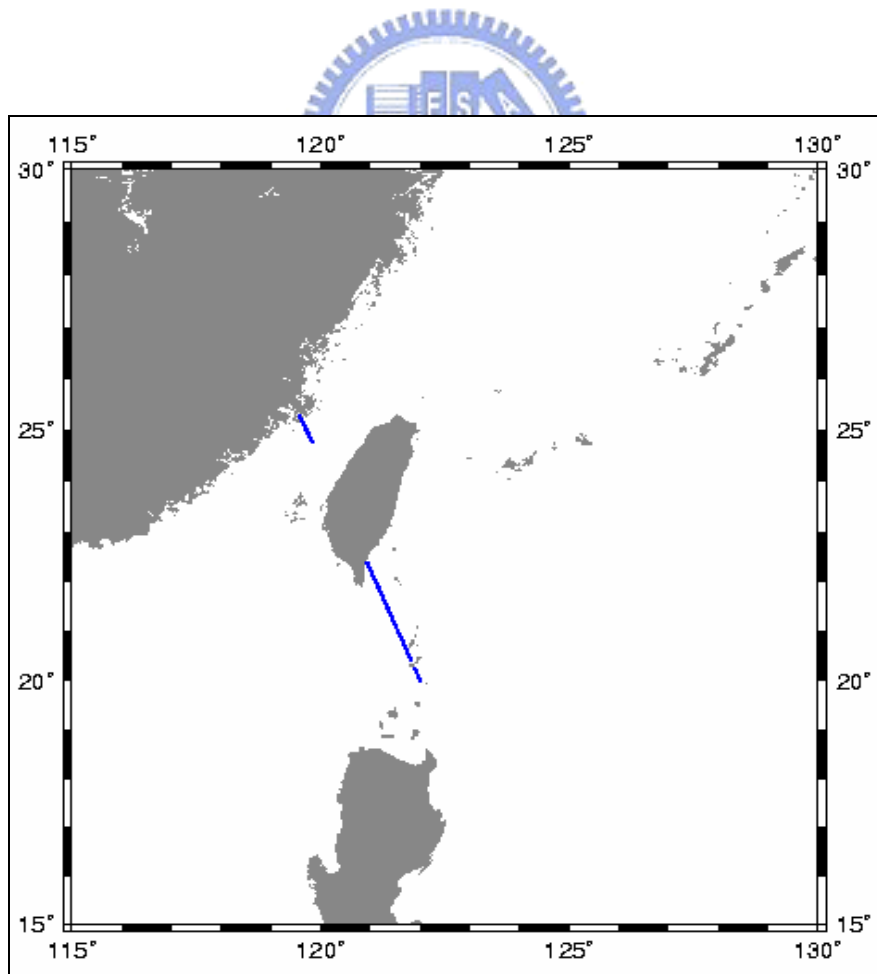
Figure 4.4: The ground track of pass a27 of Geosat/GM
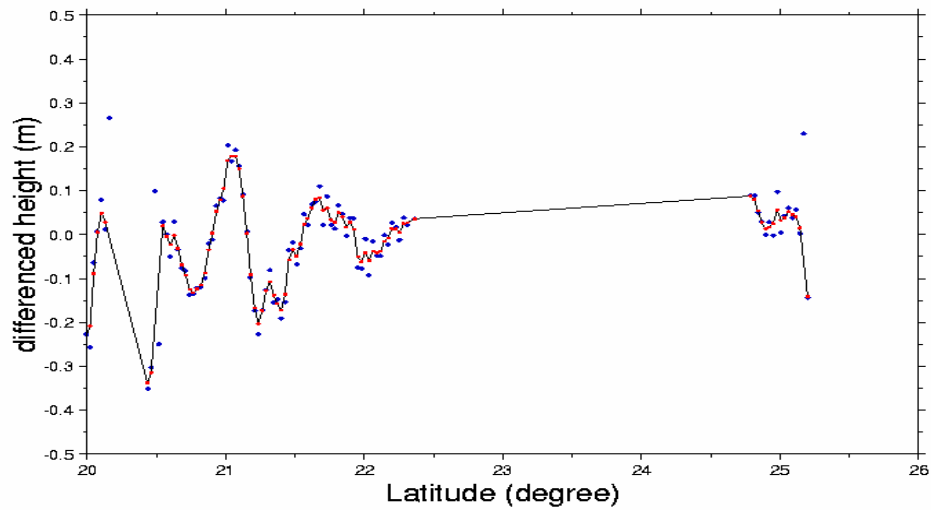
Figure 4.5: Raw data points (blue) and filtered and outlier-free points (red) using a 14-km window for pass a27 of Geosat/gm.
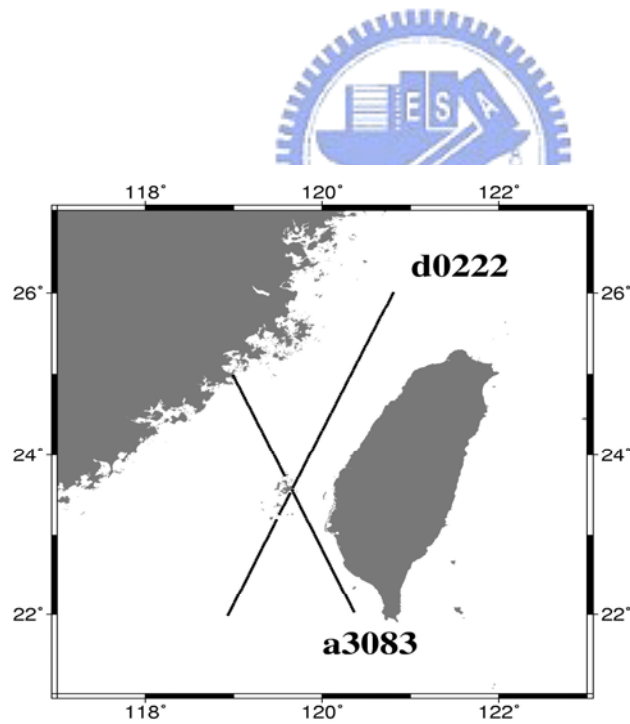
Figure 4.6: The ground tracks of Geosat/GM d0222 and a3083
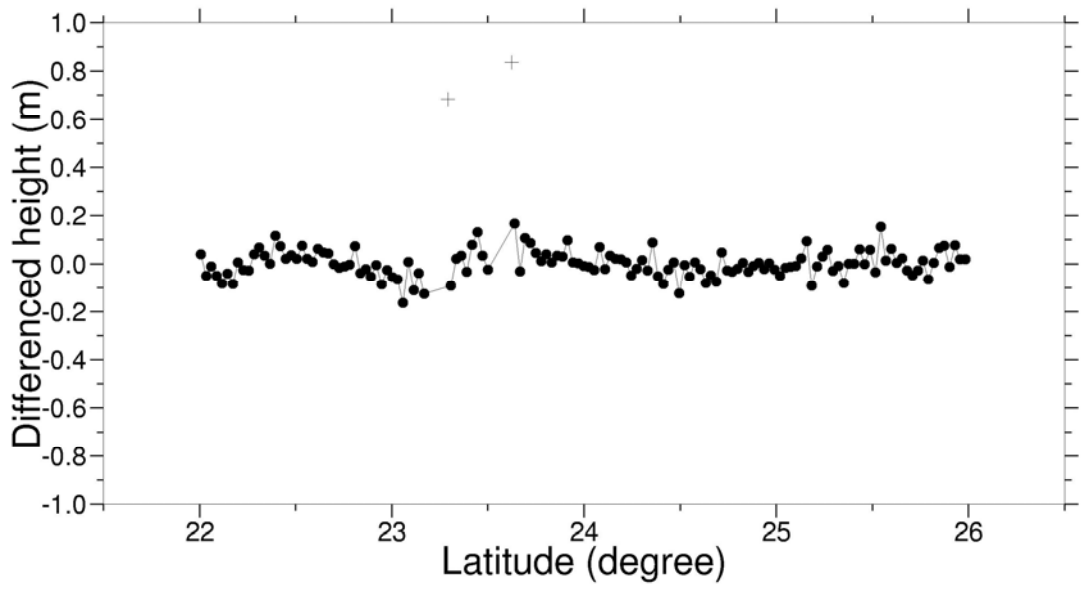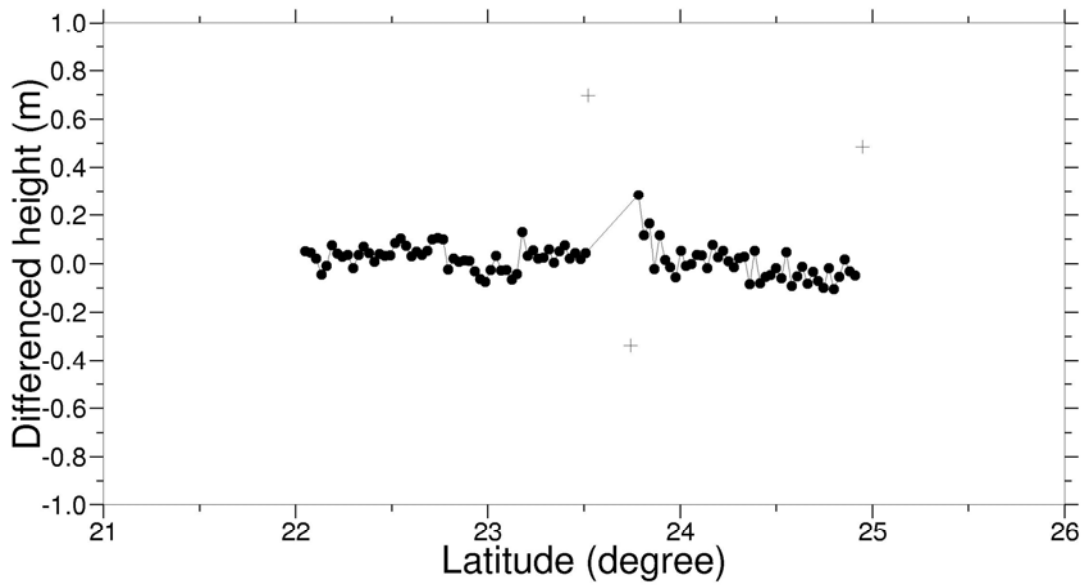
Figure 4.7: Differenced heights for passes a3083 and d0222 of Geosat/gm, crosses represent outliers.
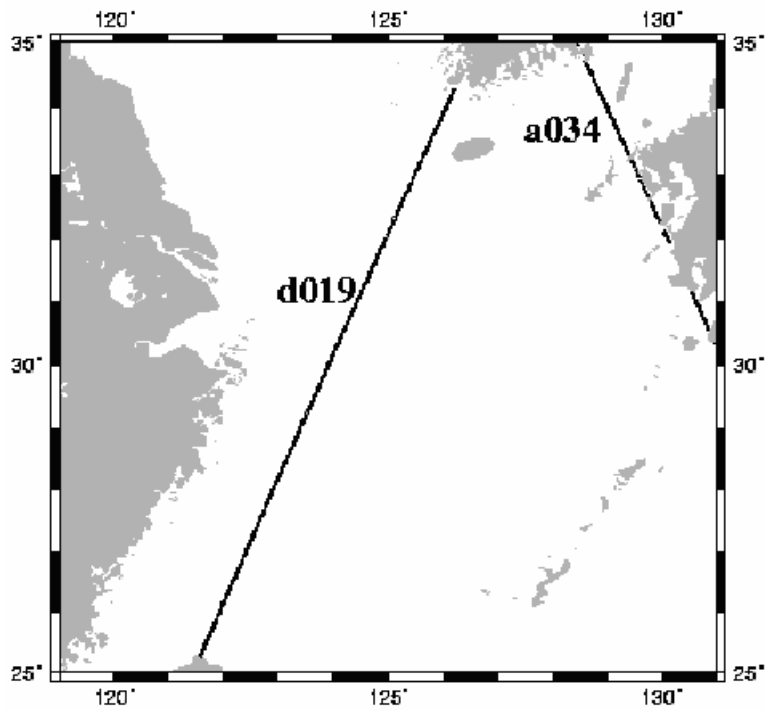
Figure 4.8: Ascending and descending passes of Geosat/ERM for outlier detection.
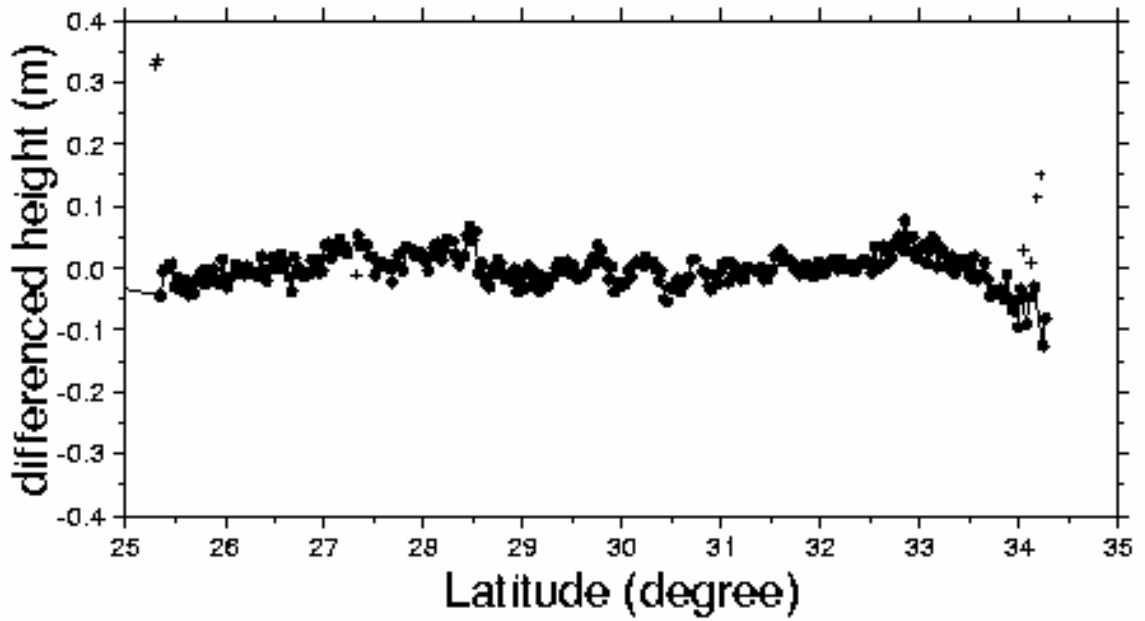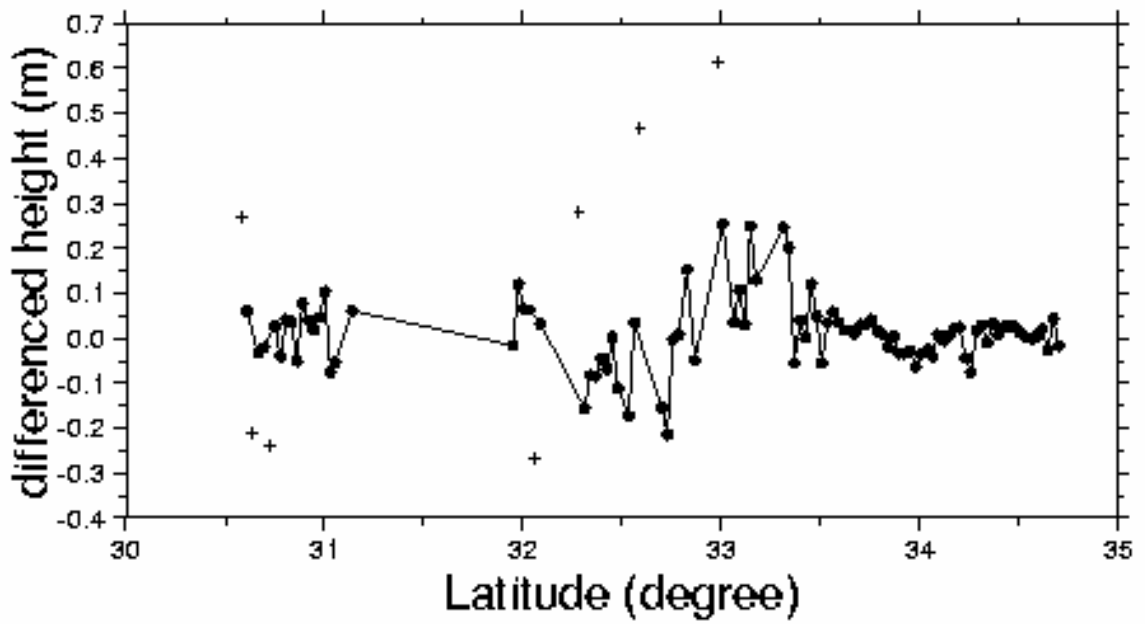
Figure 4.9: Results with a 28-km window size. Outliers are not connected by the lines.
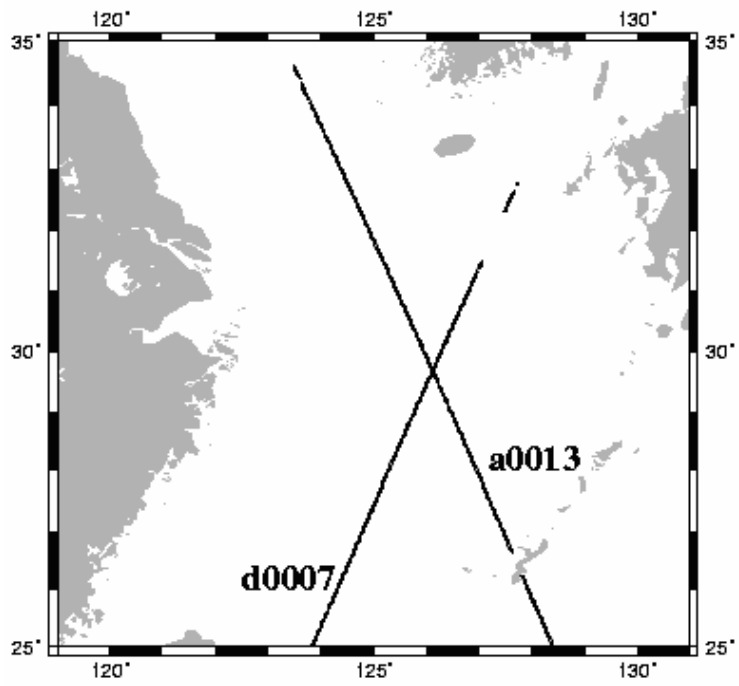
Figure 4.10: Ascending and descending passes of Geosat/GM for outlier detection.

a0013
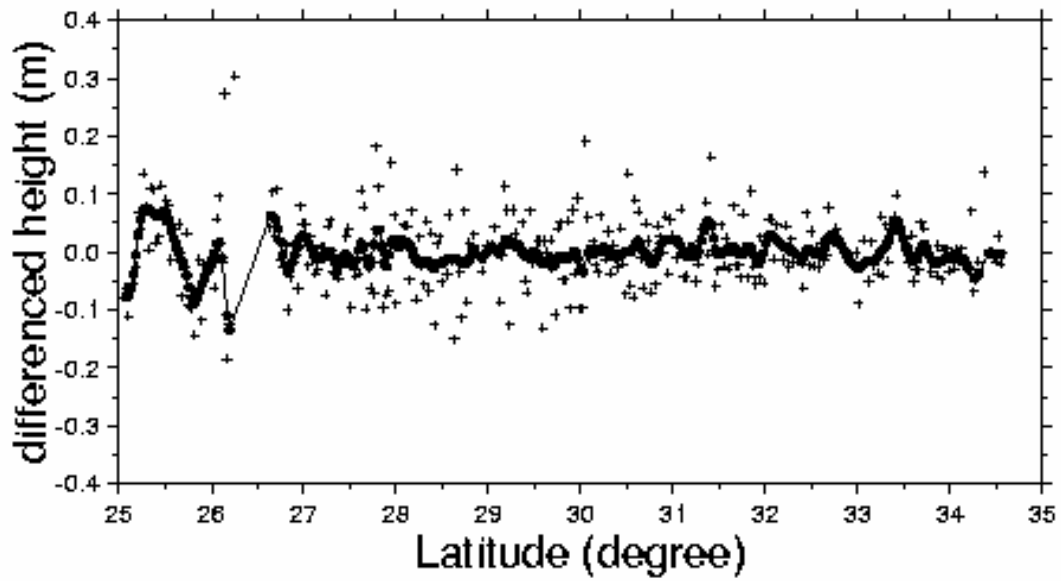
d0007
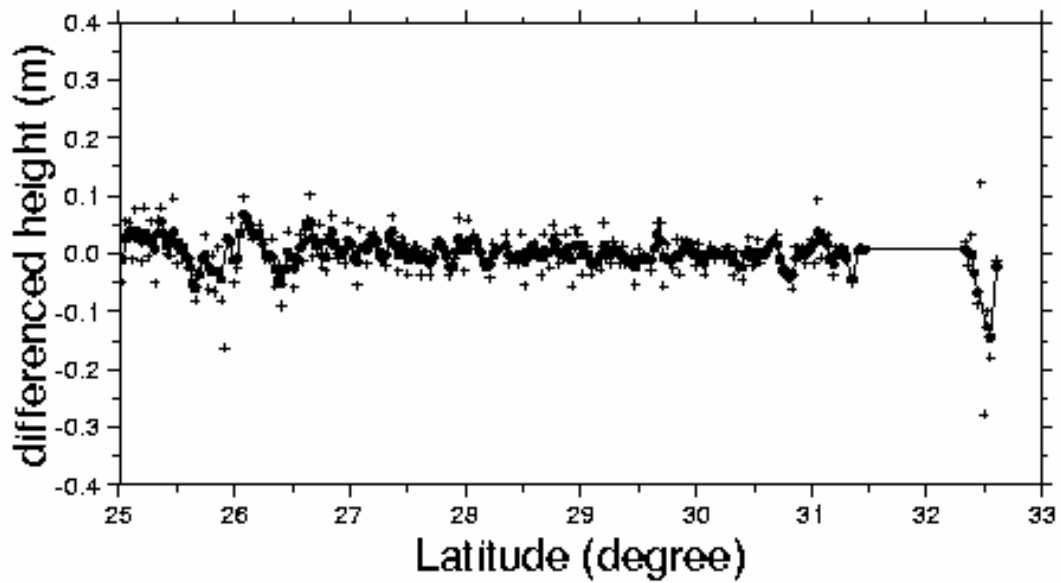
Figure 4.11: Results with a 18-km window size. Outliers are not connected by the lines.

4.3 Results of Tests

We use multi-satellite altimeter data mentioned in chapter 2 for testing two methods (by using three kinds of altimeter data types). These data have different noise levels, which work as weights in LSC computations. In all computations, the standard remove-restore procedure is employed. In this procedure, the long wavelength part of altimeter-derived data (differenced height, height slope or DOV) implied by the EMG96 geopotential model (Lemoine et al. 1998) to degree 360 is removed. With the residual data, the residual gravity anomaly is computed and finally the gravity anomaly implied by the EMG96 model is restored. The needed isotropic covariance functions are computed using the error covariance of EGM96 and the Tscherning/Rapp Model 4 signal covariance (Tscherning and Rapp, 1974). All needed covariance functions are tabulated at an interval at of 0.01°. The local covariance values in a prediction window are scaled by the ratio between the data variance and the global variance.

For the gravity grids from methods 1 and 2, a further filtering be 2 2-D median filter improved the result. Table 4.1 and 4.2 shows the results of such filtering. Based on the testing result for method 2 in Table 4.1 and for method 1 in Table 4.2, we decide to use 16 km as the filter parameters in Taiwan Strait and to use 20 km as the filter parameters in East China Sea.

To evaluate the accuracy of the gravity anomalies derived from three different methods mentioned, we made comparisons between the predicted and shipborne anomalies in the Taiwan Strait and the East China Sea area. The shipborne gravity anomaly data in Taiwan are from Hsu et al. (1998) and that in the East China Sea are from a global data base at Oxford (Hwang and Parsons, 1995) and a pointwise

Table 4.1: RMS differences (in mgals) between predicted and shipborne gravity anomalies using different filter parameters over the Taiwan Strait.

Filter parameter	RMS
No filter	11.2687
Filter wavelength = 8 km	10.8739
Filter wavelength = 16 km	10.4353
Filter wavelength = 24 km	10.5682

Table 4.2: RMS differences (in mgals) between predicted and shipborne gravity anomalies using different filter parameters over the East China Sea.

Filter parameter	RMS
No filter	10.80
Filter wavelength = 10 km	10.01
Filter wavelength = 16 km	9.82
Filter wavelength = 18 km	9.76
Filter wavelength = 20 km	9.59
Filter wavelength = 22 km	9.61
Filter wavelength = 24 km	9.64

comparison was made for both of them. The ship tracks are shown in Figure 4.12 and Figure 4.13. Table 4.3 and Table 4.4 show the result of the comparisons in TS and in ECS. The conclusions we get from the two tables are similar and the only difference is that the inverse Vening Meinesz method with DOV produces the worst result in Table 4.3   The gravity grid from method 1 has a better accuracy than those from the other two methods in the two area. The least square collocation with slope height gives results which are very close to but a little bit worse than use of differenced height as data type in method 1. By using of least square collocation with differenced height, the RMS differences between the predicted and shipborne gravity anomalies lower 1.67 mgal and 2.27 mgal comparing to method 3 (Hwang et al., 2002) in TS and ECS respectively.
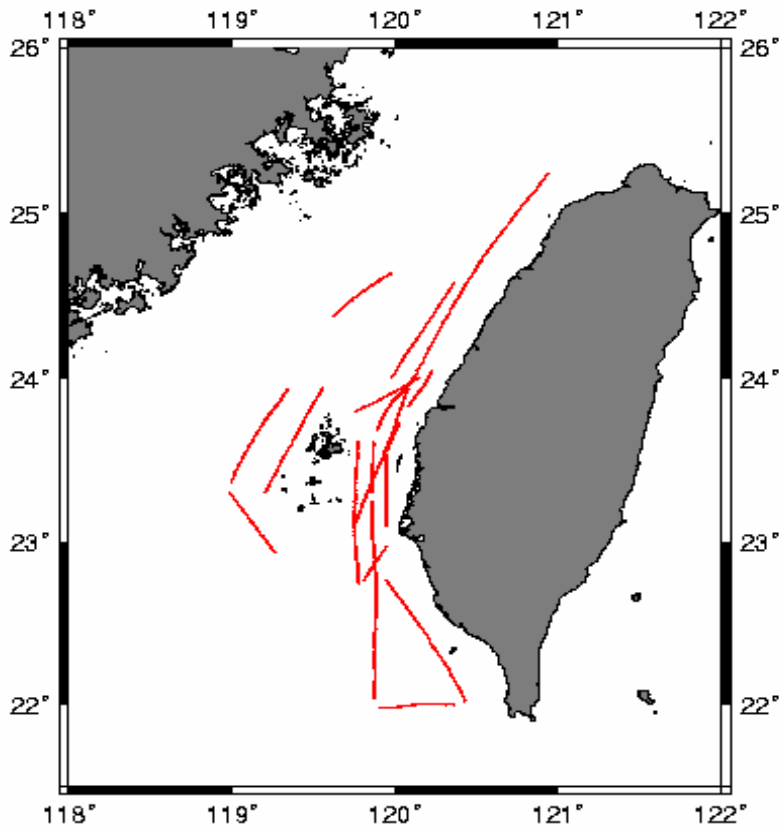
Figure 4.12: Distribution of shipborne gravity data in Taiwan Strait area.
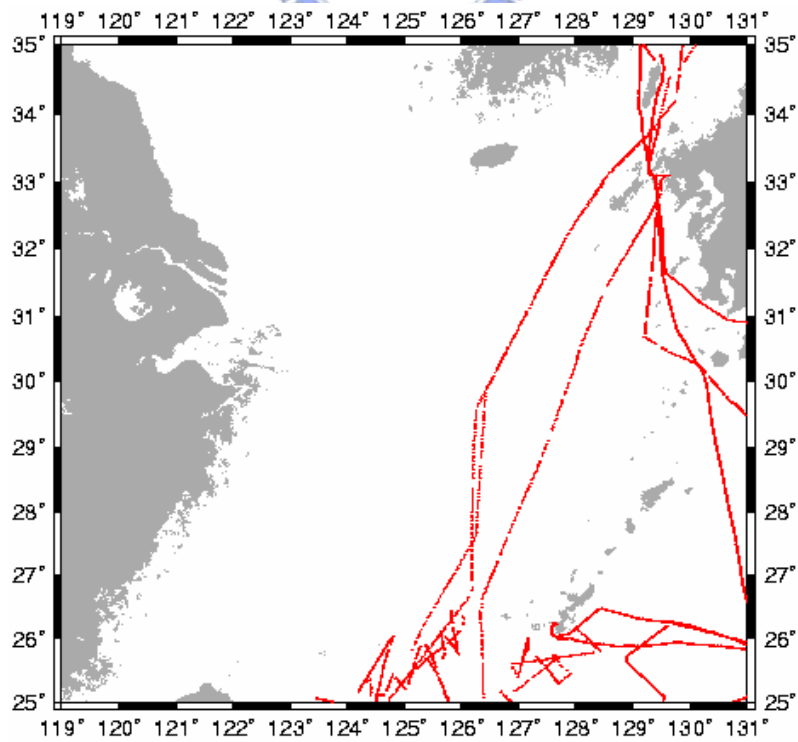
Figure 4.13: Distribution of shipborne gravity data in the East China Sea.

Table 4.3: Statistics of differences (in mgals) between altimeter-derived and shipborne gravity anomalies

Method (data type)	RMS
(1) LSC (differenced height)	9.06
(1) LSC (height slope)	10.26
(1) LSC (DOV)	10.44
(2) inverse Vening Meinesz (DOV)	10.73

Table 4.4: Statistics of differences (in mgals) between altimeter-derived and shipborne gravity anomalies in the East China Sea.

Method (data type)	RMS
(1) LSC (differenced height)	9.59
(1) LSC (height slope)	9.77
(1) LSC (DOV)	13.10
(2) inverse Vening Meinesz (DOV)	11.86
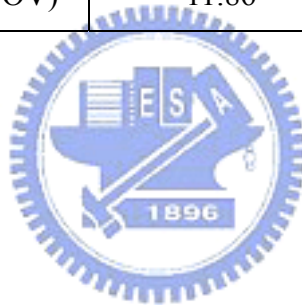
CHAPTER 5

GRAVITY ANOMALY OVER EAST CHINA SEA AND TAIWAN STRAIT: CASE STUDY AND ANALYSIS

5.1 Introduction

Over shallow waters Satellite altimetry has been very useful in earth sciences, see, e.g., Fu and Cazenave (2001) and Hwang et al. (2004a). One example of geodetic application is coastal gravity field modeling: both coastal altimetry data and terrestrial gravity anomalies were got together to determine gravity field model that are far better than the existing models that only used terrestrial gravity data (Li and Sideris, 1997; Andersen and Knudsen, 2000). Furthermore, the potential of satellite altimetry to help to learn about sea surface topography have been tested in Hipkin (2000). Sea surface topography is the essential parameter for a world vertical datum (Rapp and Balasubramania, 1992). For oceanographic applications, shallow-water altimetry has been used to derive M-2 internal tides (Niwa and Hibiya, 2004) and variations of surface circulations (Yanagi et al., 1997). There are other examples of geophysical applications of altimetry in the literature; we refer to Cazenave and Royer (2001) for a review.

Altimeter-gravity conversion is one of the most important parts in the geodetic and geophysical applications of satellite altimetry. Currently, the achieved accuracies of altimeter-derived gravity anomalies vary from one oceanic region to another,

depending on gravity roughness, altimeter data quality and density (Sandwell and Smith, 1997; Hwang et al., 2002; and Andersen et al., 2005). Accuracy analyses associated with global gravity anomaly grids were mostly made over the open oceans. However, altimeter data quality over shallow waters can be seriously degraded because of (1) bad tidal correction, (2) bad wet tropospheric correction because of corruption in radiometer measurements, (3) large sea surface variability and (4) contaminated altimeter waveforms (Deng et al., 2003). Inferior or erroneous altimeter data will lead to gravity anomalies containing artifacts and in turn false interpretations of the underlying geophysical phenomena.

The East China Sea and the Taiwan Strait are two typical shallow-water areas which are defined as waters with a depth less than 500 meters. In these areas the gravity fields are relatively smooth, but large gravity variations occur over regions with thick sediments, structural highs and at the margin of the continental shelf. Figure 5.1 shows the bathymetry in the ECS and the TS.

Over the ECS, one publicly accessible database of shipborne gravity data can be found at the National Geophysical Data Center (NGDC) (http://www.ngdc.noaa.gov), and the data are sparsely distributed. In the TS, the shipborne gravity data were mostly collected by research ships studying marine geophysics around Taiwan. Global altimeter-derived gravity anomaly grids have been important sources of gravity anomalies in these areas.

The purposes of this chapter is to (1) compare global gravity models and tide models over ECS and TS to analyze the errors in altimeter-gravity conversion over shallow waters, and to detect outliers. (2) perform case studies and analysis using shipborne gravity data over the ECS and the TS. (3) to demonstrate how we can

improve the accuracy of altimeter-derived gravity anomaly by using land data.
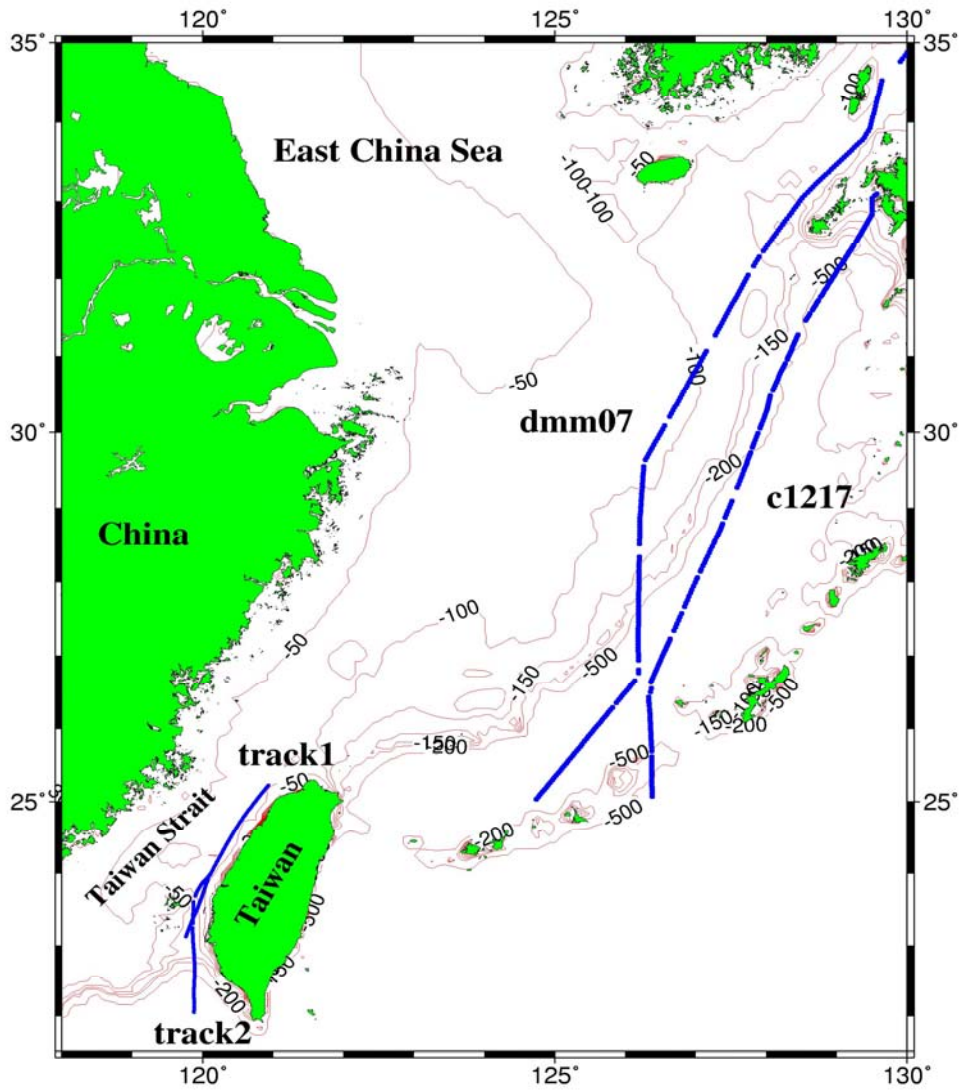
Figure 5.1: Bathymetry (dashed lines) in the East China Sea and Taiwan Strait. Lines represent shipborne gravity data for comparison with altimeter-derived gravity anomalies.

5.2 Comparison of Two Global Gravity Anomaly Grids over ECS and TS

To show the problems of the altimeter-gravity conversion over shallow waters, we compare two global, altimeter-derived gravity anomaly grids over the ECS and the TS. The two grids were computed by Sandwell and Smith (1997), Andersen et al. (2005), which are designated as SS02 and KMS02, respectively. The differences over areas of various depths are summarized in Table 5.1. Table 5.1 shows no clear correlation between depth and gravity anomaly difference at depths less than 500 meters, but in general the differences at depths greater than 500 meters are smaller than other areas. Since some of the systematic errors may be eliminated when differencing any two grids, the true errors in the gravity anomaly grids may be actually larger than what have been shown in Table 5.1. Figure 5.2 shows the distribution of the differences. As expected, large differences occur over the waters off the coasts of China, Japan, Korea, and the Ryukyu Island Arc. Note that large differences exist over almost the entire TS. Furthermore, the areas distant from the coasts also contain large differences, e.g., a spot off the east coast of China centering at about latitude= 28°N and longitude = 124°E.

Table 5.1: Statistics of the differences between the SS02 and KMS02 global gravity anomaly grids over the area $118° - 130°\text{E}, 22° - 35°\text{N}$

Depth (m)	0-100	100-200	200-500	> 500
Mean (mgal)	0.27	0.05	0.56	0.12
RMS (mgal)	4.96	4.06	5.65	4.21
No. of points	50491	14964	7426	39450
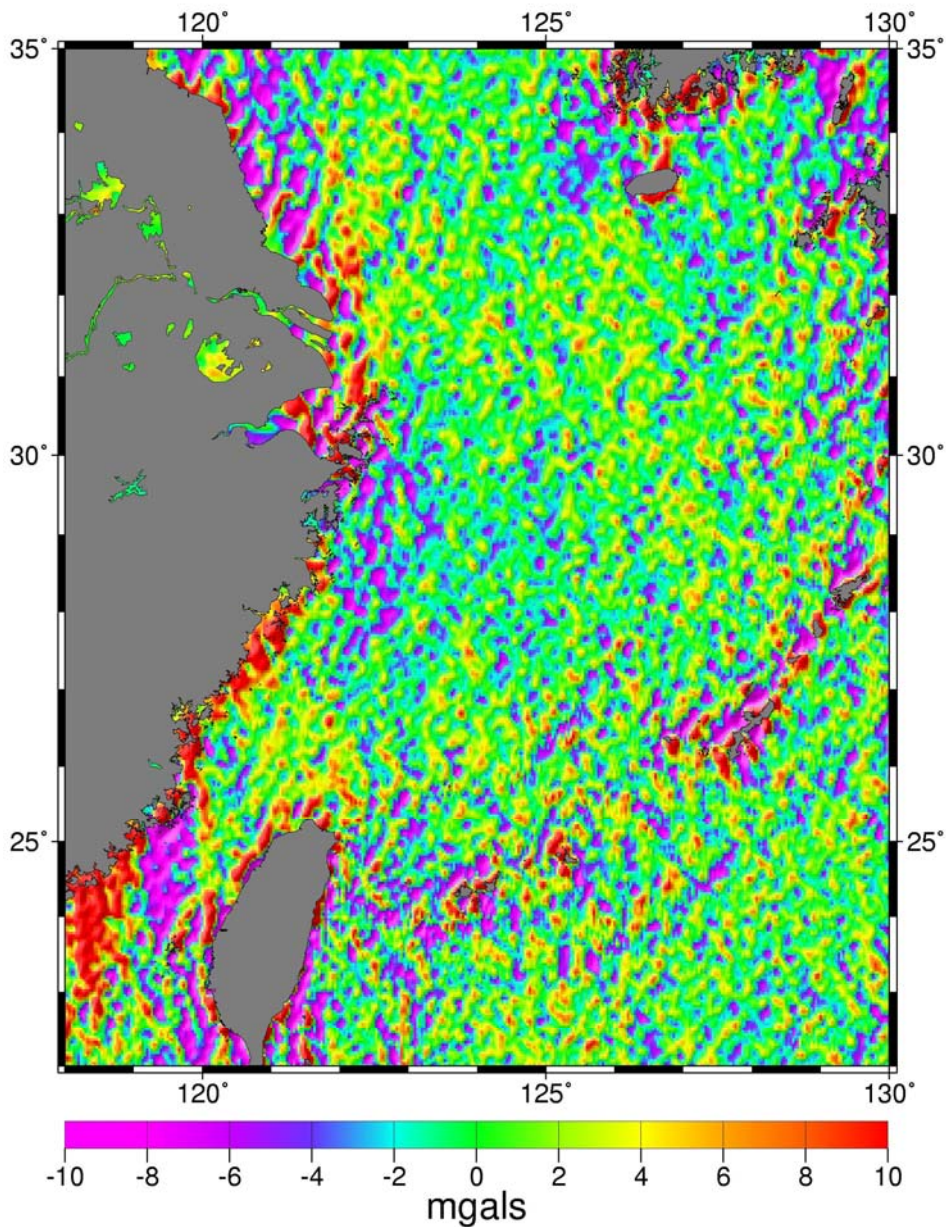
Figure 5.2: Differences between the SS02 and KMS02 global gravity anomaly grids.

In order to see the possible causes of the differences, we investigate the qualities of SSHs and two selected tide models here. Figure 5.3 shows the standard deviations of mean SSHs from the Geosat/ERM, ERS-1/35day and ERS-2/35day repeat missions. Here a standard deviation of SSH is the result of SSH measurement error and SSH variability. The standard deviations of Geosat/ERM SSHs are relatively small because a large number of repeat cycles (68 cycles) were used, compared to only 26 cycles

used in averaging ERS-1 and ERS-2 repeat SSHs. The pattern of ERS-1 standard deviations resembles that of ERS-2 standard deviations. In general, standard deviation of SSH increases with decreasing depth. As seen in Figures 5.2 and 5.3, gravity anomaly difference is highly correlated with standard deviation of SSH. In general, gravity anomaly difference (absolute value) increases with standard deviation of SSH.
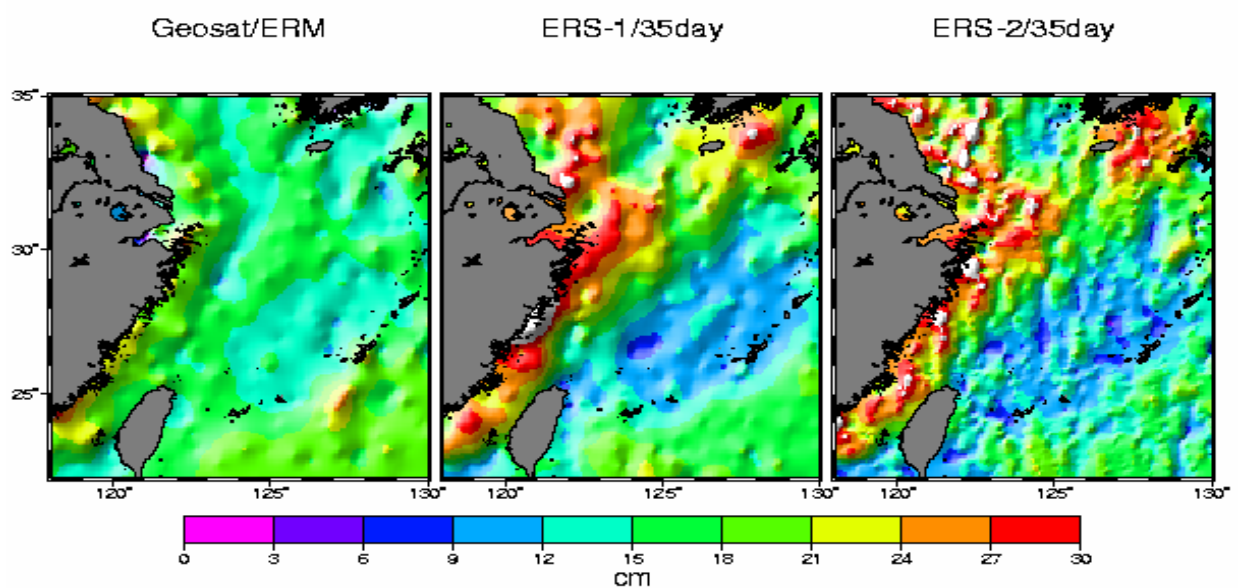
Figure 5.3: Standard deviations of sea surface heights from the Geosat/ERM, ERS-1/35 day and ERS-2/35 day repeat missions.

Figure 5.4 shows the tidal height differences at a selected epoch from the NAO tide model (Mastsumoto et al., 2000) and the CSR4.0 tide model (Eanes, 1999). Again, large tidal height differences occur in the same places where large standard deviations of SSHs (Figure 5.3) and large gravity anomaly differences (Figure 5.2) occur, showing these three quantities are geographically correlated. Figure 5.5 shows the normalized values of depths, standard deviations of ERS-1 SSHs, tidal height differences (CSR4.0 vs. NAO 99) along Tracks 1 and 2 (Figure 5.1). A normalized value, y, is obtained by

$$y = \frac{x - \bar{x}}{\sigma_x}$$

<div align="right">(5.1)</div>

where x is the raw value, $\bar{x}$ is the mean value, σ_x is the standard deviation of the time series. As seen in Figure 5.5, the standard deviation of ERS-1 SSH and the tidal height difference along Tracks 1 and 2 have a correlation coefficient of 0.9, and both increase with decreasing depth. The NAO and CSR4.0 tide models are derived from the TOPEX/Poseidon (T/P) altimeter data. Over areas with bad T/P SSHs, mostly caused by bad range measurements and bad geophysical corrections, both of these tide models will produce inaccurate tidal heights. Also, by neglecting shallow-water tidal areas in the tide models creates additional errors. Those areas with large differences in Figure 5.4 are just where NAO and CSR4.0 produce inaccurate tidal heights. By using of these inaccurate tidal heights to correct for the tidal effects in altimeter data will inevitably lead to have poorer quality of SSHs, and creates large standard deviations seen in Figure 5.3.
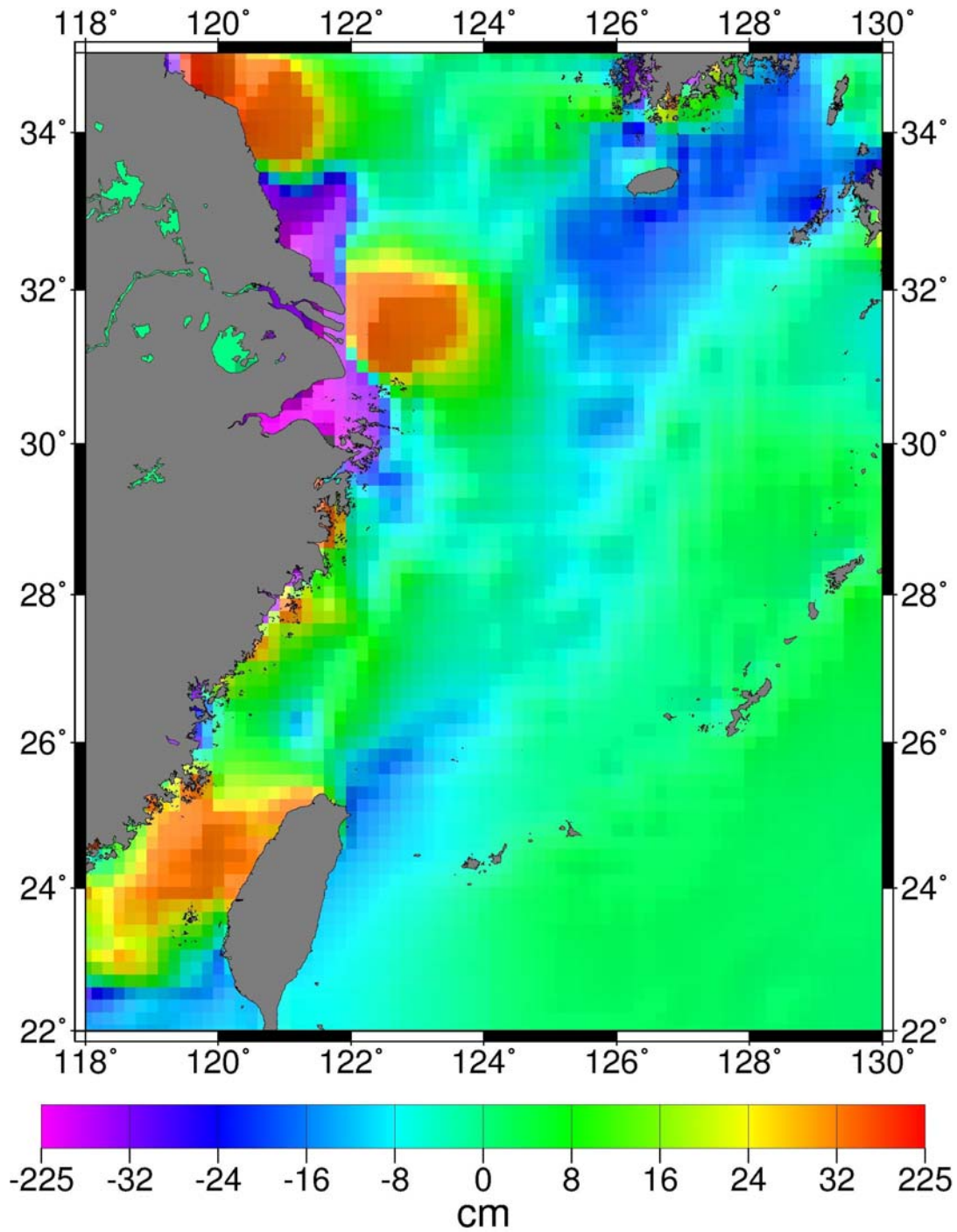
Figure 5.4: Differences between the NAO and CSR4.0 tidal heights at a selected epoch.
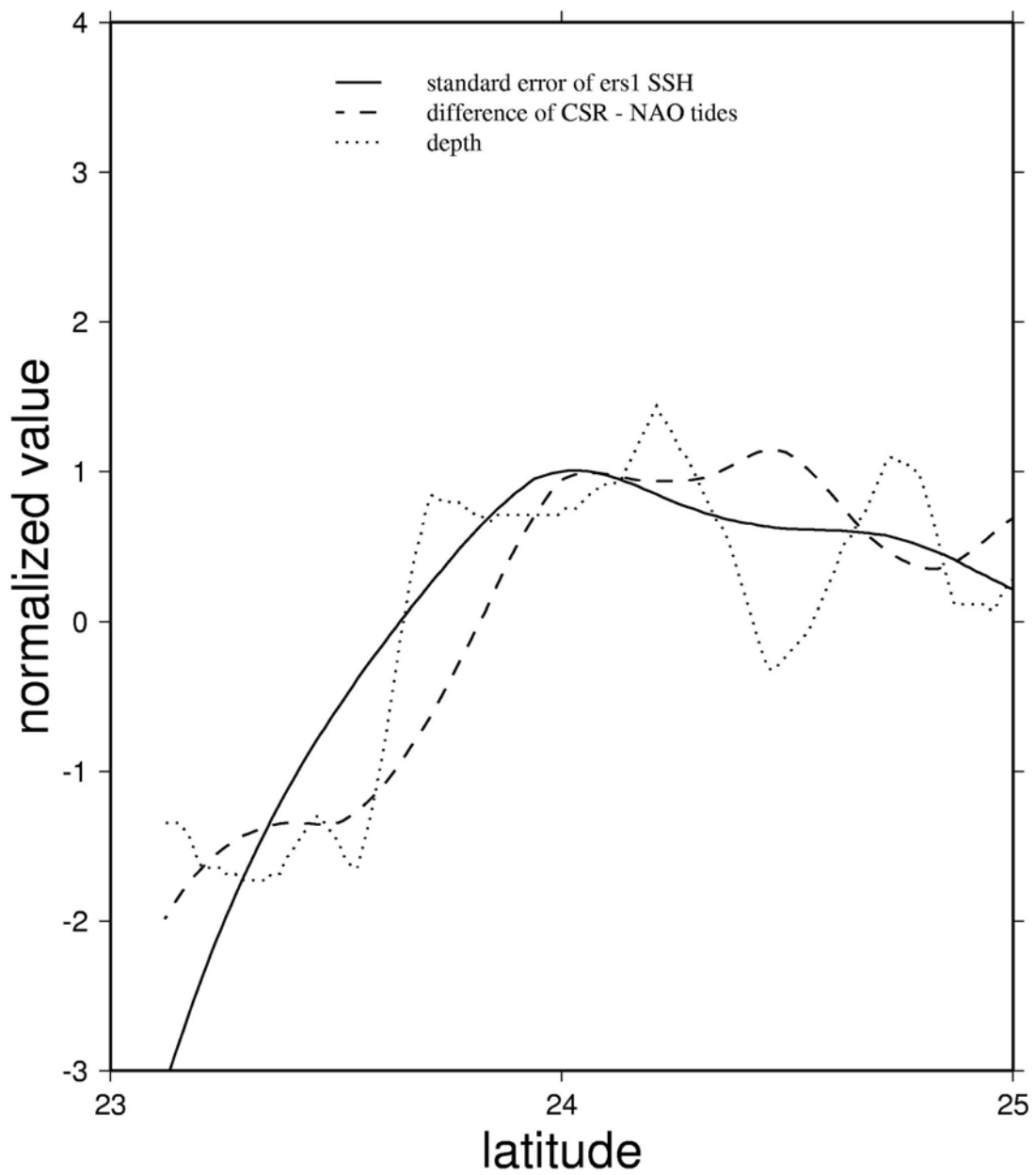
Figure 5.5a: Time series of normalized standard deviation of ERS-1 SSH, tide height difference and depth, along Track 1.
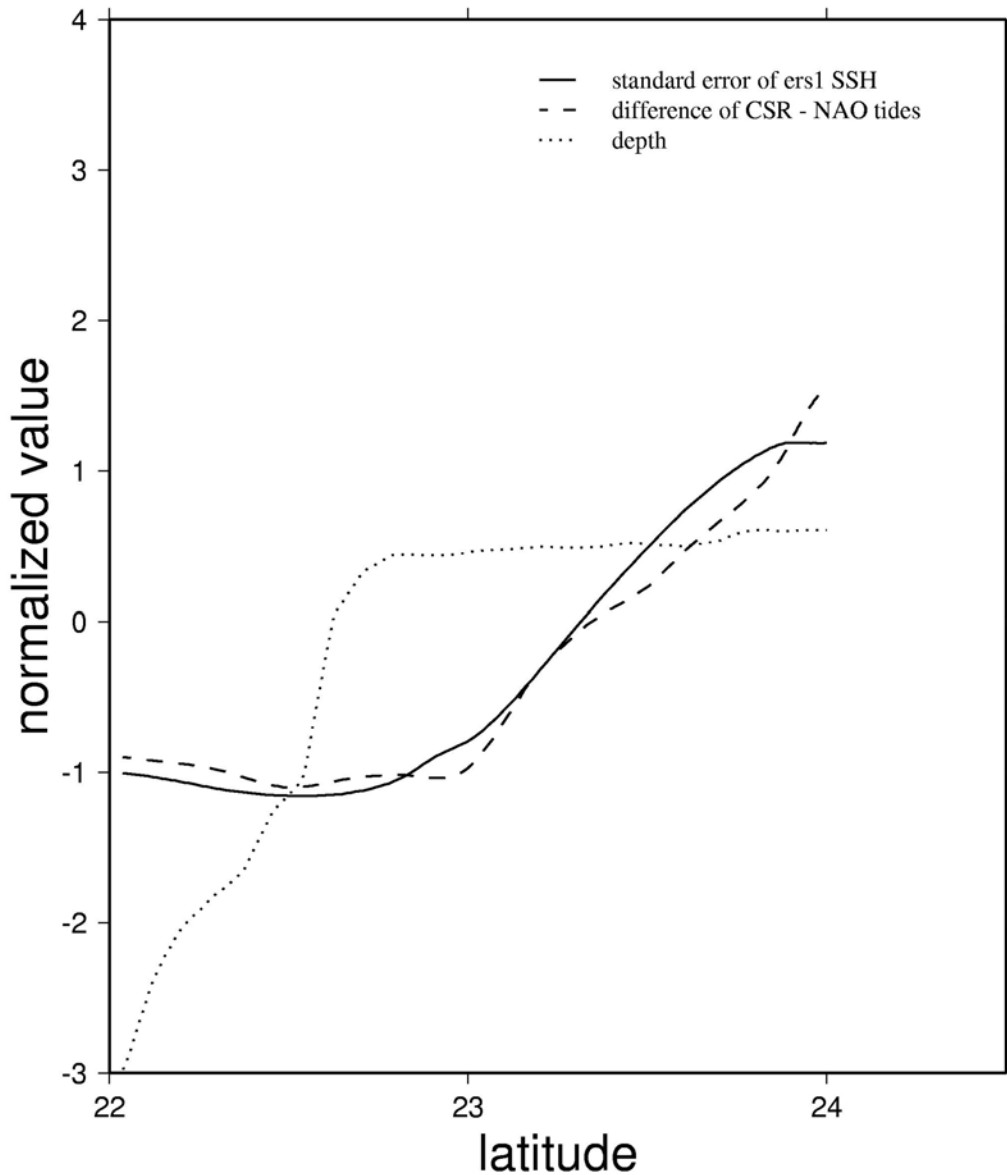
Figure 5.5b: Time series of normalized standard deviation of ERS-1 SSH, tide height difference and depth, along Track 2.

According to Jan et al. (2004) and Lefevre et al. (2000), ocean tides over ECS and TS are complex with high-frequency spatial variations in tidal amplitude and phase. The strong, fast-changing tidal currents over TS also increase the roughness of the sea surface and in turn increase the noise level of altimeter ranging (Sandwell and Smith, 2001). This explains why the tide model error over TS is large throughout the entire area (Figure 5.4). In addition, the monsoonal winds in winter and summer

induce large waves over ECS and TS (Jacobs et al., 2000; Wang, 2004), resulting in a large sea surface variability lasting more than half of a year. Therefore, one would expect that the noise level of altimeter measurements in these two areas is higher than that over a calm sea. In conclusion, inferior altimeter range measurements and inferior geophysical corrections combine to produce inferior SSHs, which in turn result in degraded gravity anomalies. More discussions on the limitations of gravity recovery from altimetry can be found in Sandwell and Smith (2001).

5.3 Coastal Land and Sea Data for Accuracy Enhancement

Altimeter-gravity conversion at the land-sea boundary is an extrapolation process since land altimeter data cannot be used for gravity derivation. At the immediate waters off the coast, there could be no reliable altimeter data due to waveform contamination (Deng et al., 2003). Also, because of depth limitation a large research ship cannot approach closely the coasts, so there are always void zones of shipborne gravity. This deficiency can be improved by using data near the coasts, including gravity anomalies from relative and airborne gravity surveys (Torge, 1989), DOVs from astro-geodetic surveys and geoidal heights from Global Positioning System (GPS) and leveling surveys (Wolf and Ghilani, 2002). A GPS-leveling-derived geoidal height is defined as

$$N = h - H \tag{5.2}$$

where N, h and H are geoidal height, ellipsoidal height and orthometric height, respectively. Due to the need in engineering and mapping applications, geoidal

heights from GPS and leveling in coastal areas could be abundant. In the case of combining altimeter and other data for gravity derivation, it would be difficult to use a FFT-based method even if it is possible (e.g., the input-output system method (Li and Sideris, 1997)). The LSC method outlined in chapter 2 is an efficient method for data combination, only requiring related models of covariance functions. A good weighting scheme for different types of data is essential for obtaining a good result. The usefulness of land gravity data in enhancing the accuracy of altimeter-derived gravity anomaly will be demonstrated in Section 5.5.2.

5.4 Outlier Distribution

The altimeter data we used are from the non-repeat missions ERS-1/GM and Geosat/GM, and the repeat missions Geosat/ERM, ERS-1/35-day, ERS-2/35-day and TOPEX/Poseidon 10-day repeats. Since no reliable estimate of SST is available here, it was set to zero. Neglecting SST here will introduce error at sub-mgal level (Hwang, 1997). For LSC computations, standard errors of the altimeter data are needed. For repeat missions, the standard errors of the altimeter data are derived from repeat observations, while for non-repeat missions, the standard errors are based on empirical values (Hwang et al., 2002). All altimeter data were screened against outliers using differenced heights. Figure 5.6 and 5.7 show the distribution of outliers over ECS and TS all altimeter missions. Outliers can occur anywhere in the oceans. Table 5.2 and Table 5.3 show the summary of outlier rejection over ECS and TS respectively. The outliers in the open oceans come largely from the non-repeat missions (Geosat/GM and ERS-1/GM). Due to data editing in extracting SSHs from the geophysical data records (GDRs), most of the bad altimeter data in the immediate

vicinity of coasts have already been removed before outlier detection. In general, there is a higher concentration of outliers near the coasts and islands than other areas. In particular, clusters of outliers were found at the southern Korean coast, the estuary of the Yangtze River and Peng-Hu Island over TS.
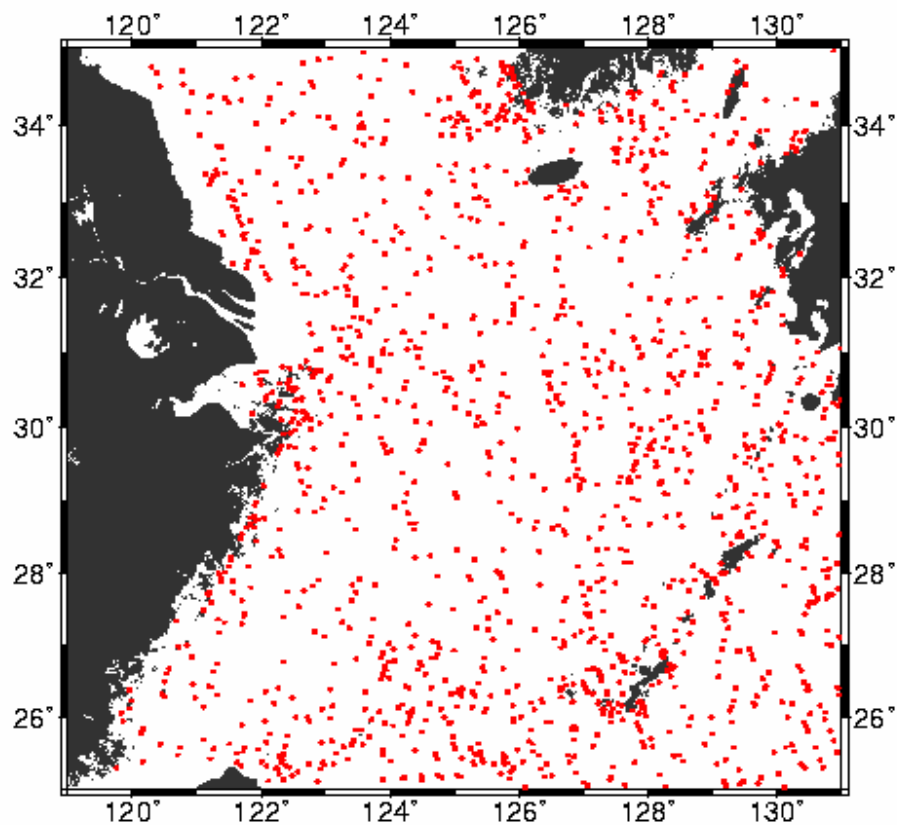
Figure 5.6: Distribution of altimeter data outliers in the East China Sea.
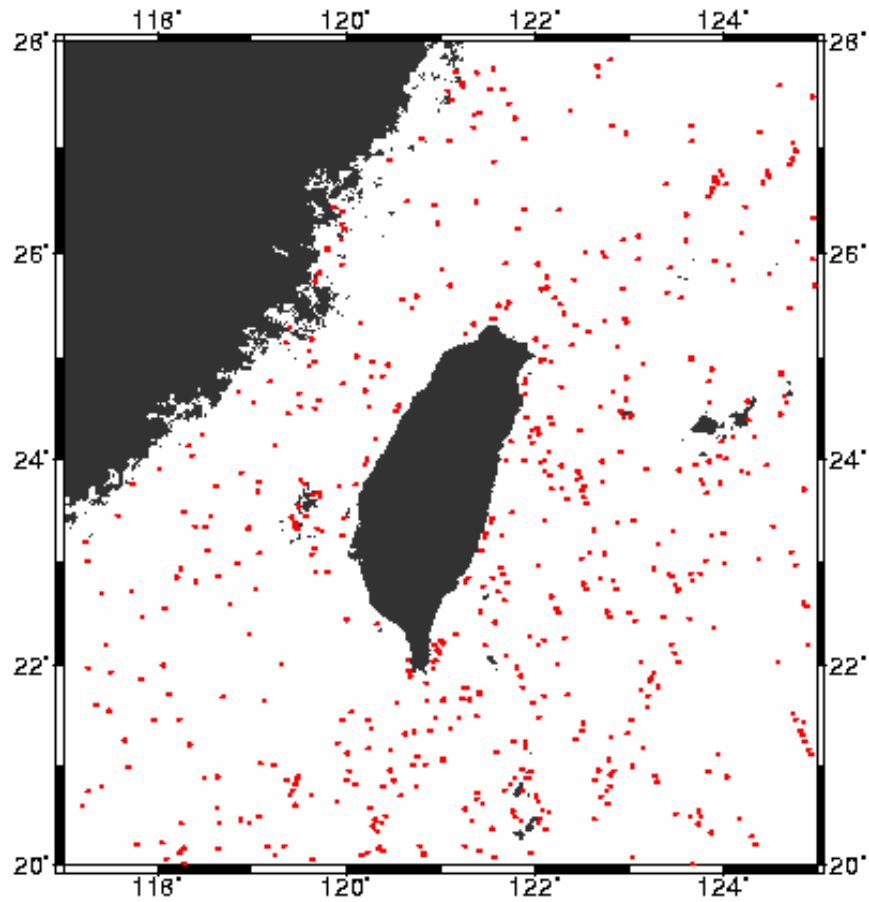
Figure 5.7: Distribution of altimeter data outliers in Taiwan Strait.

Table 5.2: Summary of outliers rejection in the East China Sea (119/131/25/35)

data	No. of passes	No. of differenced ssh	outliers	Reject%
Geosat/gm	615	96392	873	0.9
Geosat/erm	37	15797	452	2.8
ERS2/35d	39	3509	80	2.2
ERS1/35d	37	3528	75	2.1
ERS1/gm	368	37173	334	0.9
Seasat	50	5631	67	1.2
T/P	12	1236	52	4.0

Table 5.3: Summary of outliers rejection around Taiwan (117/125/20/28)

data	No. of passes	No. of differenced ssh to be used	outliers	reject%
Geosat/gm	406	55579	555	1.0
Geosat/erm	24	6985	246	3.4
ERS2/35d	26	1905	41	2.1
ERS1/35d	26	1868	69	3.6
ERS1/gm	246	19627	163	0.8
Seasat	36	2944	31	1.0
T/P	8	596	34	5.0

5.5 Case Study

5.5.1 The East China Sea

The first case study to assess the accuracies of gravity anomaly from the three altimeter-derived observations (mentioned in section 2.3 and 4.3) was carried out over ECS. We experimented with four cases of altimeter-gravity conversion. In these four cases, we used two methods of conversion: LSC and the inverse Vening Meinesz method (Hwang, 1998), and three altimeter-derived observations: DOV, differenced height and height slope. To identify the best case, we compared the altimeter-derived gravity anomalies with shipborne gravity anomalies. Figure5.1 shows the tracks of two selected ship cruises in the ECS (Tracks dmm07 and c1217) and two cruises in the TS (Tracks 1 and 2). The shipborne gravity data over ECS are from NGDC. Before comparison, for each track we removed a bias and a trend in the shipborne gravity relative to the altimeter-derived gravity anomalies (Hwang and Parsons, 1995). Table 5.4 shows the statistics of the differences between the altimeter-derived and shipborne gravity anomalies. The best result is from the case of using LSC with

differenced height, followed by the case of using LSC with height slope. The case of using LSC with DOV yields the least accurate gravity anomalies. Figure 5.8 shows the shipborne and altimeter-derived gravity anomalies along c1217 and dmm07. In general, the altimeter-derived gravity anomalies are smoother than the shipborne gravity anomalies. This is due to the filtering of the altimeter observations before the gravity derivations. At large spatial scales, the shipborne and altimeter-derived gravity anomalies agree very well, but at small spatial scales the differences become random and are not correlated with standard deviation of SSH, tidal difference or depth.

To see the possible sources causing the differences between altimeter-derived and shipborne gravity anomalies, we computed the normalized values of gravity anomaly differences (Case 1 gravity anomaly vs. shipborne gravity anomaly), depths, standard errors of ERS-1 SSH, tidal height differences (CSR4.0 vs. NAO 99) along Cruises c1217 and dmm07. As seen in Figure 5.9 and 5.10, the gravity anomaly differences fluctuate rapidly and do not possess a particular pattern with respect to the other three quantities. Over the shallow waters (depth less than 100 meters) of the ECS, both gravity anomaly differences and tidal height differences are relatively large. In general, the standard error of ERS-1 SSH increases with decreasing depth. Furthermore, the tidal height difference is larger over shallow waters than over the deep waters, and this agrees with the conclusion drawn in Section 5.2.

Table 5.4: Statistics of differences (in mgals) between altimeter-derived and shipborne gravity anomalies in East China Sea.

Case	Mean	RMS	Min	Max
LSC with differenced height	-5.33	13.02	-49.24	43.96
LSC with height slope	-5.45	13.19	-50.77	44.38
LSC with DOV	-4.61	16.99	-85.59	74.65
Inverse Vening Meinesz with DOV	-4.11	15.53	-52.23	80.53

Table 5.5: Statistics of differences (in mgals) between altimeter-derived gravity and two tracks of shipborne gravity anomalies in Taiwan Strait

Case	Mean	RMS	Minimum	Maximum
LSC with differenced height	7.91	9.82	-7.68	23.58
LSC with height slope	7.65	10.30	-9.13	28.30
LSC with DOV	9.39	12.16	-9.14	28.87
Inverse Vening Meinesz with DOV	9.14	11.61	-14.88	27.79
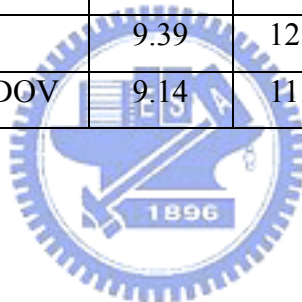
Table 5.6: Statistics of difference (in mgals) between altimeter-derived and shipborne gravity anomalies in the Taiwan Strait

Method and data for gravity derivation	Mean	RMS	Min	Max
LSC with differenced heights only	8.01	9.06	-12.21	24.84
LSC with differenced heights and land gravity anomalies	6.22	8.22	-11.85	22.73
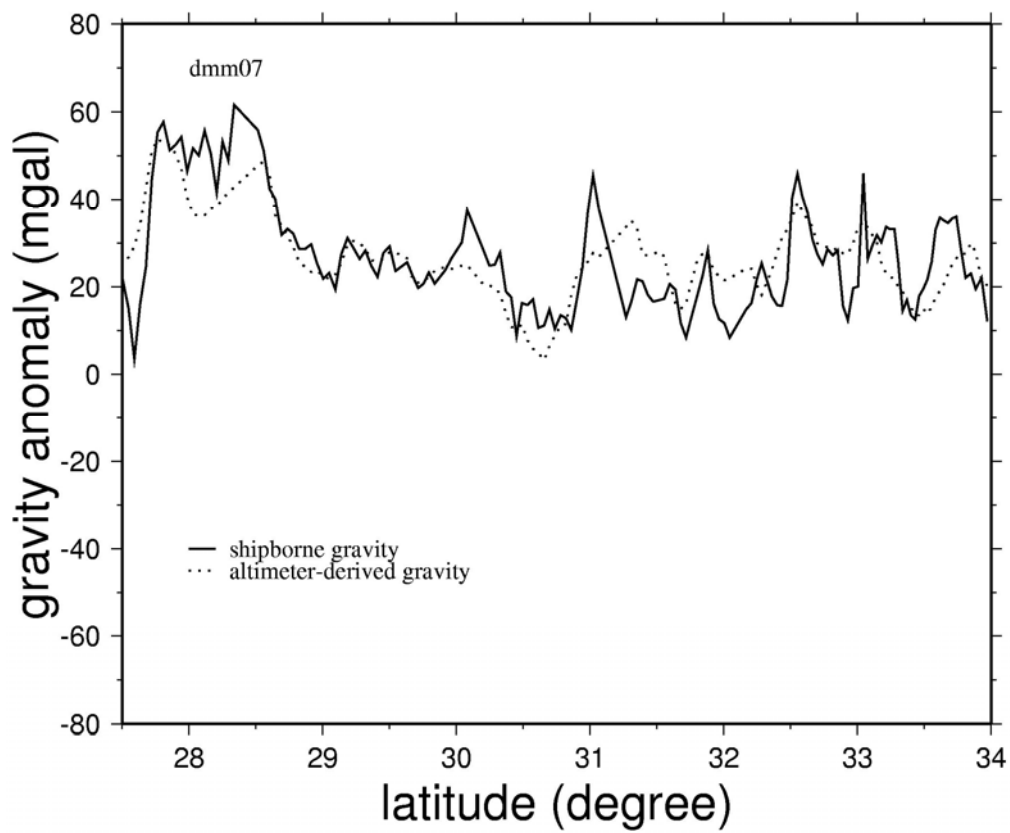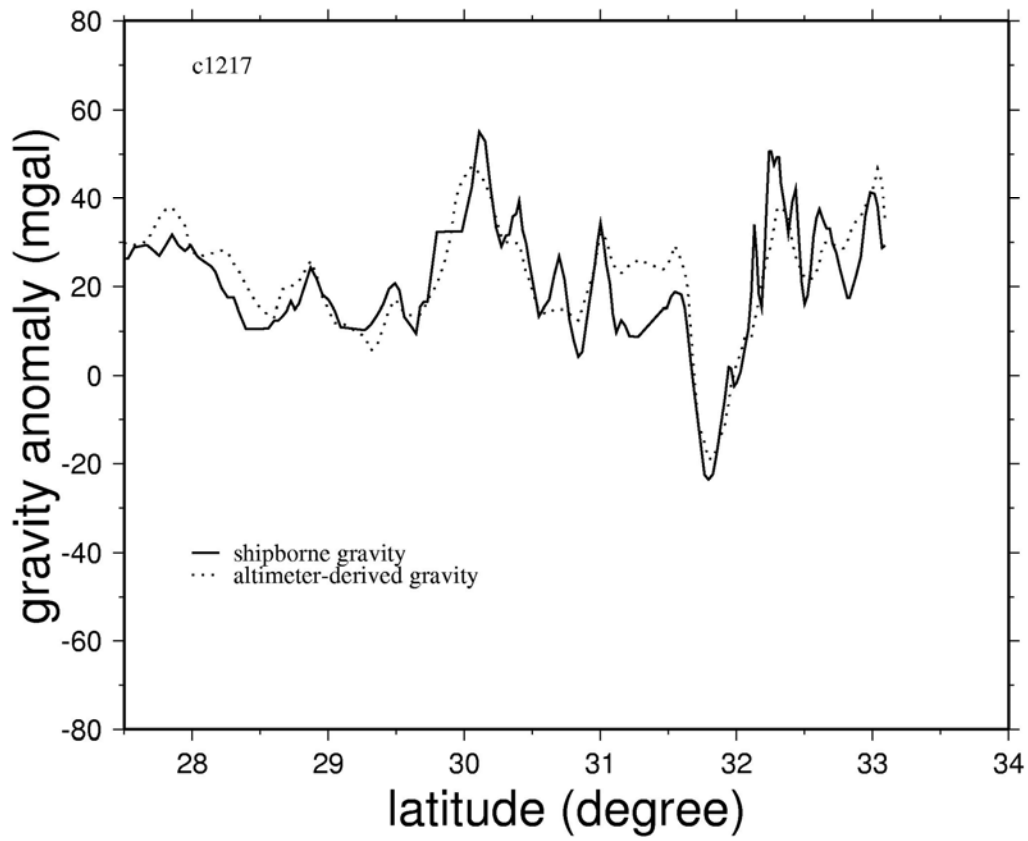
Figure 5.8: Gravity anomalies along Cruises c1217 and dmm07 in the East China Sea
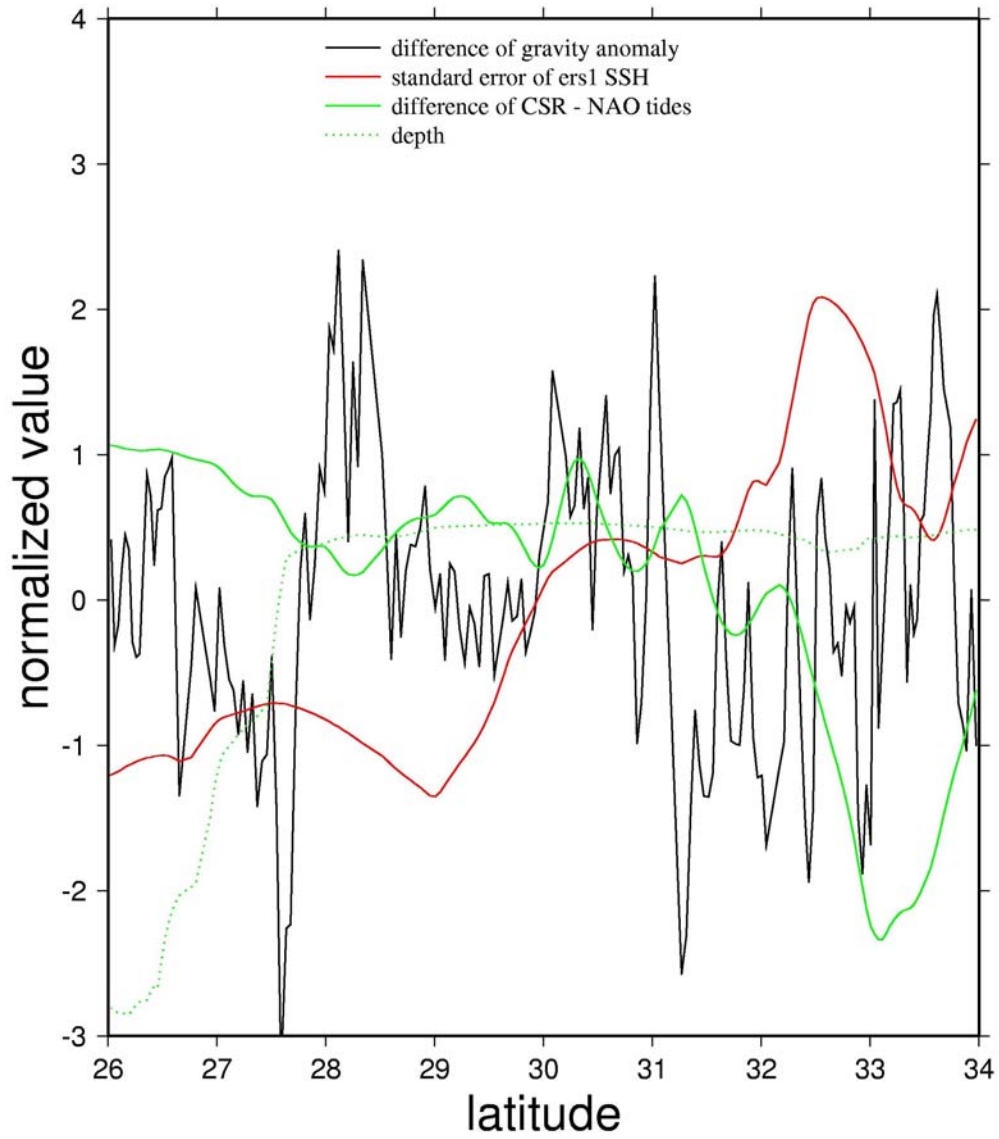
Figure 5.9: Time series of normalized difference of gravity anomaly, standard error of ERS-1 SSH, tide model difference and depth, along Cruise dmm07.
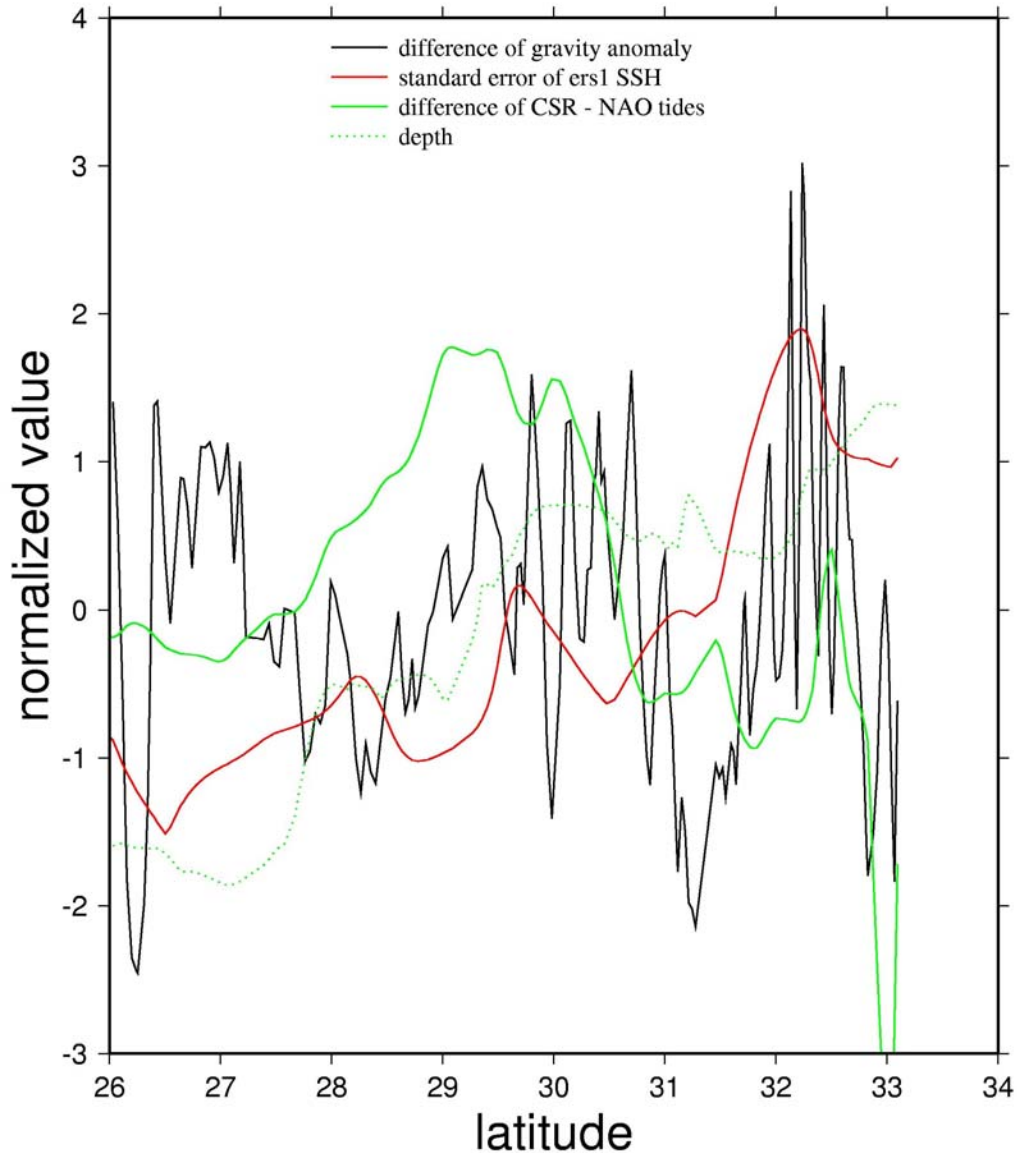
Figure 5.10: Time series of normalized difference of gravity anomaly, standard error of ERS-1 SSH, tide model difference and depth, along Cruise c1217.

5.5.2 The Taiwan Strait

Next we carried out experiments over TS using the same four cases as in the ECS. We used shipborne gravity data along Tracks 1 and 2 (Figure 5.1) to evaluate the altimeter-derived gravity anomalies. These shipborne gravity data were compiled

by Hsu et al. (1998), who has crossover adjusted the shipborne gravity data and removed bad values. Table 5.5 shows the results of the comparisons between altimeter-derived and shipborne gravity anomalies in the four cases. The conclusion from Table 5.5 is similar to what has been drawn from Table 5.4, that is, the least square collocation method with DOV produces the worst result. Again, use of differenced heights produces the best results provided that the same altimeter-gravity conversion method is used.

Since land gravity data are available along the coast of TS, we also assessed the impact of land gravity data on the accuracy of altimeter-derived gravity anomaly. Figure 5.11 shows the distribution of land gravity and altimeter data around Taiwan. Note that there is no altimeter at the immediate coastal waters off the west coast of Taiwan. We experimented with the method of LSC using differenced heights, and with and without land gravity data (two cases). Table 5.6 shows the statistics of the differences between shipborne and altimeter-derived gravity anomalies. Figure 5.12 shows the shipborne and altimeter-derived gravity anomalies along Tracks 1 and 2. The patterns of the difference along Tracks 1 and 2 are similar to those for Tracks c1217 and dmm07 (Figure 5.8). That is, the agreement between shipborne and altimeter-derived gravity anomalies at large spatial scales is better than that at small spatial scales. Furthermore, Tracks 1 and 2 are only tens of km off the west coast of Taiwan and the density of altimeter data is low along theses two tracks (Figure 5.11). In general, difference of gravity anomaly increases with decreasing density of altimeter data. The density of land gravity data is relatively high over a zone from $22.5°$N to $24.5°$N, and here the agreement between altimeter-derived (with land gravity) and shipborne gravity anomalies is better than that in other parts of the ship tracks. In the areas south of $22.5°$N and north of $24.5°$N, only few land gravity data

94

are used, so there is virtually no difference between the altimeter-only gravity anomalies and the altimeter-land gravity anomalies.
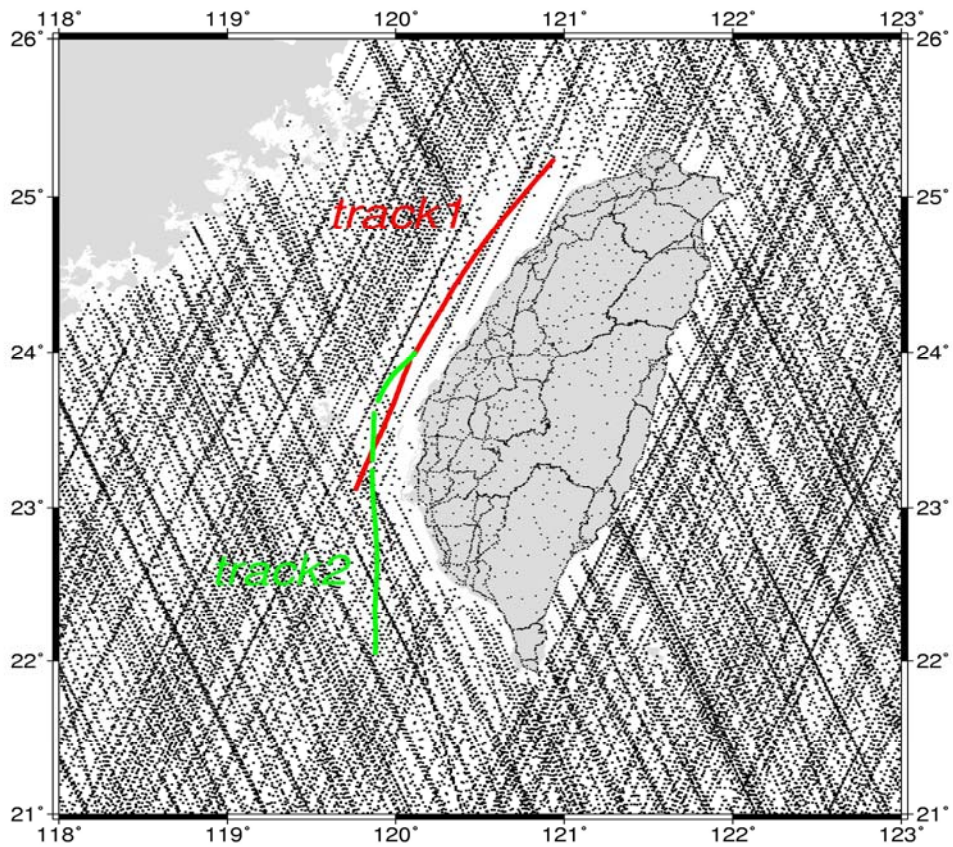
Figure 5.11: Distribution of land gravity data and altimeter data around Taiwan.
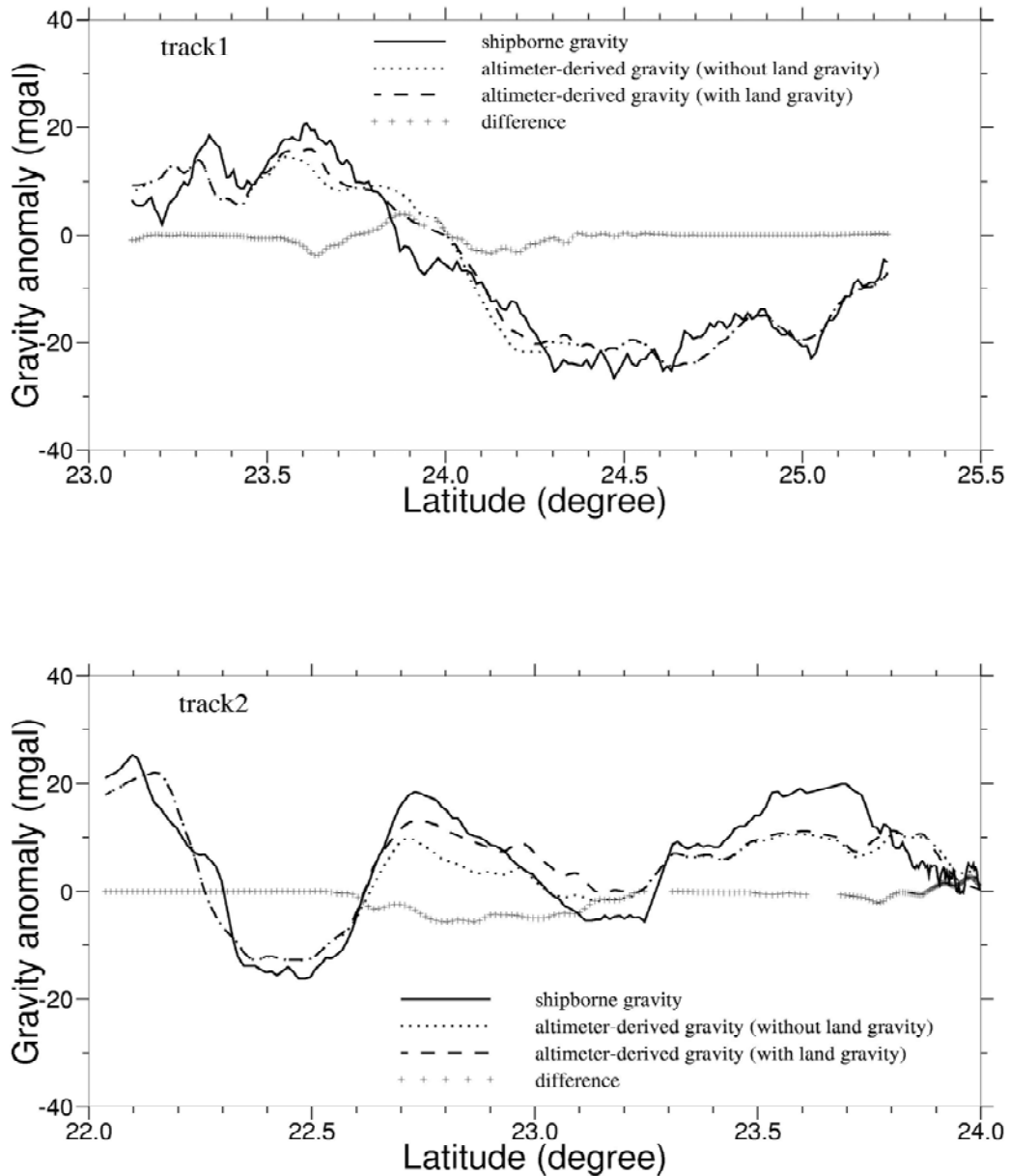
Figure 5.12: Gravity anomalies along Track 1 and Track 2 in the Taiwan Strait.

Again, we investigated the possible causes of the difference between altimeter-derived and shipborne gravity anomalies in the TS. Figure 5.13 and 5.14 shows the same quantities as in Figure 5.9 and 5.10, but in the TS. Again, along the two ship tracks, the patterns of gravity anomaly difference are quite random and are

not correlated with depth and tidal height difference. However, there is a strong correlation (about 0.9) between standard error of ERS-1 SSH and tidal height difference along both Tracks 1 and 2. Again, tidal height difference increases as decreasing depth. The conclusions from the analyses associated with Figures 5.9 & 5.10 and Figures 5.13 & 5.14 are in agreement with the conclusion drawn in Section 5.2: the major source of large standard error of SSH and large error of altimeter-derived gravity anomaly is tide model error. Another cause of degraded altimeter-derived gravity anomaly near coasts, which is not investigated in this paper, is low altimeter data density due to data editing. Even the data editing criterion near coasts is relaxed to increase data density, the additional altimeter data may not be of good quality for gravity derivation. One way to improve altimeter data quality near coasts is to retrack waveforms of altimeter ranging. For example, Deng et al. (2003) have obtained improved T/P SSHs by waveform retracking over the Australian coasts. Currently, globally retracked ERS-1 and Geosat waveforms are available (Lillibridge et al., 2004; Smith et al., 2004), and have been shown to produce improved marine gravity fields.

Figure 5.13: Time series of normalized difference of gravity anomaly, standard error of ERS-1 SSH, tide model difference and depth, along Track 1
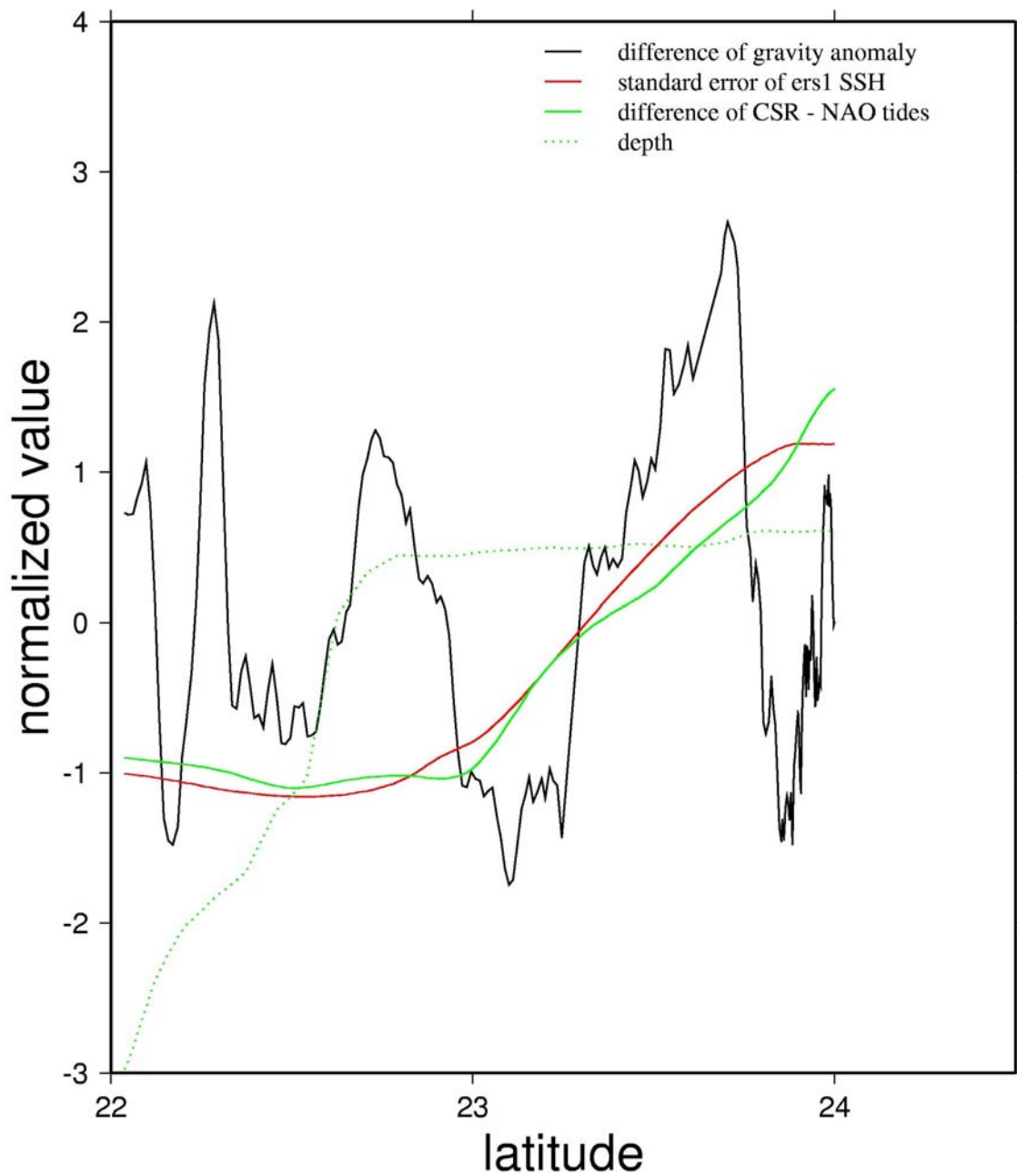
Figure 5.14: Time series of normalized difference of gravity anomaly, standard error of ERS-1 SSH, tide model difference and depth, along Track 2.
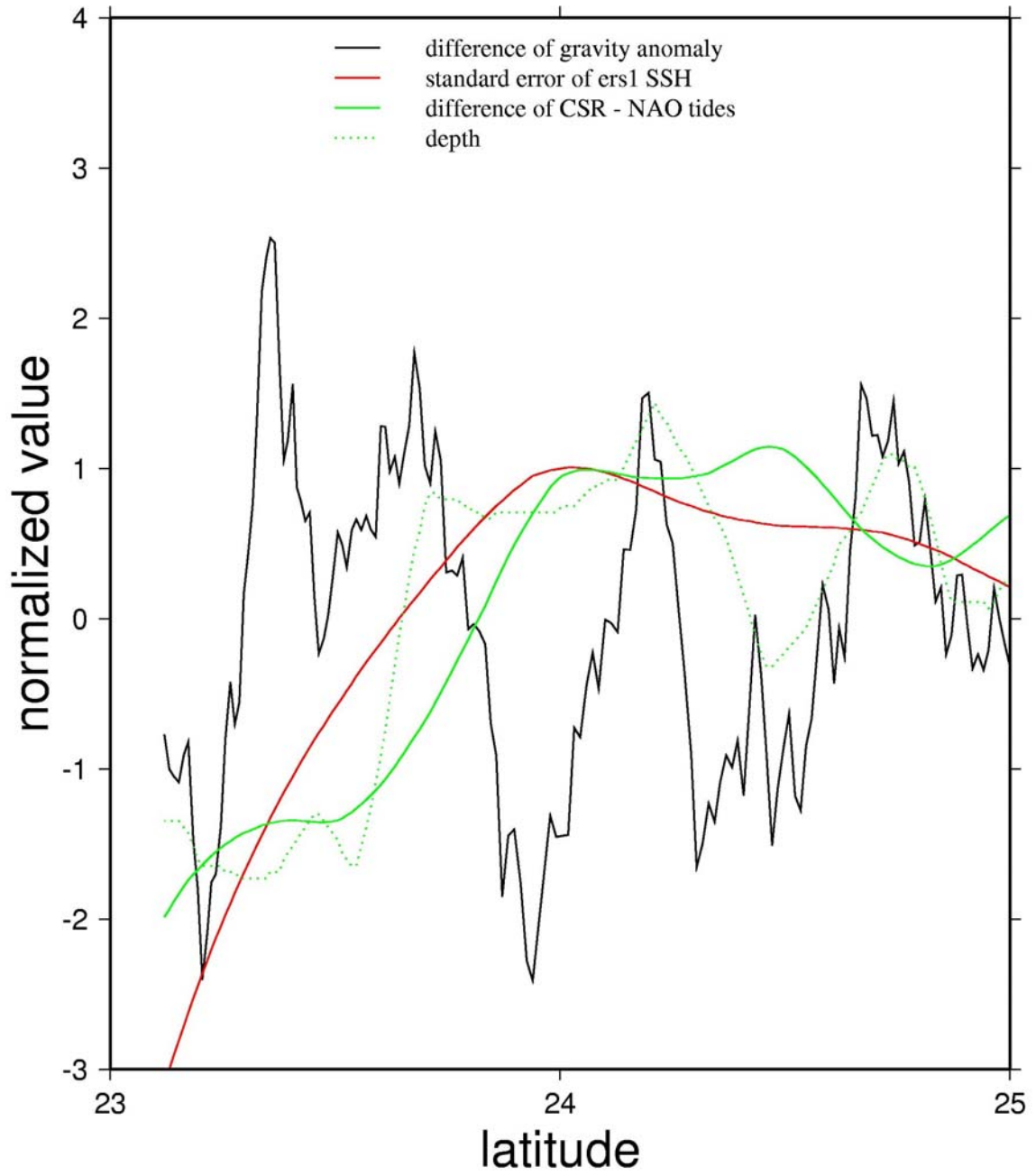
CHAPTER 6

CONCLUSIONS AND RECOMMENDATIONS

6.1 Conclusions

In this thesis, Chapter 2 first introduces 4 methods for gravity anomaly derivations from altimetry, which include a completely different kind of case, LSC with differenced height. Chapter 2 and 3 describe the work of an improved computation of global MSSH and gravity anomaly grids using improved multi-satellite altimeter data sets and a new procedure. Various tests have been made in order to find an optimal set of parameters for the computation. The procedure is based on the deflection-geoid and inverse Vening Meinesz formulas, as well as the remove-restore concept.   The crossover adjustment of SSHs is not used because of the use of DOV as the altimeter data type in the computation. Using DOV is particularly advantageous over areas with sparse altimeter data and in the case of long wavelength error contained in altimeter data. The comparisons of the NCTU01 MSSH with the T/P and the ERS-1 MSSH result in overall RMS differences of 5.0 and 3.1 cm in SSH, respectively,   and   7.1 and 3.2 μrad in SSH gradient, respectively. The agreements between the predicted and shipborne gravity anomalies range from 3.0 to 13.4 mgals, depending on the gravity signatures and the altimeter data noise, the later being affected by instrument noise, sea state and accuracies of geophysical corrections. The NCTU01 MSSH model outperforms the NASA/GSFC model (Wang, 2001) and the CLS model, and the NCTU01 gravity anomaly model has a better accuracy than those of the models of Sandwell and Smith (1997) and Hwang et al.

(1998). The gravity anomalies described in Chapter 3 can be used to derive mean gravity anomalies for modeling high-degree geopotential coefficients, and to study the spectral properties of the Earth's gravity field.

Chapter 4 compares two methods with three kinds of altimeter data types of gravity anomaly derivation from altimetry data. For the four computations of two methods, the RMS differences between altimetry-derived gravity anomalies and shipborne gravity anomalies are 9.06 (differenced height) and 9.59, 10.26 (height slope) and 9.77, 10.44 and 13.10, 10.73 and 11.86 mgals, over TS and ECS, respectively. Comparing to NCTU01 gravity anomaly model, the RMS differences are further reduced by 1.67 and 2.27 mgal in these two areas. The method of LSC with differenced heights yields promising results and produced the best accuracy over TS and ECS. An iterative method to remove outliers in along-track altimeter data improves altimeter data quality and improves the accuracy of predicted gravity anomaly. Preprocessing of altimeter data is important in obtaining good estimation of gravity. Good estimation of gravity depends on both good altimeter data and good method. Use of along-track DOV with LSC yields a better result over TS, but gives a worse result over ECS compared to the result from the inverse Vening Meinesz formula. However, the inverse Vening-Meinesz formula with 1D FFT is the fastest methods among the three methods.

Chapter 5 studies the sources of the differences among two global gravity anomaly grids over ECS and TS. We conclude that tide model error is the biggest contributor to the differences. It is found that tide model error, standard deviation of SSH and ocean depth are highly correlated. Also, the complicated sea states over these two areas increase the roughness of the sea surface and hence the noise level of altimeter ranging. As case studies, we experimented with the method of LSC using

differenced heights, and with and without land gravity data. Including land gravity data in the vicinity of coasts enhances the accuracy of altimeter-derived gravity anomalies. Future studies of gravity anomalies recovery will focus on shallow waters over the Yellow Sea, South China Sea and Southeast Asia.

6.2 Recommendations

For future work, we recommend a procedure to improve the accuracy of altimeter-derived gravity anomalies: (1) retrack near-shore waveforms of altimeter to produce waveform-corrected SSHs, (2) use the corrected SSHs to improve tide model, (3) use improved tide model to correct for the ocean tide effect in SSH. Finally, the improved tide-corrected and waveform-corrected altimeter data will lead to an improved gravity field over shallow waters. In addition, the altimeter derived gravity could be improved by merging the altimeter data available today with those derived from future and more accurate missions, and by combining with other sources of data, such as airborne observations and shipborne gravity data to do the prediction procedure.

REFERENCE

Andersen, O.B., Knudsen, P., and Tscherning, C.C. (1996) Investigation of methods for global gravity field recovery from the dense ERS-1 geodetic mission altimetry. In: Rapp R, Nerem RS, Cazenave A (eds), Global gravity field and temporal variations. IAG Symposium 116. Springer, Berlin Heidelberg New York, pp. 218-226.

Andersen, O. and Knudsen, P. (1998) Global marine gravity from the ERS-1 and Geosat geodetic mission altimetry. *J. Geophys. Res.,* 103, pp. 8129-8137.

Andersen, O.B. and Kundsen, P. (2000) The Role of satellite altimetry in gravity field modeling in coastal areas, *Phys. Chem. Earth (A)*, 25, 1, pp. 17-24.

Andersen, O.B., Knudsen, P. and Trimmer, R. (2001) The KMS2001 Global Mean Sea Surface and Gravity Field, IAG2001 Scientific Assembly, Budapest, Hungary, September.

Andersen, O.B., Knudsen, P. and Trimmer, R. (2005) Improved high resolution altimetric gravity field mapping (KMS2002 global marine gravity field). *Proc., IAG Symposia*, 127, IUGG Sapporo, 2003, Springer, Berlin.

Anzenhofer, M. and Shum, C.K. (2001) Coastal Altimetry and Applications. Rep of Dept of Geodetic Science and Surveying, in press, Ohio State University, Columbus.

Archiving, Validation, and Interpretation of Satellite Oceanographic Data (1996) AVISO User Handbook for Merged TOPEX/Poseidon Products, 3rd Ed. Toulouse, France.

Balmino Moynot, G.B., Sarrailh, M. and Vales, N. (1987) Free air gravity anomalies over the oceans from SEASAT and GEOS-3 altimetry data, *EOS Trans*. AGU, 68, pp. 17-19.

Basic, T. and Rapp, R.H. (1992) Ocean wide prediction of gravity anomalies and sea surface heights using GEOS-3, SEASAT and GEOSAT altimeter data, and ETOPO5U bathematric data, Report No. 416, Department of Geodetic Science and Surveying, The Ohio State University, Columbus, Ohio.

Bilitza, D. (1997) International reference ionosphere - status 1995/96.*Adv. Space Res.*, 20, (9), pp. 1751-1754.

Cazenave, A. and Royer, J.Y. (2001) Applications to marine geophysics, in: Satellite Altimetry and Earth Sciences: a Handbook of Techniques and Applications, Fu,

L.L., and Cazenave, A. (ed.), Academic Press, San Diego.

Chen, S.A. (2001) Determinations of tide, circulation and eddied over the South China Sea using TOPEX/POSEIDON altimeter data. PhD thesis, National Chiao Tung University, Hsinchu, Taiwan.

De Boor, C. (1978) A practical guide to splines. Springer, Berlin.

Deng, A., Featherstone, W., Hwang, C. and Berry, P. (2002) Waveform retracking of ERS-1, *Mar. Geod.*, in press.

Deng, X., Featherstone, W.E., Hwang, C. and Berry, P.A.M. (2001) Estimation of Contamination of ERS-2 and POSEIDON Satellite Radar Altimetry Close to the Coasts of Australia, paper submitted to *Mar. Geod.*.

Eanes, R. (1999) Improved ocean tide model from satellite altimetry. Fall Meeting 1999, Am. Geophys Un, San Francisco.

Eren, K. (1980) Spectral Analysis of Geos-3 Altimeter Data and Frequency Domain Collocation, OSU, Rep. 297.

Fairhead, J.D. and Green, C.M. (2001) Pushing the resolution boundaries of marine satellite gravity, IAG 2001 Scientific Assembly, Budapest.

Fu, L.-L., and Cazenave, A. (Eds), (2001) Satellite Altimetry and Earth Sciences: A Handbook of Techniques and Applications. Academic Press, San Diego.

Fu, L.-L. (editor) (2003) Wide-Swath Altimetric Measurement of Ocean Surface Topography, JPL Publication 03-002, Jet Propulsion Laboratory, Pasadena, CA, pp. 67. (ftp://ftp-oceans.jpl.nasa.gov/pub/llf/WSOAreportFinal2.pdf)

Fu, L.L. and Rodriguez, E. (2004) High-Resolution Measurement of Ocean Surface Topography by Radar Interferometry for Oceanographic and Geophysical Applications, American Geophysical Union, San Francisco.

Gerald, C.F., and Wheatley, P.O. (1994) Applied Numerical Analysis, 5th Ed, Addison-Wesley, New York.

Gomez, V., Maravall, A. and Pena, D. (1999) Missing observations in ARIMA models: skipping approach versus additive outlier approach, *J. Econometrics*, 88, (2), pp. 341-363.

Haxby, W.F., Karner, G.D., La Brecque, J.L., and Weissel, J.K. (1983) Digital images of combined oceanic and continental data sets and their use in tectonic studies, *EOS Trans*, 64, pp. 995-1004.

Haxby, W.F. (1987) Gravity field of the world's oceans. A portrayal of gridded geophysical data derived from Seasat radar altimeter measurement of the shape of the ocean surface, National Geophysical Data Center, Boulder, CO.

Heiskanen, W.A. and Moritz, H. (1985) Physical Geodesy. Reprint, Institute of Physical Geodesy, Tech. University of Graz, Austria.

Hernandez, F. and Schaeffer, P. (2000) Altimetric Mean Sea Surfaces and Gravity Anomaly maps inter-comparisons AVI-NT-011-5242-CLS, CLS Ramonville St Agne.

Hipkin, R., (2000)   Modeling the geoid and sea-surface topography in coastal areas. *Phys. Chem. Earth (A)*, 25, (1), pp. 9-16.

Hsu, H.Y. (1997) Global Marine Geoid from Multi-Satellite Altimetry and It's application, MSD thesis of department of civil engineering, National Chiao Tung University, Hsinchu, Taiwan. (in Chinese)

Hsu, S., Liu, C., Shyu, C., Liu, S., Sibue, J., Lallemand, S., Wang, C. and Reed, D. (1998) New gravity and Magnetic Anomaly Maps in the Taiwan-Luzon region and their preliminary interpretation, TAO, 9, 3, pp. 509-532.

Hwang, C. (1989) High precision gravity anomaly and sea surface height estimation from Geo-3/Seasat altimetry date, Report No. 399, Department of Geodetic Science and Surveying, The Ohio State University, Columbus, Ohio.

Hwang, C. and Parsons, B. (1995) Gravity anomalies derived from Seasat, Geosat, ERS-1 and TOPEX/POSEIDON altimetry and ship gravity : A case study over the Reykjanes Ridge, *Geophys. J. Int.*,122, pp. 551-568.

Hwang, C. and Parsons, B. (1996) An optimal procedure for deriving marine gravity from multi-satellite altimetry, *Geophys. J. Int.*, 125, pp. 705-719.

Hwang, C. (1997) Analysis of some systematic errors affecting altimeter-derived sea surface gradient with application to geoid determination over Taiwan. *J. Geod.*, 71, pp. 113-130.

Hwang, C. (1998) Inverse Vening Meinesz formula and deflection-geoid formula: application to prediction of gravity and geoid over the South China Sea. *J. Geod.*, 72, pp. 304-312.

Hwang, C., Kao, E.C. and Parsons, B. (1998) Global Derivation of marine gravity anomalies from Seasat, Geosat, ERS-1 and TOPEX/POSEIDON altimeter data. *Geophys. J. Int.*, 134, pp. 449-459.

Hwang, C., Hsu, H. and Jang, R. (2002) Global mean sea surface and marine gravity anomaly from multi-satellite altimetry: applications of deflection-geoid and inverse Vening Meinesz formulae, *J. Geod.,* 76, pp. 407-418.

Hwang, C., Hsu, H.Y. and Deng, X. (2004) Marine gravity anomaly from satellite altimetry: a comparison of methods over Shallow Waters, International Association of Geodesy Symposia, 126, pp. 59-66, Springer, Berlin.

Hwang, C., Shum, C.K. and Li, J.C. (Eds.) (2004a) Satellite Altimetry for Geodesy, Geophysics and Oceanography. International Association of Geodesy Symposia, 126, Springer, Berlin.

Jacobs, G.A., Hur, H.B. and Riedlinger, S.K. (2000) Yellow and East China Seas response to winds and currents. *J. Geophys. Res.*, 105, (C9), pp. 21947-21968.

Jan, S., Chern, C.S., Wang, J. and Chao, S.Y. (2004) The anomalous amplification of M-2 tide in the TS. *Geophys. Res. Lett.*, 31, (7), Art. No. L07308.

Kaiser, R. (1999) Detection and estimation of structural changes and outliers in unobserved components, *Comp. Stat.*, 14, (4), pp. 533-558 .

Kalnay, E., Kanamitsu, M., Kistler, R., Collins, W., Deaven, D., Gandin, L., Iredell, M., Saha, S., White, G., Woollen, J., Zhu, Y., Chelliah, M., Ebisuzaki, W., Higgins, W., Janowiak, J., Mo, K.C., Ropelewski, C., Wang, J., Leetmaa, A., Reynolds, R., Jenne, R. and Joseph, D. (1996) The NCEP/NCAR 40-year reanalysis project. *Bull. Am. Meteol. Soc.*, 77, pp. 437-471.

Knudsen, P. (1987) Estimation and modeling of the local empirical covariance function using gravity and satellite altimeter data, *Bull. Geodesique.*, 61, pp. 145-160.

Koch, K.R. (1970) Gravity anomalies for ocean areas from satellite altimetry, Proceedings of the Second Marine Geodesy Symposium, Marine Technology Society, Washington, D.C.

Koch, K.R. (1987) Parameter Estimation and Hypothesis Testing in Linear Models, Springer, Berlin.

Lefevre, F., Le Provost, C. and Lyard, F.H. (2000) How can we improve a global ocean tide model at a regional scale? A test on the Yellow Sea and the East China Sea. *J. Geophys. Res.*, 105, (C4), pp. 8707-8725.

Lemoine, F.G., Kenyon, S.C., Factor, J.K., Trimmer, R.G., Pavlis, N.K., Chinn, D.S.,

Cox C.M., Klosko, S.M., Luthcke, S.B., Torrence, M.H., Wang, Y.M., Williamson, R.G., Pavlis, E.C., Rapp, R.H. and Olson, T.R. (1998) The Development of Joint NASA GSFC and the National Imagery and Mapping Agency (NIMA) Geopotential Model EGM96. Rep NASA/TP-1998-206861, National Aeronautics and Space Administration, Greenbelt, MD.

Le Traon, P.Y. and Ogor, F. (1998) ERS-1/2 orbit improvement using TOPEX/POSEIDON: The 2 cm challenge. *J. Geophys. Res.,* 103, pp. 8045-8057.

Lemoine, F.G, Kenyon, S.C., Factor, J.K., Trimmer, R.G., Pavlis, N.K., Chinn, D.S., Cox, C.M., Klosko, S.M, Luthcke, S.B., Torrence, M.H., Wang, Y.M., Williamson, R.G., Pavlis, E.C., Rapp, R.H. and Olson, T.R. (1998) The Development of Joint NASA GSFC and the National Imagery and Mapping Agency (NIMA) Geopotential Model EGM96. Rep NASA/TP-1998-206861, National Aeronautics and Space Administration, Greenbelt, MD.

Levitus, S., Monterey, G.I. and Boyer, T. (1997) Seasonal Variability of Dynamic Height and its Fourier Analysis. NOAA NESDIS Atlas 15, U.S. Gov. Printing Office. Wash., D.C.

Li, J. and Sideris, M. (1997) Marine gravity and geoid determination by optimal combination of satellite altimetry and shipborne gravimetry data. *J. Geod.,* 71, pp. 209-216.

Liang, C.K. (1983) The Adjustment and Combination of Geos-3 and Seasat Altimeter Data. Rep 346, Dept of Geodetic Science and Surveying, Ohio State University, Columbus.

Lillibridge, J.L., Smith, W.H.F, Scharroo, R. and Sandwell, D.T. (2004) The Geosat geodetic mission twentieth anniversary edition data product. AGU 2004 Fall meeting, San Francisco.

Matsumoto, K., Takanezawa, T. and Ooe, M. (2000) Ocean Tide Models Developed by Assimilating TOPEX/POSIDON Altimeter Data into Hydrodynamical Model: A Global Model and a Regional Model around Japan. *J. Oceanogr.,* 56, pp. 567-581.

Matsumoto, K., Sato, T., Takanezawa, T., and Ooe, M. (2001) GOTIC2: A Program for Computation of Oceanic Tidal Loading Effect. *J. Geod. Soc.,* Japan, 47, pp. 243-248.

Moritz, H. (1980) Advanced Physical Geodesy, Herbert Wichmann, Karlsruhe.

Niwa, Y. and Hibiya, T. (2004) Three-dimensional numerical simulation of M-2 internal tides in the East China Sea. *J. Geophys. Res.*, 109, (C4), Art. No. C04027.

NOAA (1997) The Complete Geosat Altimeter GDR Handbook, NODC Laboratory for Satellite Altimetry. Silver Spring, Maryland.

Olgiati, A., Balmino, G., Sarrailh, M., and Green, C.M. (1995) Gravity anomalies from satellite altimetry: comparison between computation via geoid heights and via deflections of the vertical. *Bull. Geod.*, 69, pp. 252-260.

Pearson, R.K. (2002) Outliers in process modelling and identification, *IEE Trans on Control Tech*, 10, pp. 55-63.

Pope, A.J. (1976) The statistics of residual and the detection of outliers, *Tech. Rep.* TR-NOS-65-NGS-1, National Ocean Survey, Rockville.

Randel, D.L., VonderHaar, T.H., Ringerud, M.A., Stephens, G.L., Greenwald, T.J. and Combs, C.L. (1996) A new global water vapor dataset. *Bull. Am. Meteol. Soc.*, 77, pp. 1233-1246.

Rapp, R.H. (1983) The determination of geoid undulations and gravity anomalies from Seasat altimeter data. *J. Geophys. Res.*, 88, pp. 1552-1562.

Rapp, R.H. (1985) Detailed gravity anomalies and sea surface height derived from Geo-3/Seasat altimeter data, Report No. 365, Department of Geodetic Science and Surverying, The Ohio State University, Columbus, Ohio.

Rapp, R. and Balasubramania, N. (1992) A Conceptual Formulation of a World Height System. Rep. No. 421, Dept. of Geod. Sci. and Surveying, Ohio State University, Columbus, Ohio.

Rapp, R.H. and Basic, T. (1992) Oceanwide gravity anomalies from Geos-3, Seasat and Geosat altimeter data, *Geophys. Res. Lett.*, 19, pp. 1979-1982.

Rapp, R.H. and Yi, Y. (1997) Role of ocean variability and dynamic ocean topography in the recovery of the mean sea surface and gravity anomalies from satellite altimeter data. *J. Geod.*, 71, pp. 617-629.

Sandwell, D.T. (1992) Antarctic marine gravity field from high-density satellite altimetry, *Geophys. J. Int.*, 109, pp. 437-448.

Sandwell, D.T. and Smith, W.H.F. (1997) Marine gravity anomaly from Geosat and ERS 1 satellite altimetry. *J. Geophys. Res.*, 102, pp. 10039-10054.

Sandwell, D.T. and Smith, W.H.F. (2001) Bathymetric estimation. In: Fu. L,-L. and Canezave, A. (eds), Satellite Altimetry and Earth Sciences, pp 442-457.

Sandwell, D.T. and Smith, W.H.F. (2001) Bathymetric estimation. In Fu, L.-L. and Cazenave, A. (Eds) Satellite Altimetry and Earth Sciences: A Handbook of Techniques and Applications, Academic Press, New York.

Schwarz, K.P., Sideris, M.G. and Forsberg, R. (1990) The use of FFT techniques in physical geodesy. *Geophys. J. Int.*, 100, pp. 485-514.

Seeber, G. (1993) Satellite Geodesy. de Gruyter, Berlin.

Shum, C.K., Woodworth, P.L., Andersen, O.B., Egbert, G.D., Francies, O., King, C., Klosko, S.M., Le Provost, C., Li, X., Molines, J.M., Parke, M.E., Ray, R.D., Schlax, M.G., Stammer, D., Tierney, C.C., Vincent, P. and Wunsch, C. (1997) Accuracy assessment of recent ocean tide models. *J. Geophys. Res.*, 102, pp. 25173-25194.

Sideris, M.G. (1996) On the use of heterogeneous noisy data in spectral gravity field modelling methods, *J. Geod.*, 70, pp. 470-479.

Smith, W.H.F. and Sandwell, D.T. (2004) Improved global marine gravity field from reprocessing of Geosat and ERS-1 radar altimeter waveforms. AGU 2004 Fall meeting, San Francisco.

Smith, W.H.F. and Wessel, P. (1990) Gridding with continuous curvature splines in tension, *Geophys.*, 55, pp. 293-305.

Torge, W. (1989) Gravimetry, de Gruyter, Berlin.

Trimmer, R.G., Andersen, O. and Driscoll, M.L. (2001) Estimating altimetry 5′×5′ mean gravity anomaly regional accuracies. IAG 2001 Scientific Assembly, Budapest.

Tscherning, C.C. and Rapp, R.H. (1974) Closed covariance expressions for gravity anomalies geoid undulations and deflections of the vertical implied by anomaly degree variance models, Rep 208, Dept of Geod Sci, Ohio State University, Columbus.

Tscherning, C. C. (1997) Geoid determination by Least Squares Collocation, International school for the determination and use of the Geoid, International geoid service, DIIAR, Politecnico di Milano, Italy, pp. 110-135.

Wang, C.K. (2004) Features of monsoon, typhoon and sea waves in the Taiwan Strait. *Mar. Geores. & Geotech.*, 22, (3), pp. 133-150.

Wang, H. (1999) Satellite Altimeter Data Processing and Its Applications in China Seas and Vicinity, PHD thesis of Institute of Geodesy and Geophysics, Chinese Academy of Sciences, Wuhan, Hubei 430077, P.R. China. (in Chinese)

Wang, Y.M. (1993) On the optimal combination of potential coefficient model with terrestrial gravity for FFT geoid computation, *Manuscr. Geodaet.*, 18, pp. 406-416.

Wang, Y.M. (2000) The Satellite Altimeter Data Derived Mean Sea Surface GSFC98, *Geophys. Res. Lett.*, 27, pp. 701-704.

Wessel, P. and Smith, W.H.F. (1995) New version Generic Mapping Tools release, *EOS Trans*, AGU, pp.76.

Wolf, P.R. and Ghilani, C.D. (2002) Elementary Surveying, An Introduction to Geomatics, 10th Ed., Pearson Education International, Upper Saddle River, New Jersey.

Wunsch, C., and Zlotnicki, V. (1984) The accuracy of altimetric surfaces. *Geophys. J. R. astr. Soc.*, 78, pp. 795-808.

Yanagi, T., Morimoto, A. and Ichikawa, K. (1997) Seasonal variation in surface circulation of the East China Sea and the Yellow Sea derived from satellite altimetric data. *Cont. Shelf. Res.*, 17, (6), pp. 655-664.

Yi, Y. (1995) Determination of Gridded Mean Sea Surface from TOPEX, ERS-1 and GEOSAT Altimeter Data. Rep 434, Dept. of Geodetic Science and Surveying, The Ohio State University, Columbus.

Zhang, C. and Blais, J.A.R. (1993) Recovery of gravity disturbances from satellite altimetry and by FFT techniques: a synthetic study, *Manuscr. Geodaet.*, 18, pp. 158-170.

Zhang, C. and Sideris M.G. (1995) Gravity disturbances from GEOSAT data and forward geopotential models in the Labrador Sea, International Association of Geodesy Symposia 113, convened and edited by Sunkel H. and I. Marson, Springer, pp. 376-385.

Zwally, H.J. and Brenner, A.C. (2001) Ice sheet dynamics and mass balance, in LL Fu and A Cazenave (eds), *Satellite altimetry and earth sciences*, pp. 351-370, Academic press, New York.